

Syracuse University

## SURFACE at Syracuse University

---

Dissertations - ALL

SURFACE at Syracuse University

---

Summer 7-1-2022

# Characterization of Scintillation Light in Large Liquid Argon Detectors and the Implications for Proton Decay Searches

Kyle Spurgeon  
*Syracuse University*

Follow this and additional works at: <https://surface.syr.edu/etd>



Part of the [Physics Commons](#)

---

### Recommended Citation

Spurgeon, Kyle, "Characterization of Scintillation Light in Large Liquid Argon Detectors and the Implications for Proton Decay Searches" (2022). *Dissertations - ALL*. 1571.  
<https://surface.syr.edu/etd/1571>

This Dissertation is brought to you for free and open access by the SURFACE at Syracuse University at SURFACE at Syracuse University. It has been accepted for inclusion in Dissertations - ALL by an authorized administrator of SURFACE at Syracuse University. For more information, please contact [surface@syr.edu](mailto:surface@syr.edu).

## ABSTRACT

The Deep Underground Neutrino Experiment (DUNE) is a planned long baseline neutrino experiment. The detector will be comprised of four modules with 10kt of active volume each, making it an ideal target to neutrino oscillation physics and searches for proton decay. ProtoDUNE-SP was a single-phase liquid argon time projection chamber - a prototype for the first far detector module of DUNE with an active volume of 700 tons operating until 2020. It was installed at the CERN Neutrino Platform and took particle beam and cosmic ray data over its two year lifespan. Liquid argon scintillation light is still an active subject of study with open questions about the impact of scattering and absorption in such a large detector. Here, we combine ProtoDUNE-SP cosmic-ray data with its large photon detector coverage and large drift volume to measure the Rayleigh scattering length of pure liquid argon, nitrogen contaminated argon, and a xenon doped nitrogen – argon mixture. The rayleigh scattering length of the xenon mixture was then implemented in a study of the proton decay sensitivity of a single DUNE module, to see the effects of xenon doping.

---

# Characterization of Scintillation Light in Large Liquid Argon Detectors and the Implications for Proton Decay Searches

---

Kyle Spurgeon

B.S. University of Northern Iowa, 2016

DISSERTATION

Submitted in partial fulfillment  
of the requirements for the degree of  
*Doctor of Philosophy in Physics*

Syracuse University

July, 2022

Copyright Kyle Spurgeon, 2022

All Rights Reserved



*To those who visit here, we wish a safe journey and the joy of discovery.*

## Appreciation

As the old adage goes, it takes a village. The work completed in this document has been no exception to this.

First, and endless amount of appreciation must go to my wife, Sarah. The endless encouragement and support you have given me through this journey is unmatched. Through many sleepless nights, weeks away, and work done on vacation, you've pushed me to keep going and growing. This work would not be completed without you.

To my mother, who told me I could do great things if I wanted to, and supported me even though it meant I kept moving farther and farther away.

To Jeremiah, Ross, Nick, Justin, and Steve. A little realism and a lot of embarrassing memories from high school kept me rooted, and reminded me that friends are always close.

To Matt, Noah, John, Cassara, Jack, Andrew, Jory, Joe, and David. I would not have even survived my undergraduate studies without brighter people to support and encourage me. There is even less chance on me ending up here if I hadn't been introduced to the outdoors and rock climbing clubs at UNI. Truly, my trajectory would have been wildly different without your friendship and support.

To the entire cohort of graduate students who joined me in my first year as SU. Support is the story of our success. I know you will all do great things, I couldn't have any more faith in the abilities of a group of people.

To my colleagues on DUNE, Richie, Chris, Erin, Jon, Dante, Luca, Niccolo, and so many more. Thank you for all of the support and guidance you've given me. Thank you for the fun and encouraging

times over coffee. Thank you for correcting my mistake and teaching me how to improve. Thanks for leading the way.

Endless thanks go to Bryan Ramson, for taking me under his wing when I needed support, and for continuing to work with me and inspire me throughout my entire Ph.D. This work is as much yours as it is mine.

To Abhilash, my partner in neutrinos, thank you for learning with me and developing this group. Being two new researchers in this wide world was challenging, but the support of a good office mate eases all burdens.

Finally, to Denver, thank you for taking a chance on me. The knowledge you've instilled in me over the last four years has shaped me as a physicist, researcher, coder, and a person. Advising two new students and building a family in a new place is far from an easy challenge, but you always made time to make sure I was where I needed to be and had the support I needed to keep going. You always had answers to questions big or small (or unnecessary), and always gave them to me at a level that made me feel more like a colleague and less like a student. I've grown a lot under your guidance and will always be thankful for it.

*Syracuse, New York*

*June, 2022*

# Contents

## List of Figures

# List of Tables

# Characterization of Scintillation Light in Large Liquid Argon Detectors and the Implications for Proton Decay Searches

## Chapter 1

# The Standard Model, Neutrinos, and Proton Decay

Neutrinos are the most abundant massive particles in the universe, but are also one of the most challenging particles to detect. The existence of neutrinos was predicted in 1930, but it took nearly three decades for proof of their existence to be observed. This prediction originally necessitated that neutrinos be massless particles, much like the photon, to maintain symmetries and uphold momentum and energy conservation laws. In 1957, a prediction that neutrinos were actually massive opened the door for new theoretical models, and the confirmation of neutrino mass in 1998 by the Super-Kamiokande[1] experiment changed how physicist saw the universe. In this section, I will briefly describe the Standard model, the compilation of theories and discoveries that best defines our universe, as well as its components. I will then discuss the properties of neutrinos in more detail, before addressing some open questions about and extensions to the Standard Model.

### 1.1 The Standard Model

The Standard Model (SM) of particle physics represents the current understanding of particles and their composition and behavior in the universe. The SM describes the fundamental particles that exist in the universe: leptons, quarks, and bosons, as well as most of the forces through which



they interact. The SM has provided accurate explanations about the existence and interactions of most elementary and composite particles in recent years. The theory itself is a quantum field theory, where the fields are the fundamental objects and particles are the quanta of the fields. The particles interact via mediary fields. These interaction forces, the electroweak ( a combination of the electromagnetic and weak forces) and strong force, are described in a similar way, where the force is represented by a field and the quanta of which is the particle which mediates the field. These particles are the force carrying bosons: photons, W, Z, and gluons.

Another boson exists in the SM, the scalar boson called the Higgs, mediated by the Higgs field. The search for the Higgs boson, which was proposed by Peter Higgs in 1964[2], helped to propel particle physics into the modern era. The standard model also includes the coupling strength of the elementary particles with the fields. These coupling strengths describe how strongly each particle interacts with each force, in the case of the Higgs this coupling describes how much mass a particle gets from the field. In the cases of the vector boson fields, these couplings can be used to calculate particle decay rates and interaction cross sections. A precise understanding and measurement of these quantities is important, since these quantities are inherent to the SM and can be used to validate the model's accuracy.

To date, the SM has successfully described all of the elementary particles: the quarks and leptons. The theory predicts 6 leptons and 6 quarks, both separated into 3 "generations", generally organized by mass. Each generation is composed of a pair of particles, which are complementary particles in the field theories. The first and lightest generation of quarks is the up and down quark, the second is the charm and strange, while the third is the top and bottom quark. The leptons follow this pattern, having three "generations" of lepton pairs. The lightest lepton is the electron, then the muon, and finally the tau. There is a flavored neutrino to compliment each of these leptons. The current composition of the SM can be seen in figure 1.1.

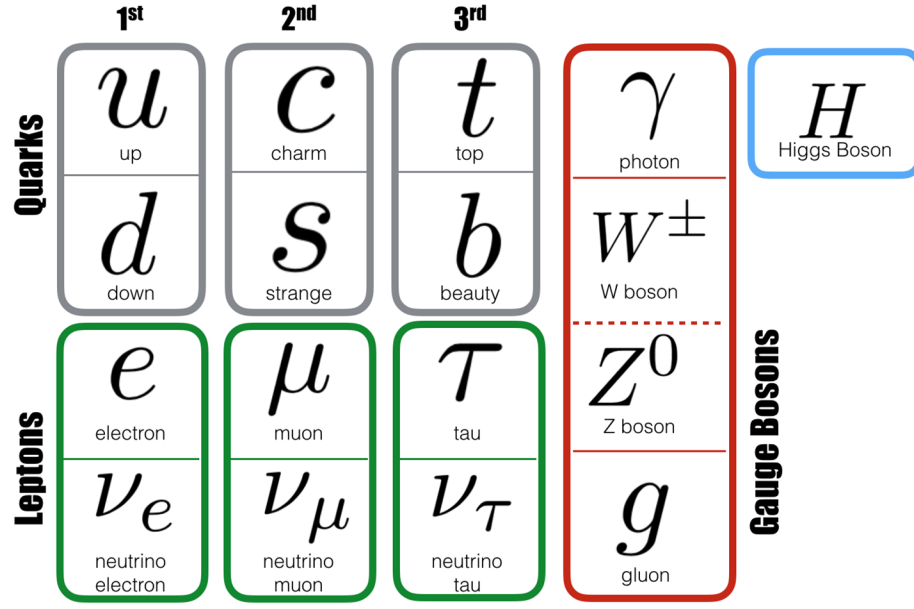


Figure 1.1: The current representation of the standard model[3].

### 1.1.1 Gauge Bosons and Forces

Gauge bosons are the quanta of the fields that permeate all space and mediate the forces associated with the boson. These fields originate in the theory from the necessity of gauge invariance, stemming from the local symmetry group that the SM is based in

$$SU(3) \times SU(2) \times SU(1) \quad (1.1)$$

The  $SU(3)$  term gives rise to the strong nuclear force, which couples to a property called color. All particles that experience the strong force, the quarks and gluons, have this property. There are three colors, red, blue, and green, as well as their anti- counterpart. The strong force is mediated by eight gluons, which interact with the quarks, annihilating quarks of one color and producing quarks of another color in a given interaction. Since, as stated, the gluons themselves carry a color, the overall color of the interaction is conserved despite the input and output quarks changing color themselves.

The  $SU(2) \times SU(1)$  term gives rise to the electromagnetic and weak forces. These two forces were originally described separately, but have since been reconciled as a single electroweak force. The first gauge boson that arises from this symmetry is the massless photon, propagator of the electromagnetic force. The photon couples to electric charge, which carries a positive or negative multiplier of the fundamental charge  $e$ . The other two bosons that arise from this symmetry and mediate the weak force are the  $Z$  and  $W^\pm$  bosons. The  $Z$  mediates the weak neutral interactions, and the  $W^\pm$  mediates the charged weak interactions.

### 1.1.2 Quarks and Hadrons

There are six quarks contained in the SM. These elementary particles interact via both the electroweak and strong force. Their generation, charge, and mass is shown in table 1.1. Each individual quark carries an electric charge, equal to  $\frac{2}{3}e$  for the up, charm, and top, and equal to  $-\frac{1}{3}e$  for the down, strange, and bottom. Quarks of positive charge are grouped into the "up type" quarks, while their negatively charged counterparts are grouped into "down types", for classification purposes. These quarks also carry a color charge, which is analogous to the electric charge. A combination of colored and anti-colored quark produce a colorless product, and a combination of all three colors produces a similarly colorless product. The fact that gluons carry colors gives rise to "color confinement", which necessitates that free particles can carry no color. This leads to quarks forming very specific combinations, forming a color - anti-color pair or a grouping of three different colored quarks. The particles formed from these grouping are called mesons and baryons, respectively, which all fall into the grouping of hadrons.

In addition to the strong force behavior described above, quarks are also affected by the weak force. The interaction with the weak force of quarks behaves similarly to the weak interactions in the lepton sector. Namely, the charged  $W$  bosons interact with quarks, changing the charge of the quark by  $1e$ , and effectively shifting quarks from the up to down type in a charge weak interaction. This interaction typically works in the field theory if one of two conditions are met, either these tran-

Quark	Generation	Mass ( $MeV/c^2$ )	Charge (e)
u	1	2.4	2/3
d	1	4.8	-1/3
c	2	1270	2/3
s	2	104	-1/3
t	3	$1.712 \times 10^5$	2/3
b	3	4200	-1/3

Table 1.1: The characteristics of the six quarks that exist in the framework of the standard model

sitions can only happen inter-generationally ( $u \rightarrow d, s \rightarrow c, t \rightarrow b$ ), or these interactions need to interact with a superposition of the quarks flavor states. Intra-generational weak interactions in hadrons have been observed experimentally, such as the  $\Lambda \rightarrow pe^- \nu_e$  beta decay[4]. These observations of flavor changing charge current interactions in the quark sector led to the development of the Cabibbo-Kobayashi-Maskawa (CKM) mixing matrix[5][6]. The elements of the mixing matrix indicate the likelihood of a quark transitioning to a quark of a different generation. Within the CKM matrix, the diagonal elements of this matrix are much bigger than the off-diagonal elements, suppressing the intra-generational transitions.

Baryons are perhaps the most familiar of these hadrons, including protons ( $uud$ ) and neutrons ( $udd$ ). There are higher energy versions of these same quark combinations, or particles that have the same quarks composition but different inherent angular momenta. Mesons are generally slightly less familiar particles. Mesons are comprised of a quark - anti-quark pair or a superposition of these states. All hadrons are assigned a baryon number, equal to  $1/3(n_q - n_{\bar{q}})$ , where  $n_q$  is the number of quarks and  $n_{\bar{q}}$  is the number of anti-quarks. All baryons have a baryon number of +1, anti-baryons -1, and mesons 0. This baryon number is a conserved quantity in particle interactions.

### 1.1.3 Leptons

The leptons of the Standard Model are the  $e, \mu, \tau$ , and their companion neutrinos,  $\nu_e, \nu_\mu, \nu_\tau$ . These particles have also been designated a lepton number, equal to 1 (-1) for (anti-) leptons, which is absolutely conserved in particle interactions. These particles are all colorless, with the leptons having

lepton	Generation	Mass ( $MeV/c^2$ )	Charge (e)
$e$	1	.511	-1
$\nu_e$	1	-	0
$\mu$	2	105.7	-1
$\nu_\mu$	2	-	0
$\tau$	3	1777	-1
$\nu_\tau$	3	-	0

Table 1.2: The characteristics of the six leptons that exist in the framework of the standard model

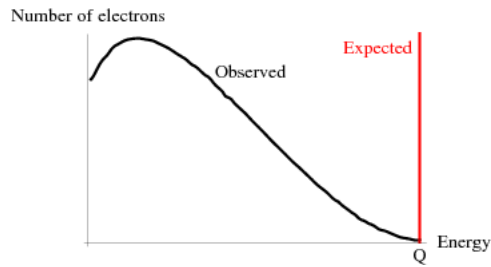


Figure 1.2: Energy distribution of the electron emitted from a beta decay reaction as measure by [8].

charge  $-1e$  and the neutrinos being chargeless. The neutrinos are therefore the only particles in the SM that interact exclusively with the weak force. This is not the only property of neutrinos that make them unique, interesting particles.

## 1.2 Neutrinos and Neutrino Oscillations

Neutrinos are abundantly produced in the universe, since the lepton conservation law leads to their production in many processes, such as solar fusion. Despite their abundance, neutrinos exclusively interact via the weak force which, aptly named, is relatively weak and leads to small interaction cross-sections. This fact is then compounded by the mass of the neutrino, which is currently unmeasured but understood to be less than 2 eV [7]. Within the SM, neutrinos are modeled as massless particles, so the observation of a neutrino mass necessitates an extension to the SM, allowing for a mechanism to give the neutrinos mass.

Neutrinos were first postulated in 1930 by Wolfgang Pauli. The origin of this idea came from observation by J. Chadwick et al. of a smooth energy distribution in beta decay analyses[9], shown in

figure 1.2. Today, beta decay is well known to take the form

$${}^A_ZX \rightarrow {}^A_{Z-1}X' + e^\pm + \nu \quad (1.2)$$

But in Pauli's time this particle had yet to be postulated, and the output of beta decay was taken to be a single electron of varying energy. This decay of a particle at rest to a single traveling electron violates the law of conservation of energy (as well as momentum and angular momentum), and reconciliation was necessary. Pauli postulated the existence of an invisible particle, at the time named the neutron, to fill this role. This idea, and name, was in contention for some time, as other theories had been proposed to explain this issue, such as Bohr's theory of statistical conservation [10]. However, it would be this interaction that would lead to observation of the neutrino.

Beta decay research contributed another key feature of the SM during this era. Within the SM a symmetry of parity exists, which states that directional interactions or moving objects mirror themselves if you invert  $[\vec{x} \rightarrow -\vec{x}]$  the coordinates). This has been shown in EM and strong interactions, but a probe into the weak interaction using beta decays has shown that the weak interaction does not conserve parity symmetry [11]. This breaks a symmetry that was believed to be fundamental, and introduces exciting complications to physics.

In 1956, Clyde Cowan and Frederick Reines et al published the detection of the neutrino using beta capture[12], the inverse of the beta decay. In this process, a neutrino interacts with a proton, emitting a positron and a neutron. They observed this by placing water near a nuclear reactor and looking for traces of photons, which were the product of a positron annihilation. The two produced photons were detected in a scintillator material and proved the existence of the neutrino.

At the time, the neutrino was postulated to be massless, as there was no experimental data to support a massive neutrino. The first complication with this assumption came from the observation of neutrinos traveling from the sun, referred to as solar neutrinos. The fusion process occurring in the sun is relatively well understood, even around the time of the neutrinos observation. There was

an understanding of the number of electrons produced in the fusion reaction, and due to lepton conservation, also the number of  $\nu_e$ .

In 1960, Raymond Davis pioneered an experiment in the Homestake mine of South Dakota. The experimental setup included a 100,000 gallon tank of dry-cleaning fluid placed in the mine. This fluid contains chlorine-37, which transforms into argon-37 and an electron when an electron neutrino collides with it. The argon-37 can then be extracted and counted, recording the number of neutrino interactions from the sun. John Bahcall provided a theoretical calculation for the expected number of  $\nu_e$  interactions expected in the experiment, and the Davis experiment recorded nearly one-third of the expected neutrinos[13]. This experiment was the first evidence of the solar neutrino problem, which would go unsolved for nearly three decades.

### 1.2.1 Neutrino Oscillations

In 1957, Bruno Pontecorvo used neutral kaon oscillation as the basis for an explanation for the solar neutrino problem[14]. Essentially, if the neutrino also existed in a both a flavor and mass eigenstate pair, then the oscillation from one flavor state to another would explain why we observe fewer  $\nu_e$  from the sun than we would expect. As stated, though, this necessitates the introduction of a *mass eigenstate* to the *massless* neutrino, and that these mass eigenstates would have to differ from the flavor eigenstates. These had already been seen, and explained, in the quark sector. The theory bridges well to the lepton sector as well, and led to the development of the Pontecorvo-Maki-Nakagawa-Sakata (PMNS) matrix[15]. The PMNS matrix is represented in equation 1.3 in the typical forms, first with the arbitrary operators followed by the notation where  $s_{ik}(c_{ik})$  represent the sine(cosine)  $\theta_{ik}$ , where  $\theta_{ik}$  is the mixing angle between the two flavors. This matrix explains the mass-flavor mixing in the neutrinos, as shown in equation 1.3, where the flavor states are superpositions of the mass states. Weak interactions with neutrinos affect and produce only these flavor eigenstates, but the SM hamiltonian interacts with the mass eigenstates, meaning that time-operations oscillate the flavor states of the neutrinos.

$$\begin{aligned}
\begin{pmatrix} \nu_e \\ \nu_\mu \\ \nu_\tau \end{pmatrix} &= \begin{pmatrix} U_{e1} & U_{e1} & U_{e1} \\ U_{\mu 1} & U_{\mu 1} & U_{\mu 1} \\ U_{\tau 1} & U_{\tau 1} & U_{\tau 1} \end{pmatrix} \begin{pmatrix} \nu_1 \\ \nu_2 \\ \nu_3 \end{pmatrix} \\
&= \begin{pmatrix} c_{12}c_{13} & s_{12}c_{13} & s_{13}e^{-i\delta} \\ -s_{12}c_{23} - c_{12}s_{23}s_{13}e^{i\delta} & c_{12}c_{23} - s_{12}s_{23}s_{13}e^{i\delta} & s_{23}c_{13} \\ s_{12}s_{23} - c_{12}c_{23}s_{13}e^{i\delta} & -c_{12}s_{23} - s_{12}c_{23}s_{13}e^{i\delta} & c_{23}c_{13} \end{pmatrix} \begin{pmatrix} \nu_1 \\ \nu_2 \\ \nu_3 \end{pmatrix} \quad (1.3)
\end{aligned}$$

$$|\nu_\alpha\rangle = \sum_{i=1}^3 U_{\alpha i}^* |\nu_i\rangle \quad (1.4)$$

Neutrino oscillations take the form shown in equation 1.5, stating that any flavor state neutrinos observed is a sum of the three mass states with coefficients defined by the PMNS matrix. In the standard way, we can apply a time dependent operator to this state:

$$|\nu_\alpha(t)\rangle = e^{-iHt} |\nu_i(0)\rangle \quad (1.5)$$

where  $|\nu_\alpha(t)\rangle$  is the state of the neutrino at some arbitrary time  $t$ ,  $|\nu_\alpha(0)\rangle$  is the initial state, and  $H$  is the hamiltonian. Working under the standard convention that  $(c, \hbar, \text{most constants}) = 1$ , and expanding the hamiltonian under the approximation that the neutrino energy  $\gg$  the neutrino mass we get:

$$|\nu_\alpha(t)\rangle = e^{-iE_i t} |\nu_i(0)\rangle \quad (1.6)$$

$$= e^{-i\sqrt{p^2+m^2}t} |\nu_i(0)\rangle \quad (1.7)$$

$$= e^{-ip + \frac{m^2}{p^2}t} |\nu_i(0)\rangle \quad (1.8)$$



Further, if we then want to detect a  $b$  neutrino as an  $a$  neutrino at some later point, we have to observe it in the fashion

$$\langle \nu_\alpha | \nu_\beta(t) \rangle = \sum_i U_{\alpha\beta}^* U_{\alpha\beta} e^{-iE_i t} \quad (1.9)$$

where the sum over  $i$  is a sum over the mass states. Here, we need to make some simplifying approximations. As we know, neutrinos have very little mass and are relativistic particles, in this regime,  $E \approx p$ , since  $p \gg m$ . Also in this relativistic, unitless world, the time travelled is  $\approx$  the distance travelled, since  $d = vt = ct = 1t = t$ . This allows us to simplify equation 1.9 and find the observation probability as a function of observables.

$$P(\nu_a \rightarrow \nu_b) = |\langle \nu_a | \nu_b \rangle|^2 \quad (1.10)$$

$$= \sum_{i,k} U_{ai}^* U_{bi} U_{ak} U_{bk}^* e^{-i\Delta E t} \quad (1.11)$$

$$= \sum_{i,k} U_{ai}^* U_{bi} U_{ak} U_{bk}^* e^{-i\frac{\Delta m_{ab}^2}{2E} L} \quad (1.12)$$

where  $\Delta m_{ab}^2 = m_a^2 - m_b^2$  is the mass splitting, or difference in the magnitude of the masses  $\nu_a$  and  $\nu_b$ .  $L$  is the distance travelled from the origin and the observation point, chosen as  $L$  instead of, say,  $x$  or  $d$  because it is beneficial to put this in experimental terms.  $L$  here represents the baseline, or length, between the neutrino's origin and the detector location.

It can be seen that the observation probability for neutrinos is dependent on the distance travelled, the energy of the neutrinos, the mass differences, and the PMNS matrix, which is comprised of the mixing angles and the charge-parity(CP)-violating phase  $\delta$ . This leaves a lot of open questions for neutrino physics, and these values have been the subject of many experiments in recent years. The availability of many different neutrino sources lends itself well to a diversified experimental land-

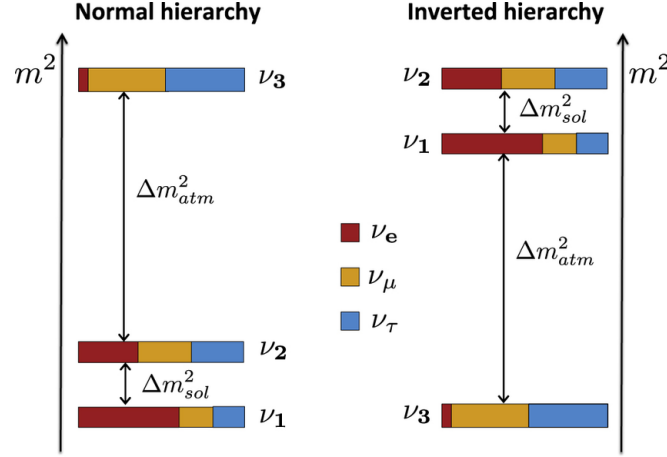


Figure 1.3: A representation of the mass hierarchy problem within neutrino physics.

scape that works together to answer these questions. As an example, there are three mass splittings,  $\Delta m_{3,1}^2, \Delta m_{2,1}^2, \Delta m_{3,2}^2$ . It can be worked out that two of these three splitting are independent, taking the form  $\Delta m_{3,2}^2 = \Delta m_{3,1}^2 - \Delta m_{2,1}^2$ . From oscillation experiments, we know that  $\Delta m_{3,1}^2 \gg \Delta m_{2,1}^2$ , and  $\Delta m_{2,1}^2$  is positive[16]. This leaves the final ordering to be discovered, the final neutrino mass hierarchy and the sign of  $\Delta m_{3,2}^2$  is just one open question.

### 1.2.2 Neutrino Interactions

Neutrinos interact exclusively through the weak force, which is well defined and leads to two different types of interactions, following the existence of two bosons mediating the force. The exchange of a  $Z$  is described as a neutral current (NC) interaction, and the exchange of a  $W^\pm$  as a charged-current (CC) interaction. In both of these interactions, all of the previously described conservation laws apply. Charge, lepton flavor, and kinematic quantities must all be conserved. This leads to a general form for both of these interactions, with the CC(anti)neutrino interactions producing the paired (anti)lepton, and the NC (anti)neutrino interactions producing a (anti)neutrino of the same flavor of the interacting particle. Equations 1.13 and 1.14 show the general forms of the CC and NC

interactions, respectively.

$$\nu_\ell + N = \ell^- + X \quad (1.13)$$

$$\bar{\nu}_\ell + N = \ell^+ + X$$

$$\nu_l + N = \nu_l + X \quad (1.14)$$

$$\bar{\nu}_l + N = \bar{\nu}_l + X$$

### 1.2.3 Physics with Neutrinos

The neutrino sector carries a lot of interesting effects and open questions within the SM. As discussed during the explanation of neutrino oscillations, there is a term built into the PMNS matrix that quantifies the CP violation in the neutrino sector. As we know, the weak interaction is known to violate parity symmetry[11]. This asymmetry is explained by making the weak interaction a theory in which only left-handed particles and right handed anti-particles participate in the weak force. This introduces enough oddities into the SM, but the implicit dependence on CP violation in neutrino oscillations further complicates the matter. The idea of a charge-parity violating decay has been measured in kaon oscillations, which were shown to violate this in the 1960s[17]. The CP violating phase in the neutrino sector is one of the biggest open questions in the field, as  $\delta_{cp}$  could be 0, or could be a maximal value, both of which have large physics implications.

Neutrinos are also the only particles described in the SM that have the potential to be Dirac or Majorana particles, meaning that there is some chance that they are their own anti-particle. This idea was originally proposed by Ettore Majorana[18] as a general theory, but the massive, chiral, neutral charged nature of the neutrinos make them the final candidate for this odd characteristic. If proven, this could have implications on the number of neutrinos, as well as the field theory that explains them.

Though the number of generations in the SM produces a nice symmetry, the ambiguity in the neutrino sector leaves many doors open. Experiments and theory show the potential for *more* neutrino flavors. The idea of a sterile neutrino, or a neutrino that only interacts via gravity but which can still be oscillated to, has been postulated[19]. In the 1990s, a well know neutrino experiment called the Liquid Scintillator Neutrino Detector (LSND) observed some evidence for sterile neutrinos[20] with the MiniBooNe experiment seeing some evidence also in the last decade. This is still a very active field of research within the theoretical and experimental neutrino world.

There is also the open question of what mechanism gives the neutrinos their mass, and what effects did this have during the formative years of the universe. There is an imbalance of matter and anti-matter within the universe. This asymmetry is unexpected, since a particle is formed with its anti-particle at the time of its creation, conforming to the conservation laws we see in our universe. There are a variety of mechanism that have been theorized that could lead to this not being true[21], but nothing has been experimentally confirmed yet. The idea of neutrinos being their own anti-particle would be one such mechanism to create such an asymmetry[22]. There are also a variety of higher dimensional field theories that could explain this imbalance, and a full understanding of the neutrino's characteristics and their implications on the SM could help shine some light on these questions.

### 1.3 Proton Decay

Protons, as of now, are the hallmark of longevity within our universe. A decaying proton, either free or bound, has never been observed. All higher energy hadrons decay, as one might expect, to lower energy states. Free neutrons have been observed to decay[23] in the form of beta decay, which is the decay of a neutron into a proton, shown in figure 1.4. Positive beta decay has been observed, where a proton bound inside a nucleus decay into a neutron, and emits a positron. This is, however, not possible for a free proton like it is for a free neutron, because there is no phase space in the system for a proton to decay.  $\beta^+$  decay is possible when the resulting nucleus has a lower energy

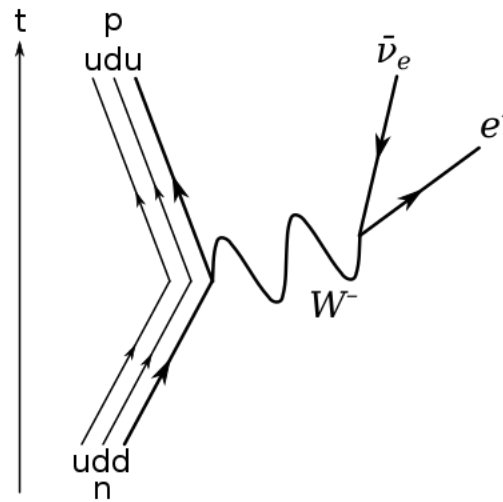


Figure 1.4: The Feynman diagram for the beta decay of a free neutron into a proton, electron, and an anti-neutrino.

than the original, in which case the nucleus gives energy to the proton to allow the transition. The conservation laws within the SM, such as baryon and lepton number conservation, do not allow the proton to decay into any lighter particles. Due to the slight mass difference, the neutron can decay into a proton. Currently, the lifetime of the proton has been measured to be greater than  $1.67 \times 10^{37}$  [24] years.

The existence of proton decay is a key feature in many theories which seek to "unify" the standard model. In these theories, all of the forces can be explained in one succinct, uniform formulation. We have already seen such a unification in the SM, with the unifying of the electromagnetic and weak forces into one theory. This lends support to the idea that there exists one single Grand Unified theory which would support and describe all the forces within the standard model. Proton decay would also provide an answer to this matter anti-matter asymmetry problem, with the decay of a proton being the key to breaking the baryon number conservation and giving us a mechanism for the creation of more matter in the current universe. Within expanded models, mechanisms for baryon number non-conservation can be included into the field theories, allowing for an avenue for the asymmetry.

In this section, I will further describe the idea of a grand unifying theory, I will mark the current landscape of these GUTs, and in more detail describe the implications and experimental methods for observing proton decay.

### 1.3.1 Grand Unified Theories

The simplest possible GUT that could fully contain the current SM is the  $SU(5)$  symmetry group[25]. This was one of the first formulations of a GUT and, though it has been disproved by the long life of the proton[26], does provide the simplest introduction to the theory of unification. The  $SU(5)$  group has  $5^2 - 1$  generators, or  $5 \times 5$  hermitian matrices. These 24 can be divided into 8, explicitly  $3^2 - 1$ , to represent  $SU(3)$  and 3 to represent  $SU(2)$ . One can then generate a single  $5 \times 5$  hermitian matrix to represent  $U(1)$ , and the entirety of the standard model can be explained by this one  $SU(5)$  theory. The introduction of this representation allows for a full re-derivation of the SM (left as an exercise to the reader), as well as built-in explanations for many questions.

We have already discussed the implications of proton decay on the formation of the universe, but this specific GUT allows us to explain other somewhat obscure questions. The quantization of electric charge is not inherent to the SM, since the  $U(1)$  generator is not quantized. However, we observe a unit charge,  $e$ . There are other, equally exotic, explanations for charge quantization, the most famous of which is probably the existence of a magnetic monopole, but this is also very far from observed at the time of writing. This quantization of charge, and the subsequent equality of the proton and electrons charges, is standard in the composition of our universe but left wholly unexplained with the confines of the SM. If atoms were not electrically neutral, matter as we know it would not exist, as a single proton would not stabilize a single electron. This instability would happen if the charges were unequal to *any* precision. The timeline of the instability, of course, is dependent on this precision, but anything other than exact equality allows room for error. The proton charge is exactly equal to the electron charge in this  $SU(5)$  representation (since the trace of the  $5 \times 5$  charge matrix necessitates that the down quark has charge  $-1/3$  that of the electron),

lending support to the idea of a GUT.

Here, I will briefly introduce an extension to the GUTs (or any field theory), called supersymmetry (SUSY). A supersymmetric theory is any in which the equations for forces and the equations for matter are the same. In SUSY models, scalar partners exist for quarks and leptons, as well as fermion partners for the bosons. Minimal SUSY models are theories in which only the absolute minimum number of supersymmetric partners exist, such as the  $SU(5)$  theory briefly described above. These theories can be expanded to include more supersymmetric partners[27], changing the expected proton lifetime. In recent years, string theory has been heavily developed as a theory of everything, in kind to a GUT, and SUSY is inherent in many forms of string theory[28].

Without going into any more detail, the SM does not have this feature, nor does the  $SU(5)$  GUT described previously. These theories are nice for particle physicists because they further answer questions that plague even these GUTs. The two main motivators for this are the strength of the gauge couplings of the three forces do not exactly unite within these GUTs, as one might expect from a *unifying* theory, but would meet at a singular point in a SUSY GUT, figure 1.5. There is also no explanation in the SM for the magnitude of strength of the fundamental forces, with a SUSY model explaining the large difference in strength of the weak and gravitational forces[29]. SUSY models also necessitate doubling the number of particles in the universe, introducing a super symmetric partner to the fundamental particles we already know. This allows for some explanations of dark matter, explaining one of the biggest lasting questions in physics.

### 1.3.2 Implications and Observational methods

SUSY was introduced in the previous sections solely because the signature of proton decay can give insights into which GUT best describes the universe. Theories predict the interaction rate of certain modes to extremely high precision, and these cross-sections vary from model to model. In some models, the branching fractions of the decay  $p \rightarrow e^+ \pi^0$  is the main decay mode[31], while in some it might be the decay  $p \rightarrow K^+ \bar{\nu}$ [25]. Proton decay (PDK) experiments look for PDK by looking for

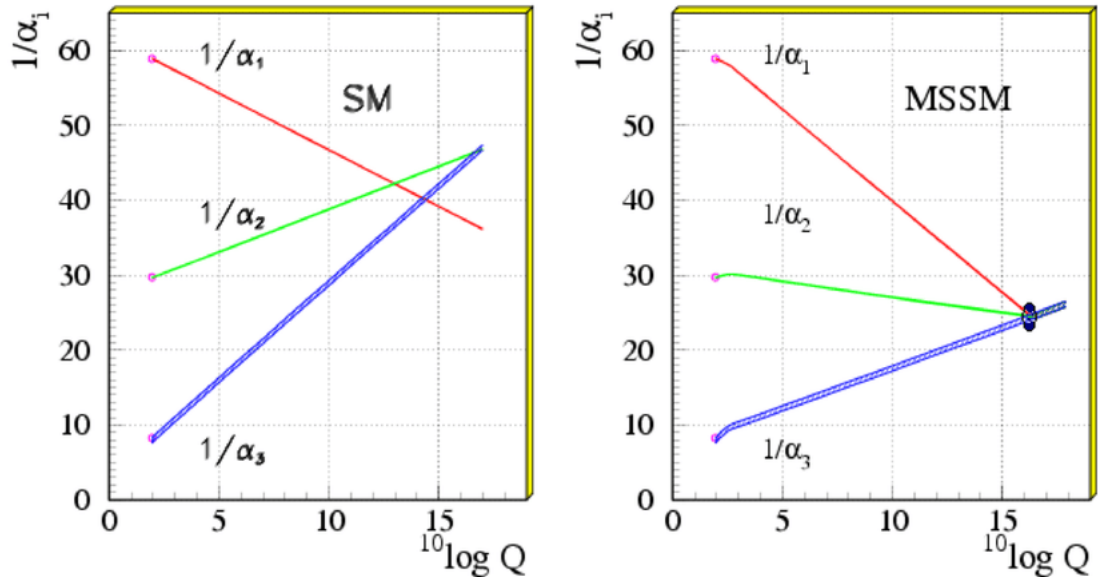


Figure 1.5: An example of the current gauge couplings (left) and a minimal supersymmetric model's gauge coupling [30]

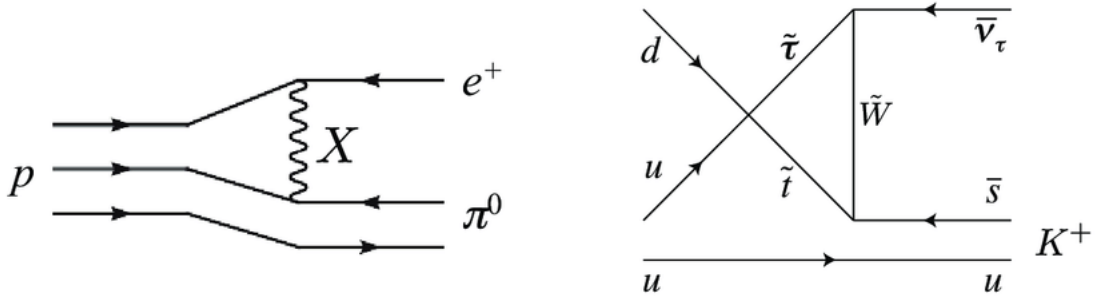


Figure 1.6: The Feynman diagram for  $p^+ \pi^0$  (left) and  $p \rightarrow K^+ \bar{\nu}$  (right).

the well defined signature for these decays.

Modern neutrino experiments look for direct observation of proton decay. The upside of these types of detectors is their good spatial and energy resolution for low energy leptons and hadrons, making it possible to observe an isolated instance of a spontaneous  $e^+ \pi^0$  appearance. Since their inception, large neutrino experiment have been putting limits on various modes of proton decay, further limiting the various competing GUTs. Large neutrino detectors are designed for characterizing the oscillation parameters from section 1.2, but the presence of large amount of protons in the detector medium and fine reconstruction abilities lend themselves to PDK detection. DUNE is planned to be



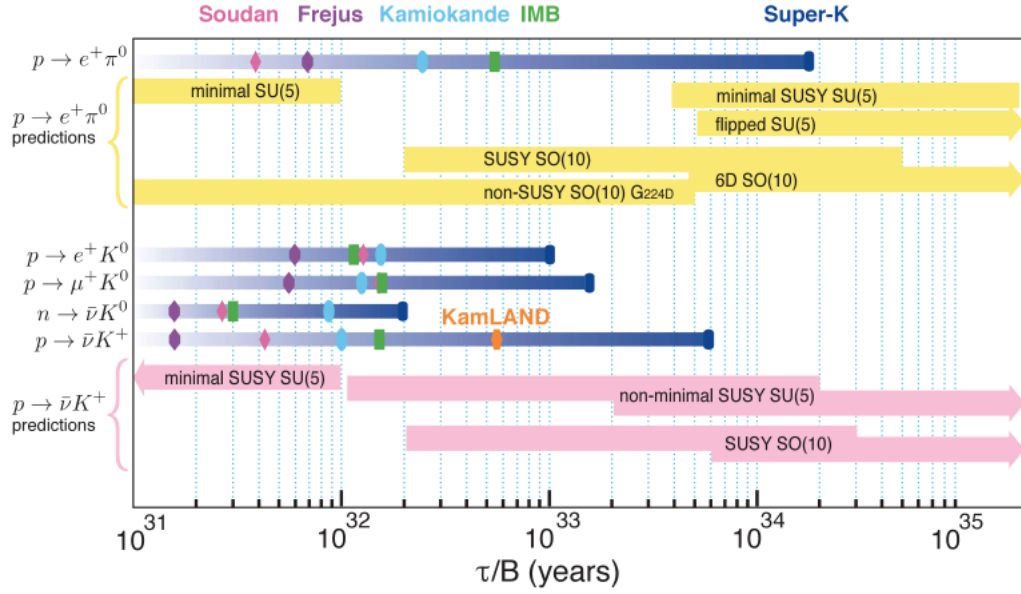


Figure 1.7: The current partial lifetime limits on various modes of proton decay, where  $\tau$  is the lifetime and  $B$  is the branching fraction, as set by neutrino detectors throughout the years. Also shown are the GUT theories and predictions in these modes.

comprised of at least two  $10kt$  modules, resulting in nearly  $10^{33}$  protons in the detector medium. Figure 1.7 shows the current limits on the proton lifetime in a variety of decay modes as set by neutrino experiments.

## Chapter 2

# The Deep Underground Neutrino Experiment

The Deep Underground Neutrino Experiment (DUNE) is a planned long baseline oscillation experiment comprised of a near detector located at Fermilab in Illinois and a far detector complex located in the Sanford mine in Lead South Dakota. The experiment will be supplied neutrinos from a megawatt-class proton accelerator which will travel the 1300km from its source at Fermilab to the far detector complex. The far detector complex will be comprised of four individual modules, each containing an active volume of at least  $10\text{kt}$  of liquid argon for a total fiducial volume of  $40\text{kt}$ . The four modules will be built in stages, with the detector design for the later stages undecided on to allow for the detector to make use of novel technologies. The first module is confirmed to be a horizontally drifted (HD) Liquid Argon Time Projection Chamber (LArTPC). In this chapter, I will discuss the LArTPC detector concept, the design of the DUNE-HD detector module, and the design and physics results of the testbed detector ProtoDUNE-Single Phase (ProtoDUNE-SP).

## 2.1 DUNE Physics Program

DUNE's main physics program is an accelerator based oscillation analysis. This program is intended to determine the oscillation parameters discussed in chapter 1, which will provide us with knowledge about CP-violation and the neutrino mass hierarchy. The beam feeding the DUNE far detector is proposed to be a  $120\text{GeV}$  proton beam. This beam will collide with a multi-layer graphite tar-

get inside a focusing horn. This process produces predominantly positive and negative pions and kaons which then decay into muon neutrinos and anti-neutrinos. The neutrino flux of this beam is  $1.65 \cdot 10^{-10} \nu/m^2$  per protons on target (POT)[32], and the energy distribution of this flux can be seen in figure 2.1. Given these expected beam fluxes, DUNE will measure the neutrino fluxes at the FD, and use the rates of  $\nu_\mu \rightarrow \nu_\mu, \bar{\nu}_\mu \rightarrow \bar{\nu}_\mu, \nu_\mu \rightarrow \nu_e, \bar{\nu}_\mu \rightarrow \bar{\nu}_e$  to fit for the oscillation parameters.

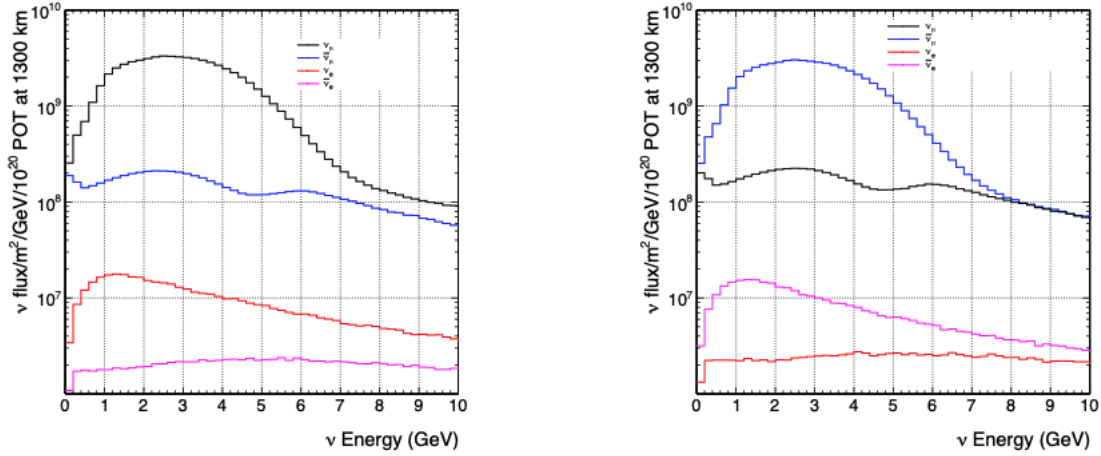


Figure 2.1: The anticipated neutrino fluxes of the beam-line supplying DUNE[32].

The expected sensitivity to these parameters can be seen in [33]. These sensitivities are promising, showing a  $5\sigma$  measurement of CP-violation in 10 years for 50% of  $\delta_{CP}$  values. In cases of maximal CP-violation, this run time could be reduced even further. Measurements of the mass hierarchy can be determined in as few as 3 years for non-maximal  $\delta_{CP}$  values, and as low as 1 year for maximal.

This oscillation physics program is intense and very promising, but the DUNE collaboration has also pioneered a very ambitious non-beam physics program. Since the number of neutrino events scales linearly with detector mass, the DUNE detector has been designed to be very large. This  $40kt$  total mass results in a lot of detector medium, which provides numerous other event detection possibilities. Natural neutrino sources, such as supernova and atmospheric neutrinos are obvious other targets for detection. The DUNE detector has been planned such that it optimizes detection efficiencies for the low energy neutrinos, as detection of a small number of supernova neutrinos

can provide invaluable insight into stellar dynamics.

The large mass of DUNE and the choice of LAr as a medium also make it a strong candidate for proton decay (PDK) detection. The LArTPC has been shown to be especially adept at detecting two specific channels of PDK,  $p \rightarrow e^+\pi^0$ , which is predicted as the dominant decay for some non-supersymmetric GUT models[31], and  $p \rightarrow K^+\bar{\nu}$ , which is the predicted dominant decay for some supersymmetric GUT models[25]. The  $p \rightarrow e^+\pi^0$  has been strongly bounded by the Super-Kamiokande water-cherenkov detector[34]. The  $p \rightarrow K^+\bar{\nu}$  decay, however, presents some challenges to this detector technology and the bounds are not set to a comparable precision. In this decay, the kaon is produced at energies below the cherenkov threshold, making this channel nearly invisible. Due to the very good energy and spatial resolution of LArTPCs, this kaon decay channel is much easier to measure in a detector like DUNE, and thus has become the primary target for PDK searches.

## 2.2 Liquid Argon Time Projection Chamber Technology

The time projection chamber detector (TPC) concept was first proposed by David R. Nygren[35] in the 1970's, with the liquid argon time projection chamber (LArTPC) pioneered by Carlo Rubbia[36] in 1977. Since its conception in the 1970's, this detector technology has been engineered and progressed to the stage where LArTPCs are at the forefront of neutrino detection technologies. The high density, low electronegativity, high scintillation yield, and low cost of argon has made it the medium of choice for these TPCs, while improvements in detector engineering and design have led to the ability to produce very large detectors. This combination of a good detector medium, and well characterized and tested detector design create a neutrino detector that has a relatively large cross-section, high triggering capabilities, and good spatial and energy resolution.

Many of these positive characteristics are intrinsic to the base design of the TPC. A TPC is comprised of three major components, a positively charged anode plane, a negatively charged cathode plane, and a drift volume. The anode/cathode plane induce a uniform electric field within the drift volume

which causes electrons to drift towards the anode plane along the shortest path. The anode plane also serves as the readout plane. The anodes are comprised of planes of conducting wires at various orientations in front of the final collection plane. These planes read the induction signal from traversing electrons drifting past allowing for two-dimensional readout. The combination of the two-dimensional charge readout, the knowledge of the drift velocity of electrons in a uniform electric field, and the drift time of the electrons through the medium, the LArTPC has an inherent three-dimensional readout complemented by fine grain energy reconstruction. This base TPC design is accompanied by a light collection system, allowing for fine-tuned timing resolution and increased energy reconstruction.

### 2.2.1 LAr Scintillation Light

A LArTPC operates under the basic principle that as an ionizing particle travels through the LAr, it creates electron-ion pairs in the Argon molecules. These free electrons, under an electric field in the detector, are the main mechanism for tracking detection. These electrons are drifted across the volume by the field and collected at the readout end. This process leaves excited argon atoms and ionized argon molecules in the detector. These excited and ionized argon molecules are in unstable states, and will drift in the detector medium looking to return to a stable state. Each type of molecule follows a specific path to stability, shown in pictorial form in figure 2.2.

The argon excimer drifts through the free space in the detector until it arrives at another argon atom. Here, there is a large probability for the excited argon atom to trap this stable argon atom, forming an excimer molecule,  $Ar_2^*$ . This is an unstable molecule and will experience a radiative decay after a short time, which separates the two argon atoms and emits a photon. In the case of an ionized argon atom, the  $Ar^+$  atom drifts in the LAr medium until arriving at a stable argon atom. For this process to continue free electrons must be present in the medium, from this and many other argon atoms being ionized by particles passing through, resulting in a free electron cloud. Once the argon ion approaches a stable argon atom in this electron cloud, they can collect a single free electron and

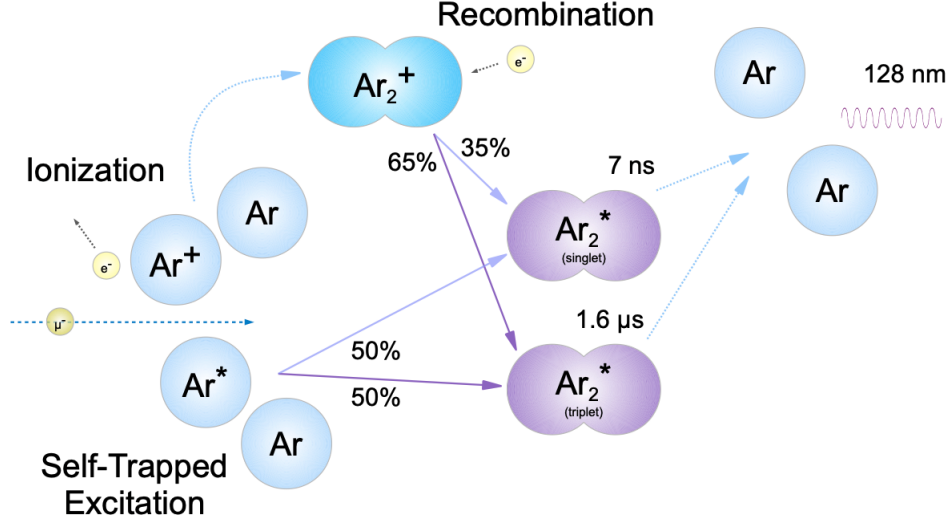
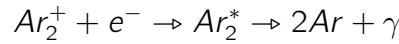


Figure 2.2: The light scintillation mechanisms for liquid argon.

recombine into an  $Ar_2^*$  excimer, which then radiates a photon as described. These two processes are shown in equation 2.1.



The dependence of the recombination of an ionized argon atom on a free electron means that the charge one can collect at the readout is decreased as one produces scintillation photons for detection[37]. This effect is seen in figure 2.3 This effect is dependent on the electric field, as a stronger field clears the electrons from the ionization region quicker, and creates a charge and light anti-correlation in the LArTPC. The ratio of the number of excited argon atoms to ionized one has been calculated[38] as

$$\frac{N_{ex}}{N_i} = .21 \quad (2.3)$$

where  $N_{ex}$  is the number of excited atoms and  $N_i$  the number ionized. The number of photons expected from this scintillation process can then be calculated from  $N_{ex} + N_i$ . The number of photons

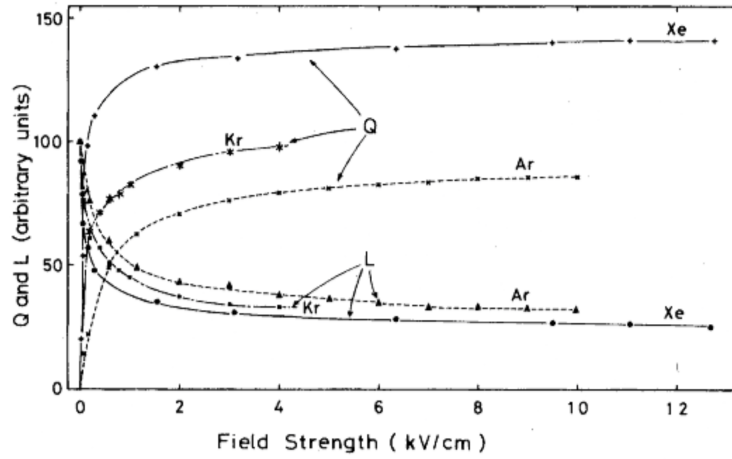


Figure 2.3: The scintillation charge ( $Q$ ), and scintillation light ( $L$ ) as a function of the field strength for xenon, argon, and krypton [37]

is proportional to the sum of these two numbers, and depends on the average energy expected per ion pair. This number has been shown to be 40,000 photons/MeV [39]. The wavelength of photon emitted from this process has been measure to high precision, with emission occurring within a ten centimeter band centered at 127nm [40], shown in figure ??.

This large number of photons makes LAr an ideal detector medium, but the *timing* of these photons is also important, especially for applications of photon detection as a detector trigger. From [41], it can be seen that there are two very low energy states that are accessible for the excimer, the  $1\Sigma_u^+$  singlet and  $3\Sigma_u^+$  triplet states. These two states have nearly identical energies relative to the ground state, but vastly different lifetimes. These lifetimes have been measured, and are known to be 6 nanoseconds for the singlet state and 1.6 microseconds for the triplet state[42]. This prompt scintillation light allows for precise timing resolution from the LAr scintillation light and allows LArTPCs to use it as a trigger.

## 2.3 DUNE-HD Detector

As stated above, the first DUNE detector module will be a horizontally drifted LArTPC. The DUNE-HD detector will be  $12.0m \times 14.0m \times 58.2m$  and have a total (fiducial) mass of 17.5 (10) kt of LAr.

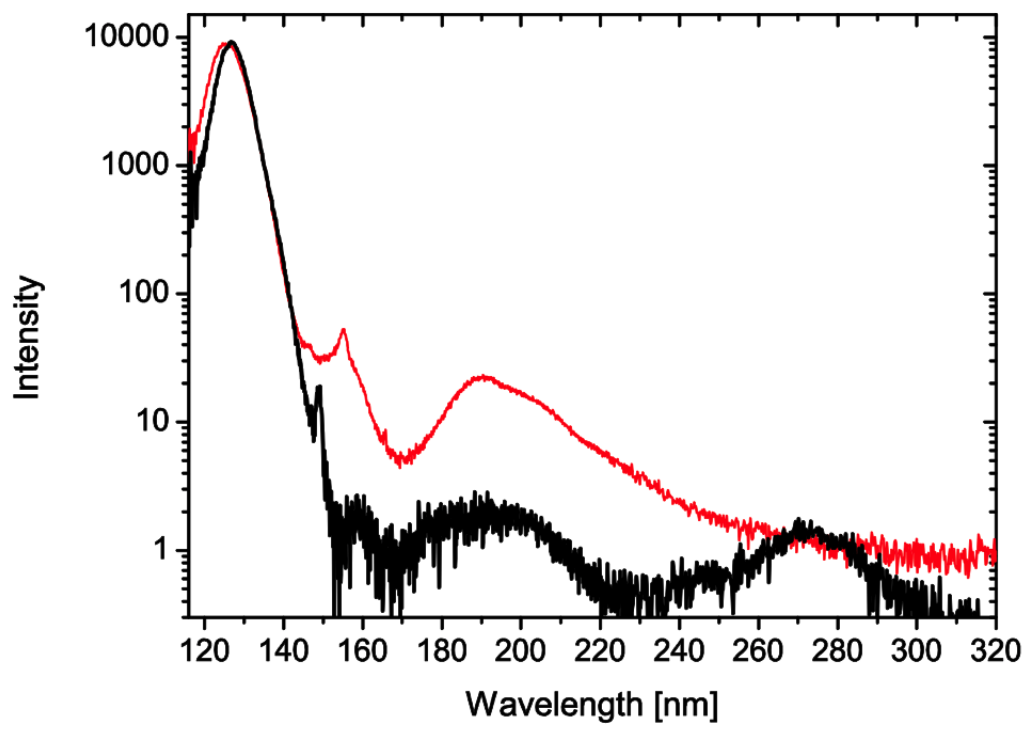


Figure 2.4: The intensity of the output spectrum from argon scintillation[40]



DUNE-HD will consist of four  $3.5m$  drift volumes which are formed between five alternating anode-cathode walls. This large TPC will serve as the first of four DUNE modules, and will be critical to the foundations of the DUNE physics program. In this section, I will describe the current design expectations for the DUNE-HD TPC and photon detection system. The full specifications for the DUNE-HD module can be found in the DUNE technical design report [33], and the description presented here will be a summary from this document.

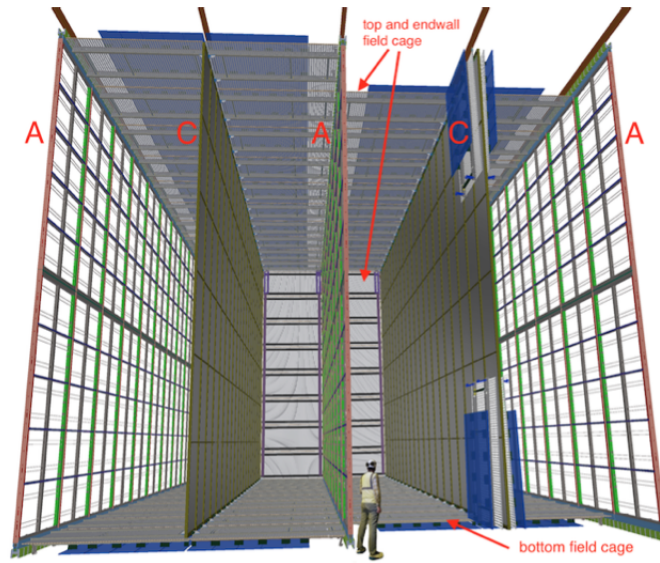


Figure 2.5: A rendering of a single 10kt DUNE module. The anode and cathode walls are labelled with A and C, respectively.

### 2.3.1 DUNE-HD Time Projection Chamber

The DUNE-HD time projection chamber will be contained inside a cryostat with exterior dimensions of  $65.8m \times 17.8m \times 18.9m$ . Inside this cryostat will be the TPC itself, briefly described in the introduction of the chapter. The drift volumes will be held under a constant drift electric field of  $500V/cm$  by anode-cathode walls. The cathode walls will be comprised of several cathode plane assemblies (CPAs), arrayed into a wall. The CPA is a single  $1.2m \times 4m$  resistive panel, and the wall will contain 150 CPAs, held at  $-180kV$ . Paired with the anode wall, held at nearly ground potential, a  $500V/cm$  E field is formed. A field-cage (FC), made of extruded aluminum, will surround the entirety of the TPC, aiding in the creation of a uniform field, with an expected deviation of less than

1%.

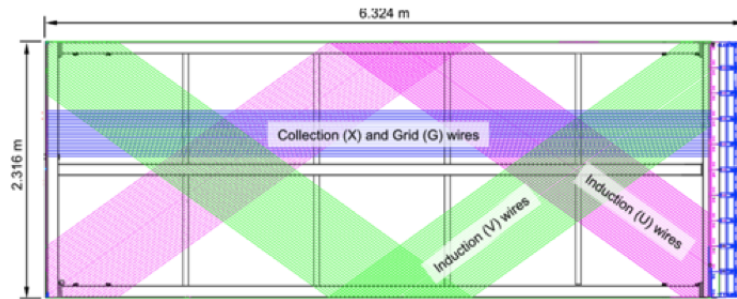


Figure 2.6: Cartoon schematic of a single APA wiring schema. The induction wires are show in green and magenta, while the collection wires are colored in blue. The inductions layers are designed to readout from either side of the APA, while the collection wires cover only one side.

The anode walls will each be comprised of 50 anode plane assemblies (APAs). These APAs are  $6m \times 2.3m$ , and will be arranged in walls 25 APAs wide and 2 APAs tall. This level of segmentation allows for easier construction and signal disambiguation. The APAs are two-sided and comprised of three active layers of wires, (U,V,X), spaced  $5mm$  apart. The X plane is the vertical collection plane, while the U,V planes are two induction planes which are oriented  $\pm 35.7 \text{ deg}$  with respect to the vertical. A drawing of this design can be seen in figure 2.6 and allows for a multi-dimensional readout. There is a fourth plane, the G plane, oriented parallel to the X plane. These wires serve as a shield, improving the readout on the induction planes. All signals from the APA are readout via the electronics, which are placed at the top or bottom, depending on the locality within the detector.

### 2.3.2 Photon Detection System

The baseline design for the DUNE-HD photon detector modules will be the X-ARAPUCA[43]. This is a novel photon detection system (PDS) design developed specifically for the DUNE physics program. Traditionally, the PDS in time projection chambers, and other neutrino experiments, would be comprised of multiple photo-multiplier tubes (PMTs). The large size and precise timing and electron resolution of PMTs make them a good and versatile candidate for these applications. However, their size can be a problem when trying to optimize the fiducial volume of a detector, especially in a large segmented detector like DUNE-HD. To increase the active volume in the DUNE modules, a

series of novel designs were created to fit the PDS within the APA planes, resulting in comparable photocoverage to a similar PMT design, but vastly increasing the active LAr volume.

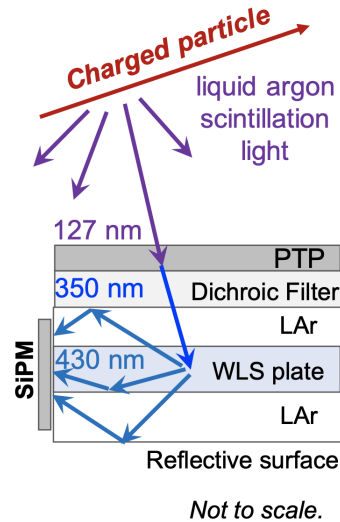


Figure 2.7: Cartoon representation of a single sided X-ARAPUCA module. The wavelength labels and arrows correspond to the photon wavelength on that side of the interfaces

The X-ARAPUCA design has been settled on for the first DUNE-HD module. The design concept is to allow light from LAr to enter the device via a wavelength shifting (WLS) plate. This first interface shifts the LAr scintillation light from the VUV to the visible spectrum. This light then passes through a dichroic filter, an optical band-pass filter that will allow this high energy light through and not allow lower energy photons back through. The trapped photon then interacts with another WLS plate. This second shift transforms the photons into the range that is reflected by the dichroic filter, and effectively traps the light within the module. The light is then free to reflect internally in the second WLS plate, as well as within the filtered cavity, before being collected on a silicon photomultiplier (SiPM) and read out. This process can be seen in figure 2.7. The design principle allows for construction of modules that only allow photons from one side, or from both sides, allowing them to be placed effectively in all APA walls in DUNE-HD.

The wavelength shifters selected for this application were chosen based on the conversion efficiency, durability, and emission wavelengths. The first wavelength shifter used in the ARAPUCA is

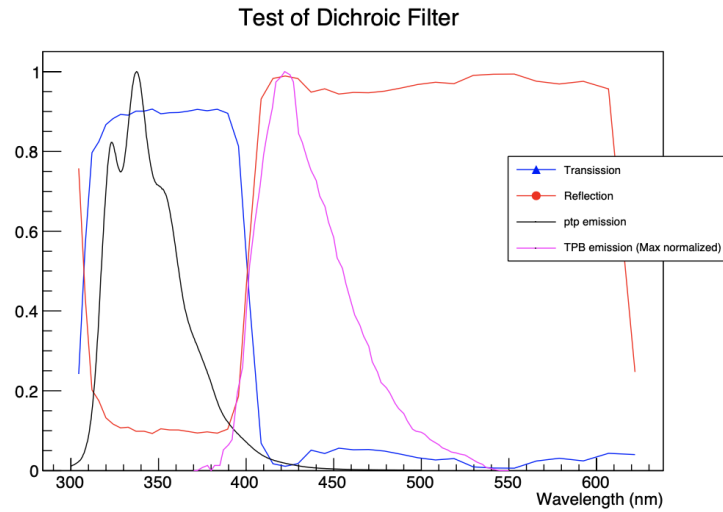


Figure 2.8: The emission spectra of the two wavelength shifters employed in the ARAPUCA design and the cutoff spectra for transmission and reflection of the dichroic filter.

p-Terphenyl (pTP). It was selected from this specific application from a variety of candidates. The actual absorption spectrum of pTP in the VUV region is somewhat unknown, but it has also been shown to have a relatively high emission yield in LAr application, where the number of scintillation photons is well understood. The emission spectrum of pTP is peaked at 340nm, which places it well within the efficient absorption region of the second WLS, and outside of the emission spectrum, making it an effective first WLS layer. The second shifter is tetra-phenyl butadiene (TPB), and is a well known and characterized WLS that is the standard for VUV photon shifting in LAr. Similar to pTP, the exact VUV absorption spectrum for TPB is not currently well known, but it has been experimentally shown to have high emission yields in LAr scintillation scenarios, and the emission spectrum, shown in figure 2.8 aligns well with most modern SiPM absorption ranges. The difference in the emission spectra of pTP and TPB allow for an easily designed dichroic filter that will trap the TPC emitted photons inside the reflection cavity. An overlay of the pTP emission spectrum, the designed dichroic filter transmission/reflection spectrum, and the TPB emission spectrum can be seen in figure 2.8.

This design of the PDS allows for large photo-coverage of all drift volumes. X-ARAPUCAs located in between two drift volumes will accept photon from both sides, and this light signal will be assigned

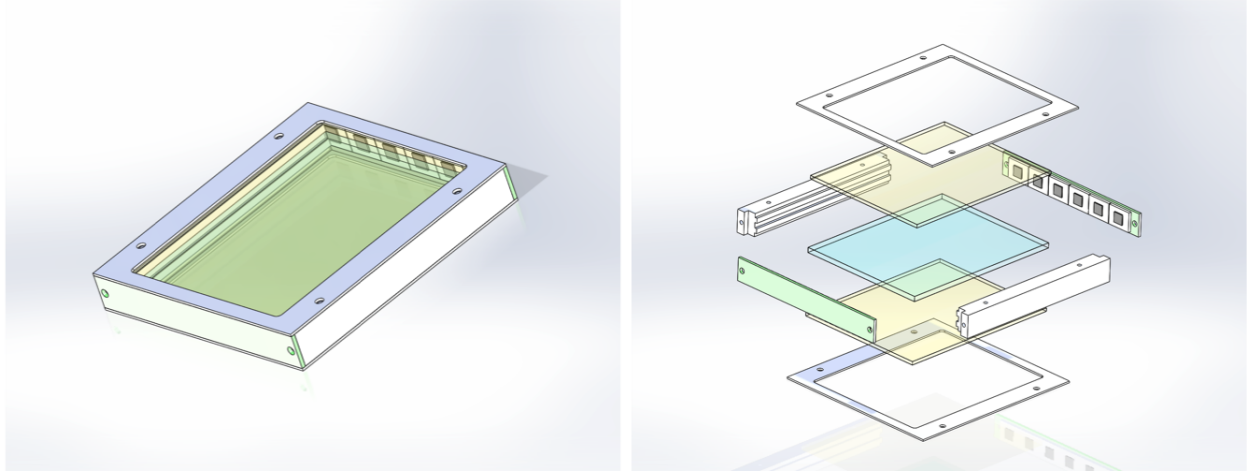


Figure 2.9: A design schematic for the X-ARAPUCA, the baseline design for the DUNE-HD photon detection system.

to the appropriate drift volume by time-matching this signal to the tracking system or other PDS modules, effectively segmenting the PDS. The X-ARAPUCAs themselves are also highly segmented. This is done partially for ease of build, integrity of components, and collection efficiency, but also allows the PDS to have some inherent spatial resolution. A drawing of one of these X-ARAPUCA modules can be seen in figure 2.9, while the installation idea within the APA can be seen in figure 2.10. These X-ARAPUCAs have a measured efficiency of 2.9%[44].

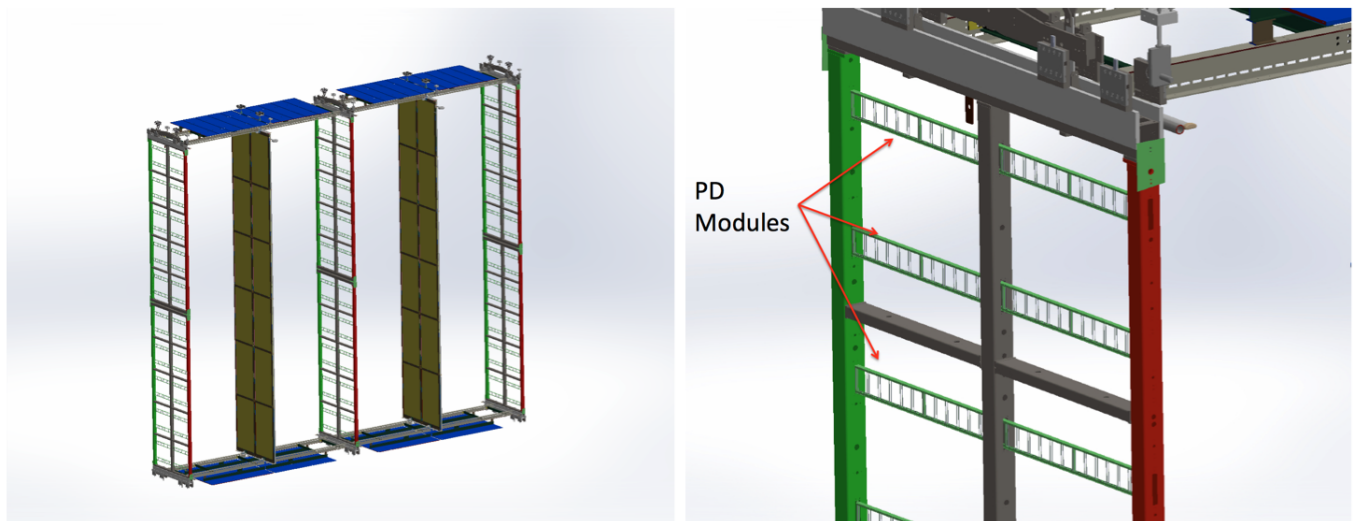


Figure 2.10: Design of the DUNE-HD photon detector system installed within the double-height APAs.

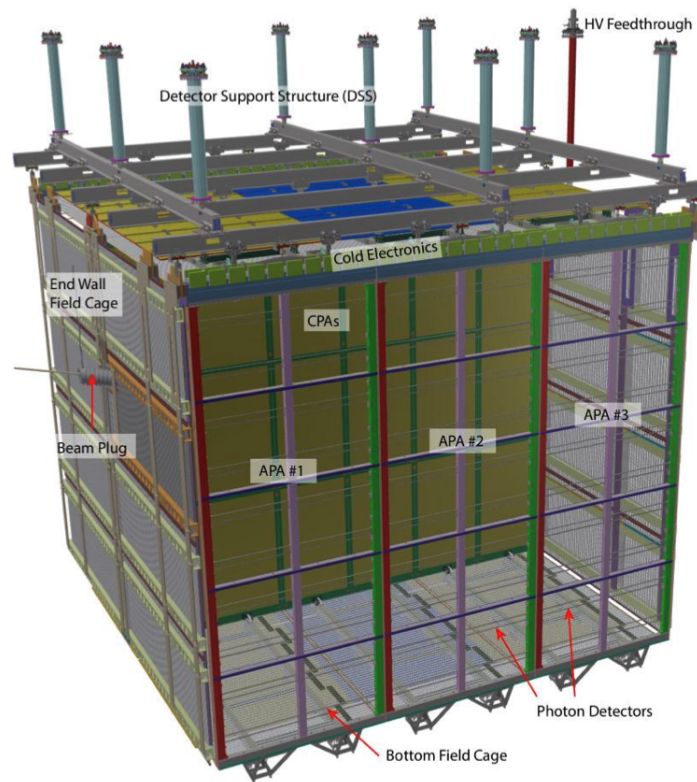
## 2.4 ProtoDUNE-SP

As a step towards DUNE-HD, the collaboration designed and constructed a set of prototype detectors at the CERN Neutrino platform, aptly named ProtoDUNE. Two detector concepts were constructed to test the single phase (SP) and dual phase (DP) LArTPC concepts, ProtoDUNE-SP and ProtoDUNE-DP. This thesis studied exclusively the single phase technology, and this section will describe the ProtoDUNE-SP detector components; the TPC, PDS, and triggering systems, as well as the campaign to dope ProtoDUNE-SP with trace amounts of xenon. This prototype detector was configured with what was, at the time, the base technologies intended for DUNE-HD, and took CERN-SPS beam supplied data in 2018, with a long campaign of cosmic ray data into 2019 and 2020 following the CERN long shut down. Since this time, ProtoDUNE-SP has been decommissioned with the intention of transitioning the technologies to the updated versions now planned for the DUNE-HD, and a data taking run after the CERN long shutdown. All specifications provided here can be found described in greater detail in the ProtoDUNE-SP technical design report[45].

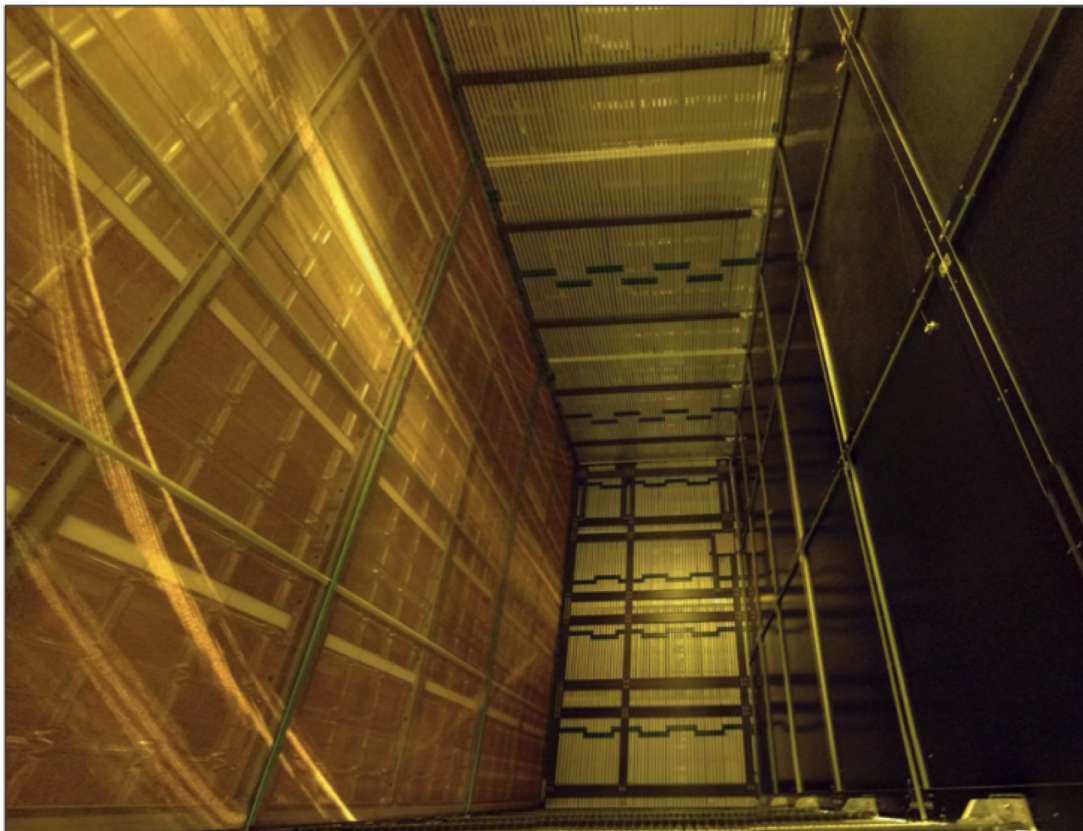
### 2.4.1 ProtoDUNE-SP Time Projection Chamber

The ProtoDUNE-SP TPC is contained within a corrugated membrane cryostat, of internal dimensions  $8.5m \times 7.9m \times 8.5m$ , making it the largest LAr cryostat ever. A rendering of the TPC design, electronics and cryostat, as well as a photo of ProtoDUNE-SP constructed inside the cryostat can be seen in figure 2.11. Within this cryostat is 770 tons of LAr, with two exterior APA planes and one central CPA plane comprising two drift volumes and the largest LArTPC ever constructed. The TPC itself has dimensions of  $7.2m \times 6.0m \times 6.9m$  with two  $3.6m$  drift volumes. To match the DUNE-HD specifications, the drift field is held at  $500V/cm$  and the APA and CPA planes are comprised of multiple singular modules. The APAs are  $2.3m \times 6.3m \times 12cm$ , with three side-by-side APAs comprising either APA plane. The APA induction wires are wound around the frame at  $\pm 35.7 \text{ deg}$ , while the collection wires are oriented vertically. A sketch of this arrangement can be seen in figure 2.12.





(a)



(b)

Figure 2.11: (a) The rendering of the completed ProtoDUNE-SP experiment and a (b) photo from the interior after construction.

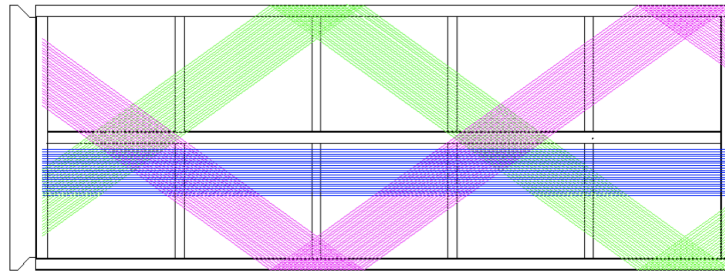


Figure 2.12: Cartoon schematic of a single APA wiring schema. The induction wires are show in green and magenta, while the collection wires are colored in blue. The inductions layers are designed to readout from either side of the APA, while the collection wires cover only one side.

The CPA plane is formed from 6 CPAs, each measuring  $1.15m \times 6.1m$ . These CPA are composed of three stacked cathode panels, constructed of a resistive, fire-retardant material, FR4. These panels are coated in commercial Kapton tape to increase the resistivity, and are biased to  $-180kV$  to provide the intended drift field. Containing both the APA and CPA planes is the field cage, as in the DUNE-HD design. The ProtoDUNE-SP field cage meets all of the requirements described in section 2.3.1, and is comprised of extruded aluminum and resistive dividers to provide the boundary conditions for the  $500V/cm$  electric field necessary for the experiment.

The entire ProtoDUNE-SP TPC is contained by and suspended in a  $8.5m \times 7.9m \times 8.5m$  membrane cryostat. A three loop LAr purification systems collects gaseous argon boil off, gaseous argon purge, and LAr condensation, and then purifies, condenses, and resupplies LAr from the bottom of the cryostat. This system was based on the current designs from ICARUS and other Fermilab experiments, and is designed to turnover the entire LAr volume in less than 5 days, while keeping the purity of LAr in the range necessary for these precision physics measurements.

The composition of this cryostat necessitates the creation and installation of a beam plug to reduce energy loss due to interaction with these materials. This plug is a cylinder constructed of grounded steel and fiberglass rings, and is filled with 1.3 bar of nitrogen gas, extending 5cm into the LAr volume. The beam plug was positioned to supply the majority of the beam particles to one drift volume, again to reduce loss due to interactions with detector components. The beam plug is placed approximately at the mid-point in height and 30cm to one side of the cathode, with a 11 deg downward



angle and 10 deg right facing angle.

The ProtoDUNE-SP particle beam is fed by the H4 beamline, the primary source of which is the SPS accelerator. A beryllium target extracts low momentum hadrons, which are then supplied to a secondary target to produce a particle beam in the range of interest, 0.1-10 GeV/c. The beamline is comprised of a time of flight measurement system, a triggering system, a momentum spectrometer, and a Cherenkov monitor to allow for particle ID. This system is described in more detail in [46]. This design also includes a configurable magnet, which allows selection of charge and momentum of beam particles. Over the lifetime of the ProtoDUNE-SP beam campaign, which was time limited due to the CERN long shutdown, the detector was supplied a positively charged particle beam with momenta of 0.3, 0.5, 1.0, 3.0, 6.0, 70. GeV/c. A cartoon schematic of the beamline components is shown in figure 2.13.

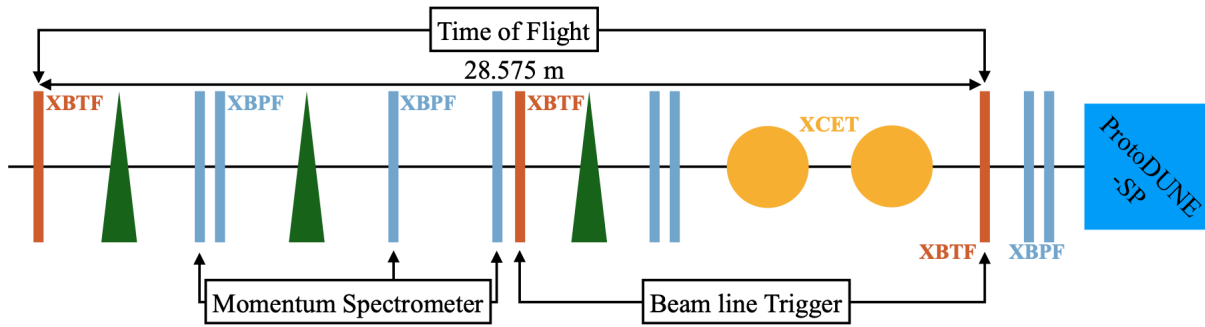


Figure 2.13: A cartoon of the beam-line supplied to ProtoDUNE-SP, showing the ordering and composition of the many components.

## 2.4.2 Photon Detection System

The photon detection system in ProtoDUNE-SP was designed prior to the baselining of the X-ARAPUCA design. As ProtoDUNE-SP was intended to be a testbed for DUNE technologies, the first run was used to test and validate multiple PDS designs, one of which was an earlier version of the ARPAUCA, labelled the S-ARAPUCA. The operating principle of this version is identical to that described in section 2.3.2, with the major difference being that instead of a secondary wavelength shifting plate placed inside the cavity, allowing for total internal reflection, there is just a WLS layer on the bottom

side of the dichroic filter. This operates under the same principles as the X-ARAPUCA, but lacks the gain in efficiency from internal reflections of the second plate. Due to the timeline and the then experimental nature of the ARAPUCA, only two were produced (out of 60 total PDS modules in ProtoDUNE-SP), so the placement of them needed to optimize knowledge gained. To do this, one was placed on the beam-side, in the first APA nearest the expected beam interaction point. This allows for as much information as possible to be collected about the behavior in high particle interaction zones. The second S-ARAPUCA was placed on the non-beam side, in a central location of the central APA. This allows for the module to collect light information from passing cosmic particles, and alleviates the majority of geometrical issues that would arise from a less symmetric position inside the detector, allowing easier characterization.

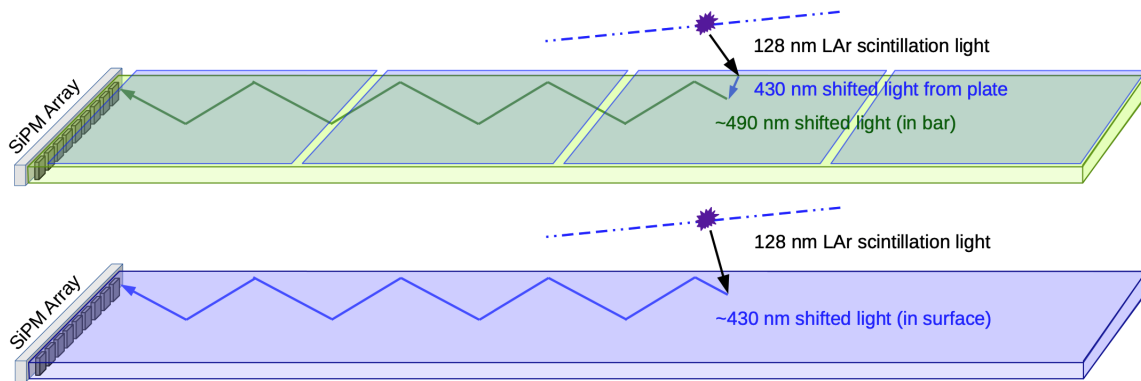


Figure 2.14: Schematics for the double shift light guide (top) and the dip-coated light guide (bottom)[47].

There are two other novel PDS designs that were implemented in ProtoDUNE-SP that follow a similar operational design. Both other technologies make sure of this bar style design that implement wavelength shifters to optimize VUV light detection. The first technology, a dip-coated light guide, was developed by a team at MIT and Fermilab. This technology is based around a clear acrylic bar as a base dipped in a wavelength shifter coating. This method uses a single WLS, TPB, and relies on internal reflection to transmit the photons to the collector end of the bar. Schematics for these designs are given in figure 2.14.

The second light guide design employed in ProtoDUNE-SP is the double shift light guide (DSLGL),

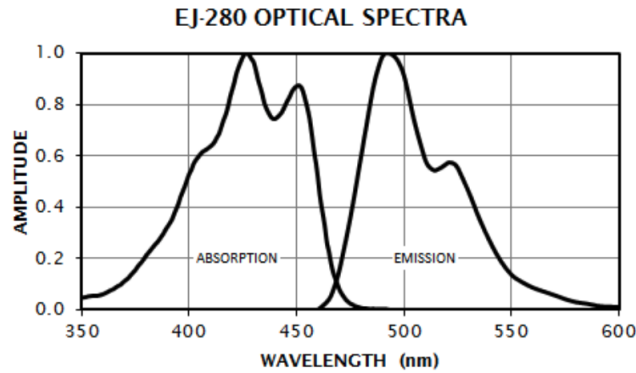


Figure 2.15: The absorption and emission spectra of the EJ-280 wavelength shifting material.

which uses two WLS in its design. The design also uses TPB as the first shifter, implemented here as a plate mounted in front of the light guide. VUV photons from the LAr volume will travel to the plate, interact with, shift, and emit from this plate into the light guide's surface. This light guide is made of a commercial WLS, Eljen EJ-280. In figure 2.15, the emission and absorption spectra for this WLS is shown. This design predates the X-ARAPUCA, and the latter operates on many of the same principles pioneered with this technology, utilizing a light guide to make sure of total internal reflection, and using two WLS to optimize the SiPM performance. Due to the production timeline and status of these two light guide technologies, they comprise the majority of PDS modules in the detector. Of the 60 modules, 58 are one of these two light guides, with 29 dip coated guides and 29 double shift. Within the APA planes, these two technologies are alternately arranged, giving both technologies full photo-coverage of the detector and allowing for accurate comparisons.

As is the theme in ProtoDUNE-SP, the choice of SiPM for the individual PDS modules allows for characterization and comparison of candidate technologies for DUNE. In this vein, there are three different SiPM models from two separate manufacturers deployed. The collaboration procured two SensL models, the A1 and C1 series SiPM, and one Hamamatsu MPPC model, the 3360-6050, for testing. A subset of Hamamatsu MPPCs are employed with a quartz window, such as those in the ARAPUCA, to better optimize collection of the incident light. To allow for uniform behavior in the presence of beam particles, all SiPMs on the beamside are SensL-A1 chips, regardless of module

technology. On the non-beam side, there is a variety of SiPMs deployed throughout. Since the S-ARAPUCA makes use of the Hamamatsu SiPM, the entire middle APA also employs them. To give some uniformity for comparison, the entirety of the downstream modules employ the SensL-C1 chips. In the upstream APA, the top half has installed Hamamatsu SiPMs and the bottom half employ the SensL-C1. The layout of the light guide and SiPM technologies is summarized in figure 2.16.

USDaS					
PD Module	HB	SSP	SSPch	DAQch	OptDet
002-0047-FL34	Hamamatsu	SSP503	0-3	216	219 41
002-0008-IU54	Hamamatsu	SSP503	4-7	220	223 43
002-0058-FL24	Hamamatsu	SSP503	8-11	224	227 45
002-0063-IU19	Hamamatsu	SSP504	0-3	228	231 47
003-0026-FL07*	SensL-C1	SSP501	0-3	192	195 49
002-0014-IU26	Hamamatsu	SSP504	4-7	232	235 51
003-0024-FL33	SensL-C1	SSP501	4-7	196	199 53
003-0004-IU48	SensL-C1	SSP501	8-11	200	203 55
002-0041-FL36	Hamamatsu	SSP504	8-11	236	239 57
002-0036-IU47	SensL-C1	SSP502	0-3	204	207 59

MSDaS					
PD Module	HB	SSP	SSPch	DAQch	OptDet
002-0002-FL22	Hamamatsu	SSP601	0-3	240	243 21
002-0054-IU22	Hamamatsu	SSP601	4-7	244	247 23
002-0059-FL08	Hamamatsu	SSP601	8-11	248	251 25
002-0020-IU09	Hamamatsu	SSP602	0-3	252	255 27
002-0060-FL39	Hamamatsu	SSP602	4-7	256	259 29
ARAPUCA-2	Hamamatsu	SSP603	0-3	264	267
		SSP603	4-7	268	271
		SSP603	8-11	272	275
002-0055-FL40	Hamamatsu	SSP602	8-11	260	263 33
002-0013-IU01	Hamamatsu	SSP604	0-3	276	279 35
002-0011-FL15	Hamamatsu	SSP604	4-7	280	283 37
002-0031-IU02	Hamamatsu	SSP604	8-11	284	287 39

DSDaS					
PD Module	HB	SSP	SSPch	DAQch	OptDet
001-0003-FL01	SensL-C1	SSP401	0-3	144	147 1
002-0044-IU50	SensL-C1	SSP401	4-7	148	151 3
002-0039-FL29	SensL-A1	SSP401	8-11	152	155 5
003-0002-IU27	SensL-C1	SSP402	0-3	156	159 7
002-0025-FL25	SensL-C1	SSP402	4-7	160	163 9
003-0011-IU37	SensL-C1	SSP402	8-11	164	167 11
003-0048-FL42	SensL-C1	SSP403	0-3	168	171 13
002-0023-IU53	SensL-C1	SSP403	4-7	172	175 15
002-0038-IU35	SensL-C1	SSP403	8-11	176	179 17
002-0040-FL06*	SensL-C1	SSP404	0-3	180	183 19

USRaS					
PD Module	HB	SSP	SSPch	DAQch	OptDet
003-0031-IU20	SensL-A1	SSP301	0-3	96	99 40
002-0055-FL03	SensL-A1	SSP301	4-7	100	103 42
002-0020-IU31	SensL-A1	SSP301	8-11	104	107 44
ARAPUCA-1	Hamamatsu	SSP304	0-3	132	135
		SSP304	4-7	136	139 46
		SSP304	8-11	140	143
002-0042-IU52	SensL-A1	SSP302	0-3	108	111 48
002-0056-FL30	SensL-A1	SSP302	4-7	112	115 50
002-0047-IU17	SensL-A1	SSP302	8-11	116	119 52
002-0054-FL38	SensL-A1	SSP303	0-3	120	123 54
001-0039-IU51	SensL-A1	SSP303	4-7	124	127 56
003-0015-FL04	SensL-C1	SSP303	8-11	128	131 58

MSRaS					
PD Module	HB	SSP	SSPch	DAQch	OptDet
002-0049-IU16	SensL-A1	SSP201	0-3	48	51 20
001-0054-FL18	SensL-A1	SSP201	4-7	52	55 22
002-0035-IU13	SensL-A1	SSP201	8-11	56	59 24
002-0006-FL14	SensL-A1	SSP202	0-3	60	63 26
001-0044-IU18	SensL-A1	SSP202	4-7	64	67 28
002-0012-FL19	SensL-A1	SSP202	8-11	68	71 30
002-0027-IU12	SensL-A1	SSP203	0-3	72	75 32
002-0015-FL21	SensL-A1	SSP203	4-7	76	79 34
001-0052-IU14	SensL-A1	SSP203	8-11	80	83 36
003-0025-FL06	SensL-A1	SSP204	0-3	84	87 38

DSRaS					
PD Module	HB	SSP	SSPch	DAQch	OptDet
403-003-0063-IU28	SensL-A1	SSP101	0-3	0	3 0
403-003-0041-FL9	SensL-A1	SSP101	4-7	4	7 2
403-002-0001-IU15	SensL-A1	SSP101	8-11	8	11 4
403-003-0054-FLP12	SensL-A1	SSP102	0-3	12	15 6
403-001-0006-IU49	SensL-A1	SSP102	4-7	16	19 8
403-003-0064-FLP13	SensL-A1	SSP102	8-11	20	23 10
403-001-0061-IU04	SensL-A1	SSP103	0-3	24	27 12
403-001-0042-FLP4	SensL-A1	SSP103	4-7	28	31 14
403-001-0025-IU21	SensL-A1	SSP103	8-11	32	35 16
403-003-0020-FL5	SensL-A1	SSP104	0-3	36	39 18

Figure 2.16: A table showing the ordering and general layout of the various PDS modules employed in ProtoDUNE-SP, giving information on the design style and employed SiPM for all modules.

## 2.4.3 Triggering and Readout Systems

All data read out by ProtoDUNE-SP was the result of an event trigger. These triggers come from one or more of the sub-systems and are handled by the central trigger board (CTB). The CTB is a hardware solution for event triggering, communicating with the sub-systems to search for coincidences and signaling the timing system to make a readout decision. The timing system itself is a 50MHz clock, and the readout decisions can be configured at run time. Once an event is signaled for readout, data is streamed continuously for 6000 samples at 3MHz, beginning with a buffer of  $250\mu s$  before the trigger. The PDS is also readout here using the same schema, where the internal clocks

of the PDS operate at 150MHz, so more samples are taken with a result of the same  $13.3\mu\text{s}$  of data available.

ProtoDUNE-SP took data from two different triggers, the particle beamline trigger and the cosmic ray tagger (CRT). The particle beamline is triggered from by a pair of scintillating fiber monitors, which also track the position and momentum of the incoming particles. The CERN beamline is highly monitored and finely timed, so the ProtoDUNE-SP beamline knows when to expect a beam dump. The beamline trigger is activated by two interactions in the downstream monitors that is coincident with this beam window. The CTB stores and readout a trigger word associated with this event, allowing those in data analysis to search for a beamline triggered event in the data file.

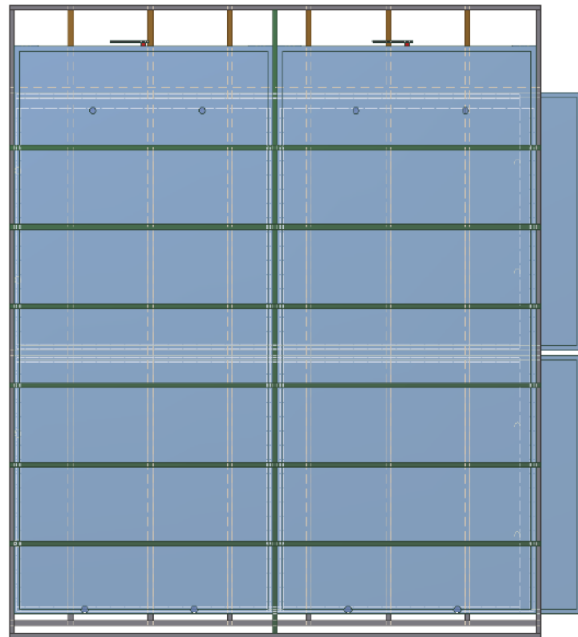


*Figure 2.17: A schematic of the CRT modules used in the ProtoDUNE-SP experiment.*

The CRT is comprised of four modules of scintillating straw tube trackers, originally designed for the Double-Chooz experiment and repurposed for the ProtoDUNE-SP experiment. The operating principles of straw tube trackers is well understood, and these modules have been characterized as seen in [48]. The CRT sub-modules are comprised of 64 scintillator strips that measure  $5\text{cm} \times 1\text{cm} \times 320\text{cm}$  in width, thickness, and length respectively. The strips are overlaid in two parallel layers,

offset by 2.5 cm allowing for a 2.5cm effective pitch. The scintillator strips each contain a WLS fiber which is readout by a Hamamatsu M64 PMT which is outfitted with a custom electronics readout board to signal triggering and record the pulse height on the individual fiber channels. These board are self triggered and triggers are sent to the CTB for decision making. Each ProtoDUNE-SP CRT module is made of four sub-modules, two vertical and two horizontally oriented, shown in figure 2.17. These four overlapping sections, called panels, give two dimensional spatial resolution for the incident muon track. A trigger is formed on a panel-to-panel coincidence basis. Though, originally, this lead to an effective pitch of order 1m for CRT track incident locations, work was done to decode the readout from the CRT electronics to reduce this to a coincidence strip-level tracking resolution.

The CRT trigger coincidence time can be configured on the software side of the controls. The electronics must be fed a configuration file that states what the expected coincidence time is, as well as what sub-sets of panels to trigger on. This process can allow you to effectively mask off parts of the detector and only readout illumination in a desired section of the TPC. Due to the positioning of the beamplug, as well as the other materials and the ProtoDUNE-DP cryostat within the EHN1 hall, the upstream CRT trackers were installed with an offset in the beam direction, meaning that the beam-left CRT module was closer to the cryostat face than the beam-right module. With a fixed coincidence timing of 80ns for the majority of the data-taking period, this inherently biased the CRT triggered data to beam-left side. This layout can be seen in figure 2.18.

The ProtoDUNE-SP TPC was readout by two competing technologies, the ATCA-based RCE [49], and the PCIe-based FELIX [50]. Both of the technologies were used together throughout the beam and cosmic runs. The TPC reads out one wire per channel, looking for a peak in the charge distribution. of the induction wires This hit is timed to see if it coincides with hits in other channels or a timed trigger signal. The raw wire hits are readout to be reconstructed by the software at a later time. ProtoDUNE-SP utilized the Pandora pattern reconstruction package for its tracking, following other LArTPCs. This software package uses algorithms and machine learning software to cluster these raw wire hits within their plane, and then matches these 2D cluster into 3D hits and tracks.

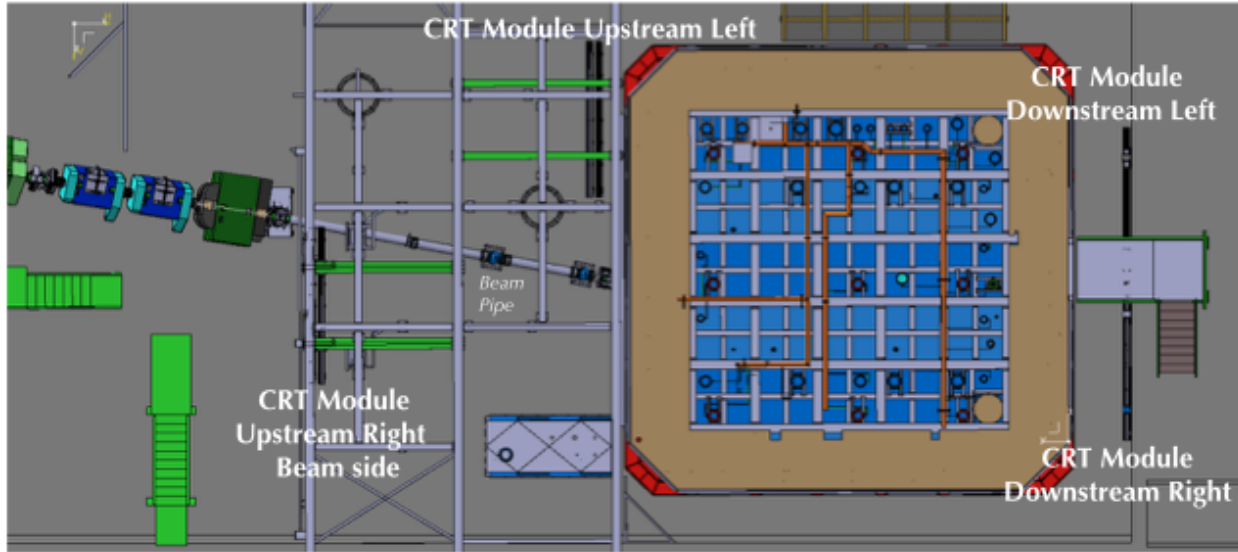


Figure 2.18: The layout of the NP-02 cryostat, beam-line, and CRT modules in the CERNM neutrino hall.

## 2.5 Xenon Doping of ProtoDUNE-SP

After the beam and cosmic data taking runs of PDSP, there was an R&D campaign. Part of this campaign was used for voltage tests and neutron source tests. There was also an extended campaign of xenon doping studies. Over five months, 13.3 kg of xenon was injected into the ProtoDUNE-SP detector. Xenon has been used as a detector medium in TPCs for many years[51], typically for experiments that require exceptionally low noise, such as dark-matter searches or  $0\nu\beta\beta$  searches[52]. Xenon tends to have better optical properties than argon in TPCs, xenon produces more scintillation photons at a higher wavelength, making them easier to detect using modern SiPMS or PMTs. The  $128\text{nm}$  wavelength of argon scintillation photons necessitate the implementation of WLS, as described in 2.3.2, which reduces the overall detection efficiency. Xenon scintillates light at  $175\text{nm}$ , which is a wavelength that can be detected with relatively high efficiency in modern SiPMs. Xenon also has a significantly longer Rayleigh scattering length, expected to be nearly eight times that of LAr. This means that light is detected more uniformly over large drift volumes, such as those implemented in PDSP and DUNE. Increased light uniformity makes triggering far from the PDS (i.e. near the cathode) easier. Xenon also has the possibility to improve calorimetric capabilities and could improve resolution of low-energy events. Xenon also features two scintillation components,

currently measured to be about 4 and 26ns[53], but both are significantly faster than the argon components. Xenon also has some potential to help the LAr PDS recover performance in the presence of dopants, such as nitrogen. This will be discussed further in this section and chapter 4. Figure 2.19 shows the same process as ?? but in the presence of nitrogen and xenon. If large amounts of nitro-

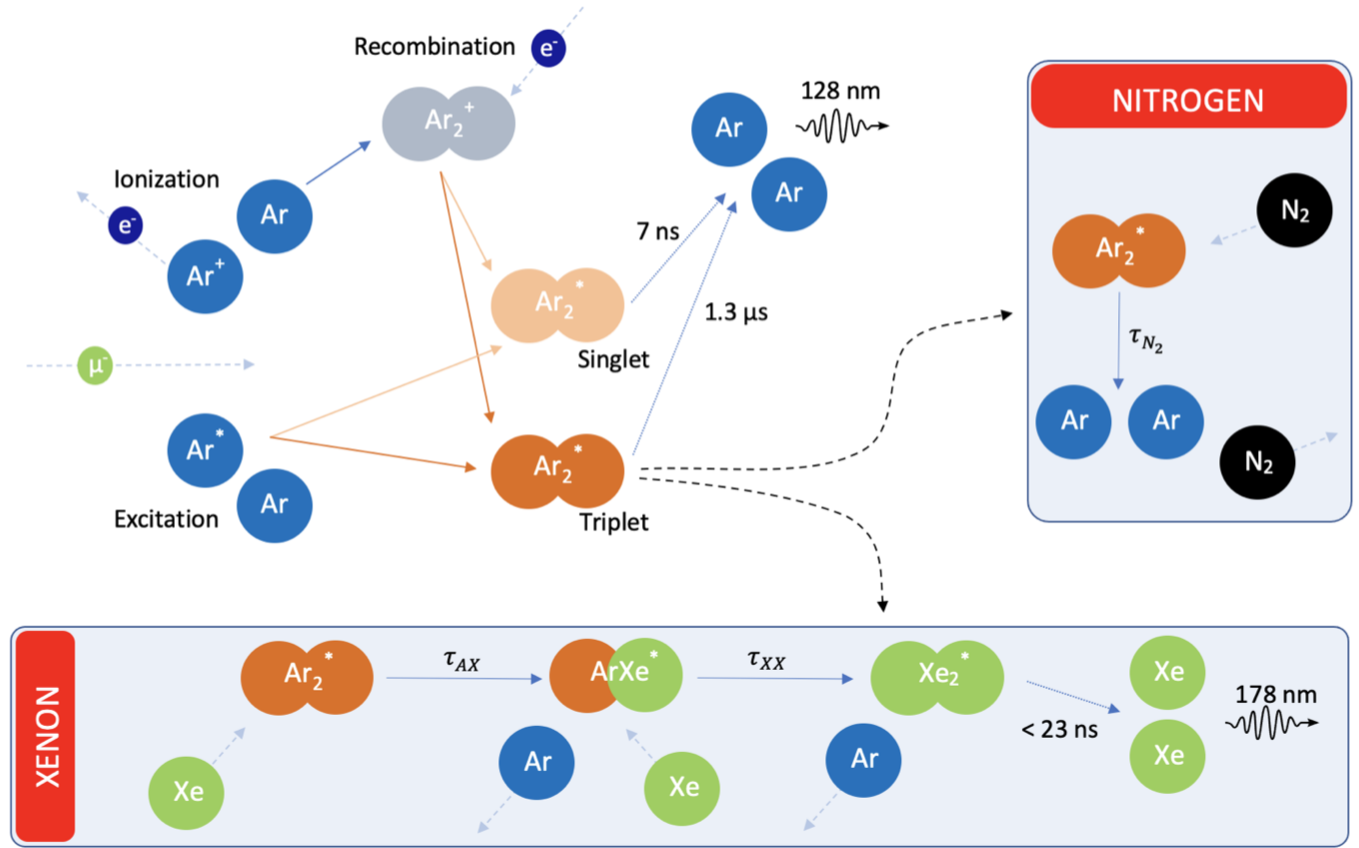


Figure 2.19: The processes which create scintillation light in the three detector conditions characterized in this work.[54]

gen are present in the detector, then a nitrogen atom will interact with the argon dimer, colliding and removing the excitation energy. This process,  $Ar_2^* + N_2 \rightarrow 2Ar + N_2$ , is a well understood quenching process[55], since the dimer no longer decays and emits a photon. In the presence of Xenon, the argon dimer collides with a xenon atom, creating a new hybrid  $ArXe^*$  dimer. This dimer exists until it collides with another xenon atom, resulting in an excited xenon dimer,  $Xe_2^*$ . As with the argon excimer, the xenon excimer decays after some lifetime and emits a de-excitation photons of wavelength 175nm. The interaction time for an argon excimer with xenon tends to be quicker



Date	Xenon (grams)	Xenon (ppm)
13-14 Feb. 2020	776	.1
26-28 Feb. 2020	2234	3.1
3-8 Apr. 2020	5335	7.4
15-20 May 2020	1984	2.8

*Table 2.1: The dates and amounts of the various xenon injections during the campaign. Between injections, a variety of cosmic data was collected for analysis.*

than that of nitrogen. When both are present in the mixture, these two processes compete with each other, with the nitrogen quenching removing scintillation light and the xenon process shifting the scintillation wavelength, with a quicker decay time than the argon excimer.

Typically, the xenon interaction process can still occur in the presence of nitrogen, due to significantly quicker decay times. This allows the injection of xenon to counteract the effects of quenching due to dopants in the bulk volume. Because of this, xenon injection could be a mechanism with which to recover operational performance given some sort of failure in the detector that introduces contaminants into an operating TPC. ProtoDUNE-SP ended up being a perfect testbed for this as, just as the xenon doping campaign began, a failure in the recirculation system introduced a large volume of oxygen and nitrogen into the detector. The recovery of the system filtered out some of the contaminants, but the result was that approximately 5.7ppm of nitrogen remained in the bulk. Subsequent injections of xenon were introduced slowly over five months. The xenon was injected in gaseous form in the boil-off recirculation line, allowing the xenon and argon to be fully mixed before the gas was re-condensed and injected back into the bulk. Over these five months, five separate injections were done with data taken between injections. Table 2.1 shows the date and amount of xenon introduced into the detector.

During the majority of the xenon doping campaign, the field was not applied to the cryostat. This makes simultaneous analysis with TPC components impossible, and thus analysis of the effects of xenon was done using just the CRT and PDS data. Data was collected from cosmic events for every run during this period, using the PDSP-PDS. The waveforms were analyzed over this period to see

if the waveform time profile was shifting from the argon to xenon time structure. Figure 2.20 shows the evolution of the average waveform for the ARAPUCA, DSLGs with SensL SiPMs, and DSLGs with Hamamatsu SiPM in the beam left drift volume from runs with pure LAr, after the nitrogen contamination, and after all 18ppm of xenon. The shift in scintillation time structure is clear.

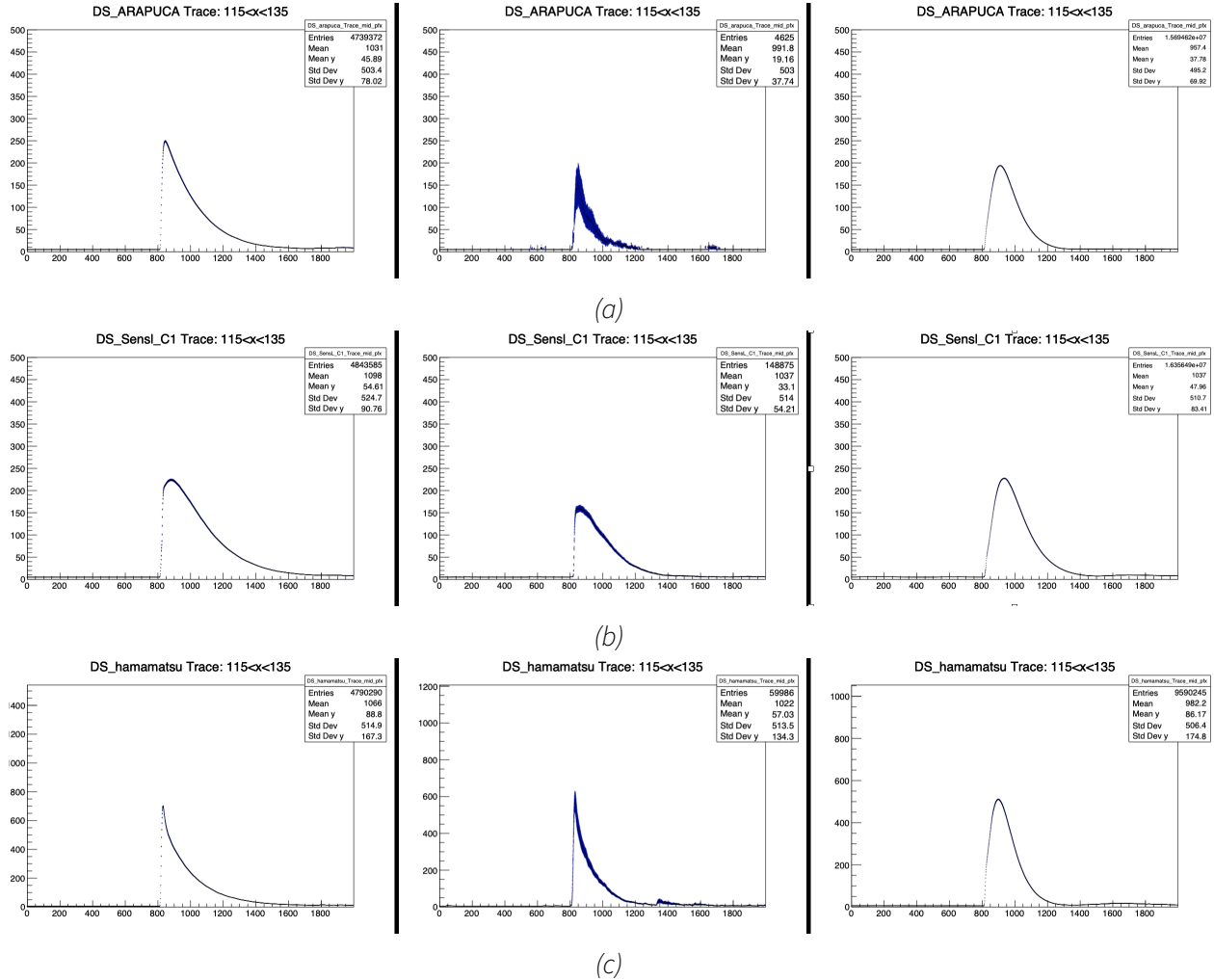
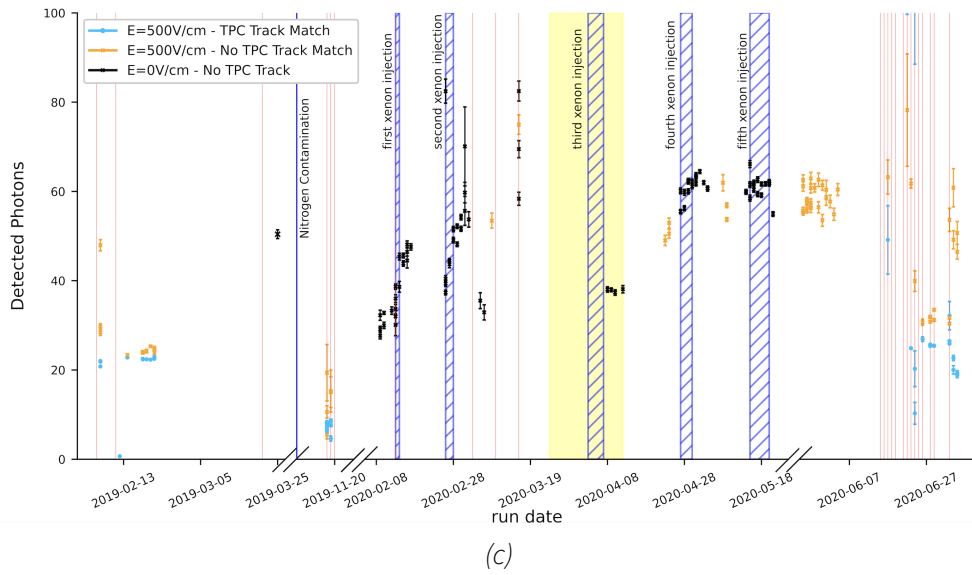
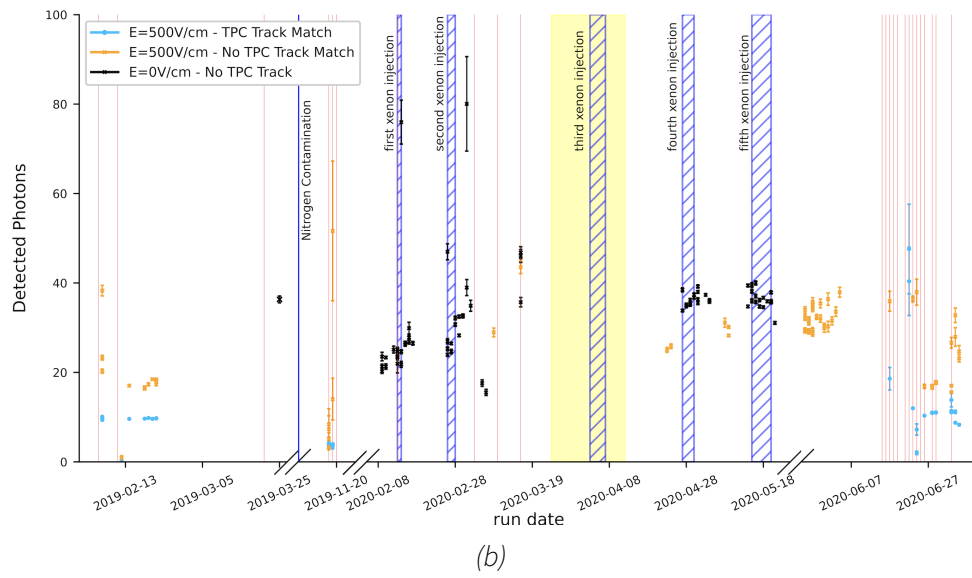
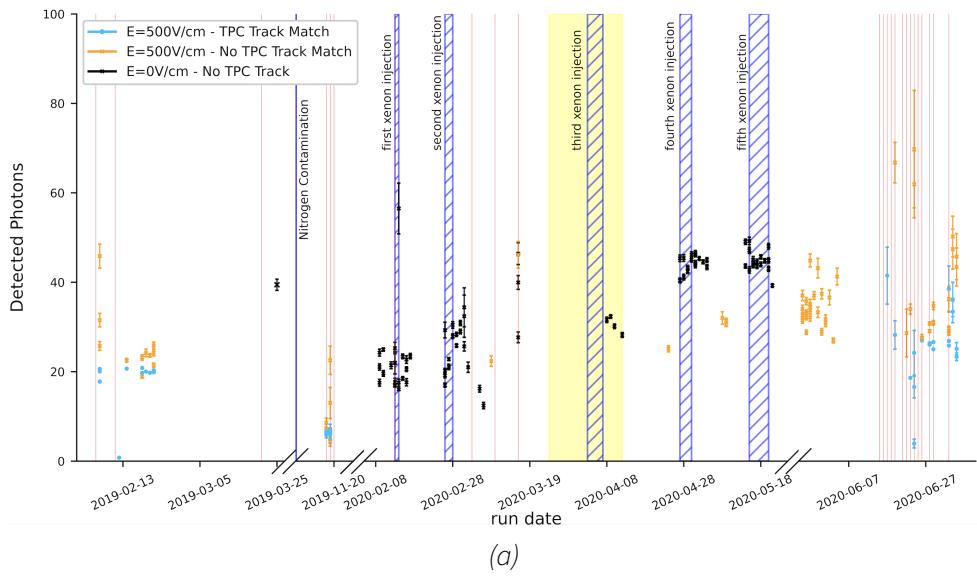


Figure 2.20: Evolution of the average waveform from Pure LAr, Nitrogen contaminated LAr, and the subsequent Xenon doped mixture. The evolution shows the transition from the argon scintillation structure, to heavily quenched light yields (LYs), to recover light yields with the xenon time structure. Results for the ARAPUCA (a), DSLGs with SensL SiPMs (b) and Hamamatsu SiPMs (c) are shown for the BL APA.

To better see how the xenon doped light yield compares to the pure LAr yield, as well as how well the recovery from contaminants was, an analysis was done to find the average light yield for all cosmic runs over the PDSP lifetime. To allow for a good comparison of both the data with the field and with-

out, and to quantify the absolute light yield, two different matching algorithms were implemented. The first, a CRT-TPC-PDS matching algorithm will be explained in full detail in the following chapter. The second was is a CRT-PDS matching scheme which time matches a CRT hit with a PDS readout trigger. The CRT-PDS only matching allows runs with no drift field to collect "tracks" and analyze the light yield from these. Here, the CRT and PDS signals are matched in time, with a "track" formed by a straight line between the two CRT pixels. The analogous matching with the TPC is time matching the CRT and PDS, and then spatially matching a TPC track with the CRT track, increasing purity.

After events have been selected by one of these matching schema, the number of photons on each module is collected. We select on a subset of the detector, to remove LY variations due to track distance from the PDS. For this analysis, a range of 150-250 cm from the PDS module was selected. This range gives good uniformity while also allowing for a large number of statistics to be analyzed. All events from a single runs were averaged. Once an average and standard error were calculated, event that deviated more than  $5\sigma$  were removed. This process allows a better tracking of the true average light yield, without a sample be skewed by a large cosmic or other bright event. This procedure produces a LY over time plot for the entire PDSP lifetime. To account for some deviations, a red line representing changes to the CRT mask is plotted, since this configuration changed many times over the lifetime of the detector and contributes largely to the statistics and average radial distance of the tracks. Labelled vertical lines denoting changes to the bulk are also plotted, so that one can see how various contaminants/dopants affect the light yield. Finally, a large yellow region has been indicated where only a single APA was collecting light data, which removes data for some detectors and changes the number of modules included in others. Figure 2.21 has these LY versus time plots for the all PDS modules in ProtoDUNE-SP. One can clearly see the drop in LY from the nitrogen contamination, as well as the subsequent recovery from the various xenon injections. Also clear is the field dependent LY, which was discussed in 2.2.1. In the next chapter, the Rayleigh scattering and absorption lengths of the bulk medium in the three states will be discussed.



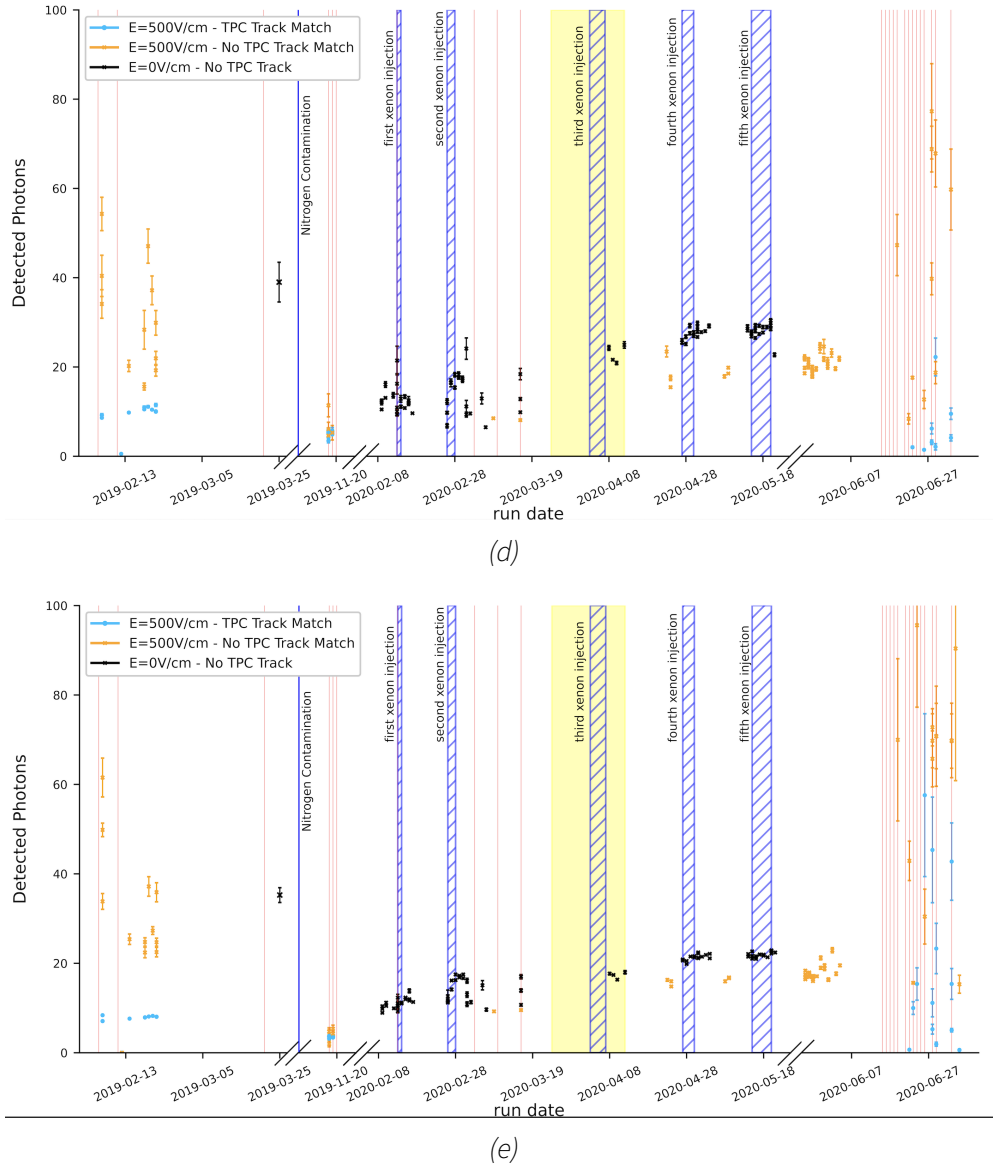


Figure 2.21: Evolution of the light yield over the lifetime of ProtoDUNE-SP for the various grouping of DSLGs and ARAPUCA in the detector. These plots are separated by detector technology and read-out SiPM, with the ARAPUCA on the BL side in (a), the DSLGs with SensL C-series (b), A-Series(e), and Hamamtsu (c) chips. The beam-side ARAPUCA in in figure (d).

## Chapter 3

# Photon Detector Characterization and Development

In this chapter, I will discuss the research, development, and characterization of components of the DUNE photon detector modules. The first section will discuss the simulation and characterization of the ARAPUCA and light guide modules, where various characteristics will be analyzed in an attempt to optimize the light detection of this technology. These simulations were done using GEANT4 simulation suite and were completed in conjunction with the baselining for the DUNE X-ARAPUCA design. The second section will discuss the construction of a laboratory setup to test the resiliency of the dichroic filter coating that is intended to be employed on the ARAPUCAs for DUNE-HD. This is the first resiliency study of this technology, which is important given the long operational lifetime of the DUNE physics program.

### 3.1 PDS Simulation and Characterization

GEANT4<sup>1</sup> has long been the standard simulation software for high-energy physics experiments. The software was designed specifically with the intent to simulate the passage of particles through matter, making it an ideal medium for particle detector simulations. After building a model of the de-

---

<sup>1</sup><https://geant4.web.cern.ch>

tector, one can simulate a variety of particles passing through, reading out the effects as necessary and characterizing your design.

For the DUNE-HD PDS design phase, GEANT4 simulations were used to analyze the passage of photons through the material and to the detector. By building a catalog of the physical properties of the composite materials, and building out a scale model in the simulation, one can effectively prototype the detector prior to building many physical prototypes. This allows for a more robust understanding of the design and for a quicker search of various geometries to optimize the design.

After this initial design and test phase, an optimization phase was undertaken. The overall design of the ARAPUCA was finalized[56], but the dimensions and interfaces were not set, due to some uncertainties. This necessitated modeling and optimization within this framework, giving the designers and the DUNE collaboration a more complete picture and allowing for the most photon collection efficiency. All studies presented here used an additional software package called GATE<sup>2</sup>, a simulation software built on top of GEANT4 designed for the numerical simulation of medical imaging devices. The software supports single photon emission tomography, optical imaging and radiotherapy experiments. On top of this wide range of applications, GATE slightly simplifies the process of building out a device simulation by implementing a macro based architecture. This leads to a more intuitive and simplified interface while having a wide range of physics processes available that are suitable for the simulation of a VUV photon detector.

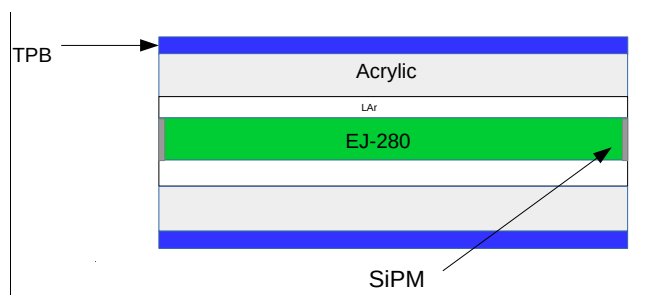


Figure 3.1: Cartoon of the various layers and interfaces in a double shift light guide.

To begin this analysis, a recreation of the DSLG geometry was created and tested. This allowed for

<sup>2</sup><http://www.opengatecollaboration.org>

the validation of GATE as a software suite applicable for this work, with the availability to compare to the results seen in [57]. This was done by using the dimensions and material lists found in [45]. Not all of the materials used in the PDS modules are common, and because of this the properties of various materials had to be source from the manufacturer. One example of this is the wavelength shifting coating used for the second wavelength shifter in the DSLG, a commercial WLS called EJ-280, produced by Eljin. Once this list was compiled, a geometry file was created listing the positions, sizes, and material composition of the components such that a mockup of the detector was created in the simulation. A cartoon for the general schematic is shown in figure 3.1. GATE allows for a single photon source to be used, and shifted throughout the the simulated space. This allowed for a  $128nm$  photon source to illuminate the surface of the simulated collector at many points in a grid. Once this process was completed, the number of photons collected at along the central axis was plotted against the distance from the SiPMs. The results for this analysis compared to the work cited is shown in figure 3.2, showing good agreement.

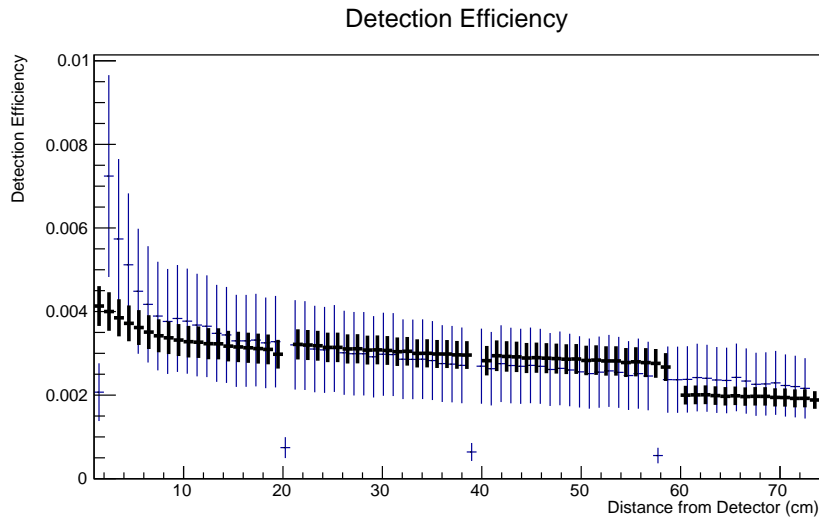


Figure 3.2: A comparison of the attenuation of a double shift light guide installed in the TallBo (black) cryostat and the simulations of the same light guide in GATE (blue).

As with the wavelength shifter used in the bulk of the double-shift light guide, EJ-280, TPB, the wavelength shifter used in the first layer, is also relatively novel for GATE. This also necessitated finding and entering the physical properties of this material into the local GATE database. To do this, the



bulk material of acrylic was used and the wavelength shifting and attenuation characteristics were entered based on the available literature. To validate this, we calculate how the ratio of photons incident on the TPB surface to the number of photons that reach the SiPM changes as the thickness of the coating changes. This is a relatively difficult analysis to do in this formulation, as the nature of GATE necessitates that we model the TPB as a TPB infused piece of acrylic (or other inert material). This should not change the behavior of the material at all, since all of the photon effects are implemented in the model, but does introduce extra interfaces. Every individual interface needs to be characterized and defined within the architecture of the simulations, and any mis-modeling that results in a gap or overlap drastically effects the results. This necessitated the iterative design not only of the physical model itself, but of the different material interfaces. Once a well designed model was developed and simulated, the photon ratio in the simulation was compared to that measure in [58], figure 3.3, showing good agreement between the measured data and this simulation.

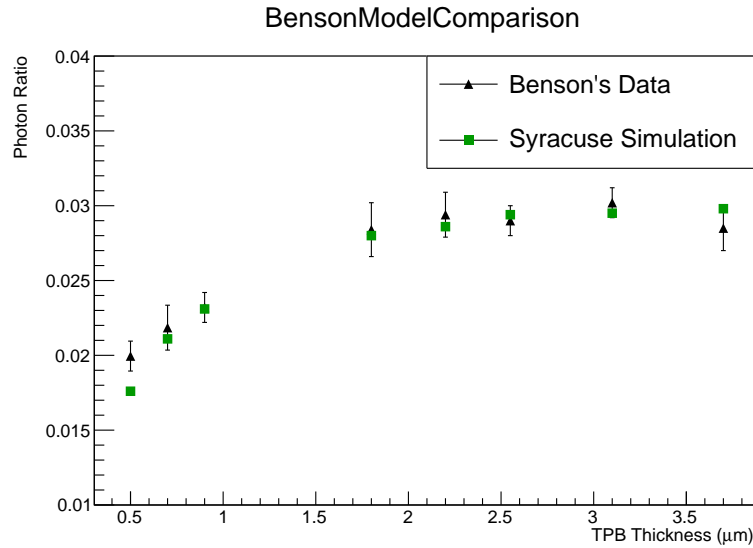


Figure 3.3: A comparison of the photon ratio as a function of TPB thickness for this simulation and the data from Benson et al. [58]

After successful validation all of the necessary materials in the double-shift light guides and of the GATE software, we move towards modeling the performance of these modules. This will serve as a baseline for the future models of the ARAPUCA and X-ARAPUCA designs. To better compare the performance of all of the detector designs, we need to define some comparison metrics and set some

standards. The first thing to note is that the same SiPM will be simulated for all designs, despite a different chip being used in the ARAPUCAs in ProtoDUNE. A single SiPM was used so that any changes in collection efficiency that arise can be correctly attributed to changes in the geometry, and not be a side effect implementing different SiPMs. The SensL C-series SiPM served as the baseline readout chip for the rest of this chapter. This chip has a well defined detection PDE, figure 3.4 and was used in the TallBo experiment[58] as well ProtoDUNE-SP. The first metric to be used as comparison is the effective area of the detector,  $A_{eff}$ , taken to be the product of the total area of the detector and the total detection efficiency. Throughout this work, we will quote  $A_{eff}$  for a full length DUNE-HD module, which is twice that simulated. This is to be consistent with number quoted in other studies of this system and allow for internal comparison of designs. We can then compare the total area per SiPM implemented in the design, which can be more enlightening than the total effective area. Some designs use significantly more chips which can be impractical from a cost perspective, while also not proving to be enlightening because the relationship between increased sensor count and increased efficiency is relatively trivial.

The effective area of a single TPB coated SiPM is calculated, since this is a standard comparison for all simulations. This value of effective area for the SiPM,  $A_{eff,SiPM}$  allows us to take into consideration the WLS efficiency, photon detection efficiency of the chip, as well as geometrical effects in a single number. The efficiency for this system is found to be .127. The area of a single SiPM is  $6 \times 6mm$ , giving us a result of  $A_{eff,SiPM} = .046cm^2$ . This value allows us to calculate an optical gain ( $g$ ) as a comparison metric, where  $g = A_{eff}/A_{eff,SiPM}$ . With this collection of comparison metrics, we can effectively compare the overall efficiency of a design, the effectiveness of its SiPM layout and use, and the effective gain of the design over a set of bare sensors in its place.

To begin this analysis, we compare two layouts of DSLG SiPM placement. This gives us a place to validate our simulation scheme, the grid like application of a VUV light source over the module face, and some insight into the geometrical effects of SiPM placement in these detectors. The first two designs include placing the SiPMs on either the long or short end of these detectors. A rendering

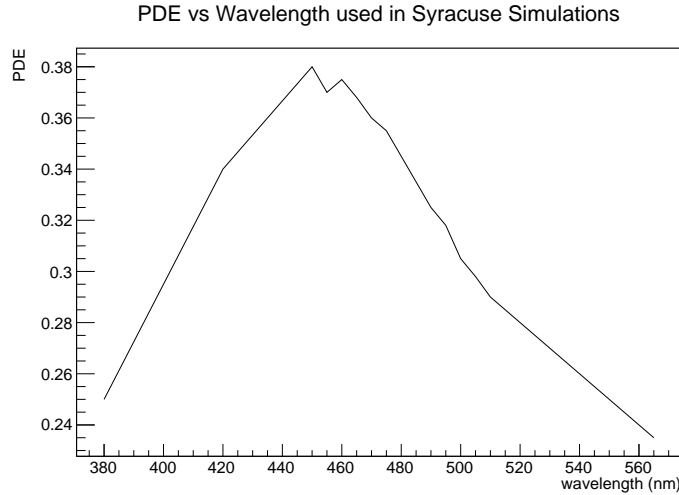


Figure 3.4: PDE for the SensL C-Series SiPM as a function of incident wavelength.

of these different design scenarios with a light source from the simulation is shown in figure 3.5. One can see the large difference in SiPM count between the two, with the long-side having 96 chips and the short side design having 24. This amount of SiPMs in these two arrangements will also be a constant throughout the rest of this section. The initial results from the simulations can be seen in 3.6. Each bin on this histogram represents the detection efficiency from a photon source applied at that point, giving us a clear view of the geometrical effects and efficiencies of the design.

The total effective area for the end and side scheme in this design were  $14.7\text{cm}^2$  and  $14\text{cm}^2$  respectively. Despite having nearly 1/4 the number of SiPMs, the design with SiPMs located on the end has a higher effective area (and thus higher gain). Rerunning the above simulations with only individual chips active in either scheme we can see that the increased visibility of the SiPM is the cause for this. In the designs where the SiPMs face down the entire detector, they collect a non-negligible number of photons from nearly every point in the module. In designs where the visibility of the SiPM is limited, so is the detection efficiency. One can also observe that the chips have a cone of maximal detection directly in front of them. This is a geometrical effect where photons coming in at too sharp of an angle are either not detected or are more likely to terminate on the side of the chip rather than the face. The total effective area of the designed implementing end mounted SiPMs is nearly 5× that of the side mounted counterpart.

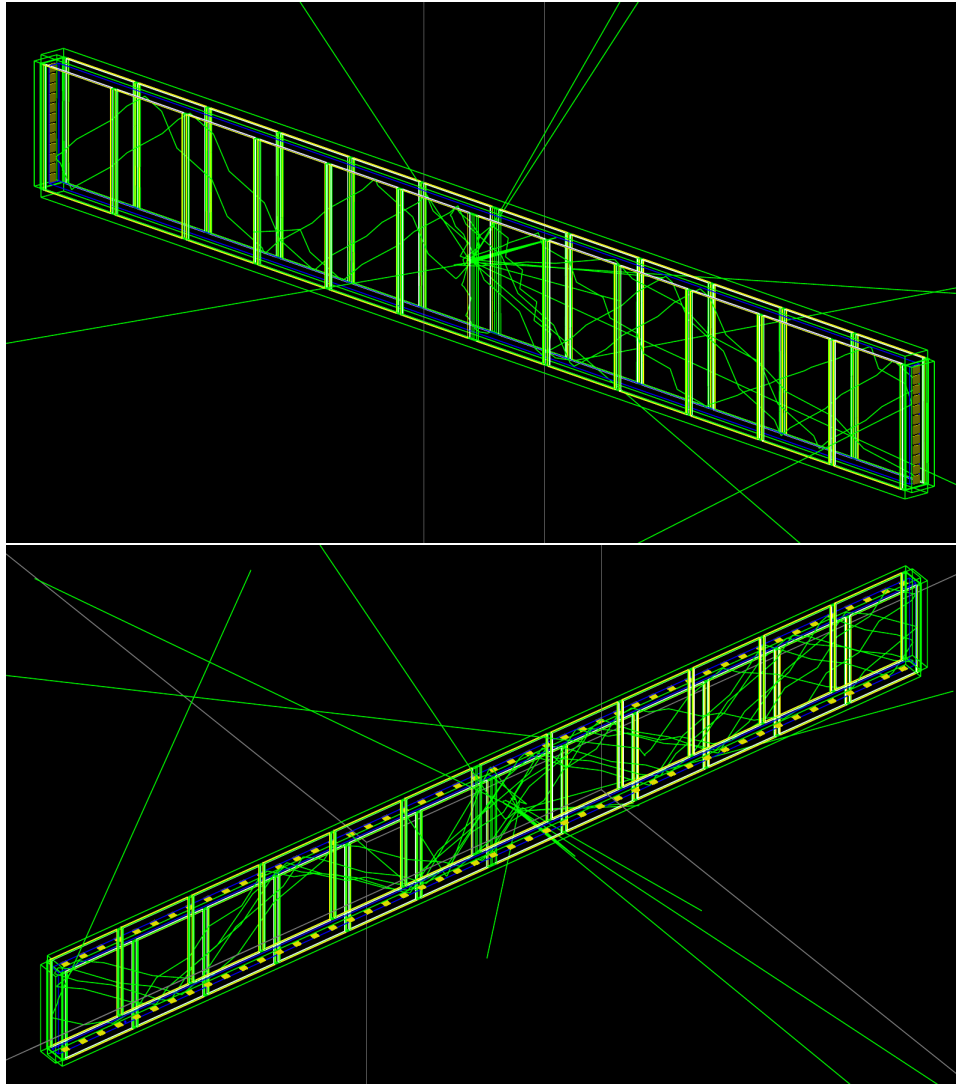


Figure 3.5: The renders of the two double-shift light guide SiPM layout designs, with the 24 chips on the shorts ends and the 96 chips on the long ends.

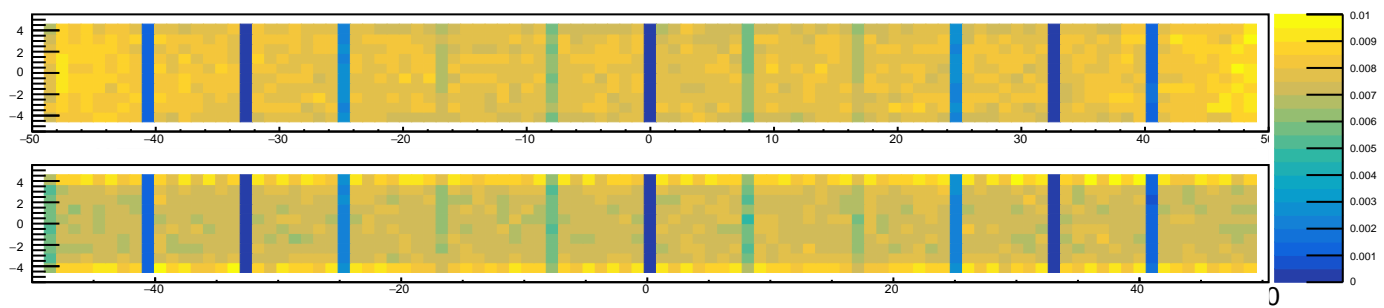
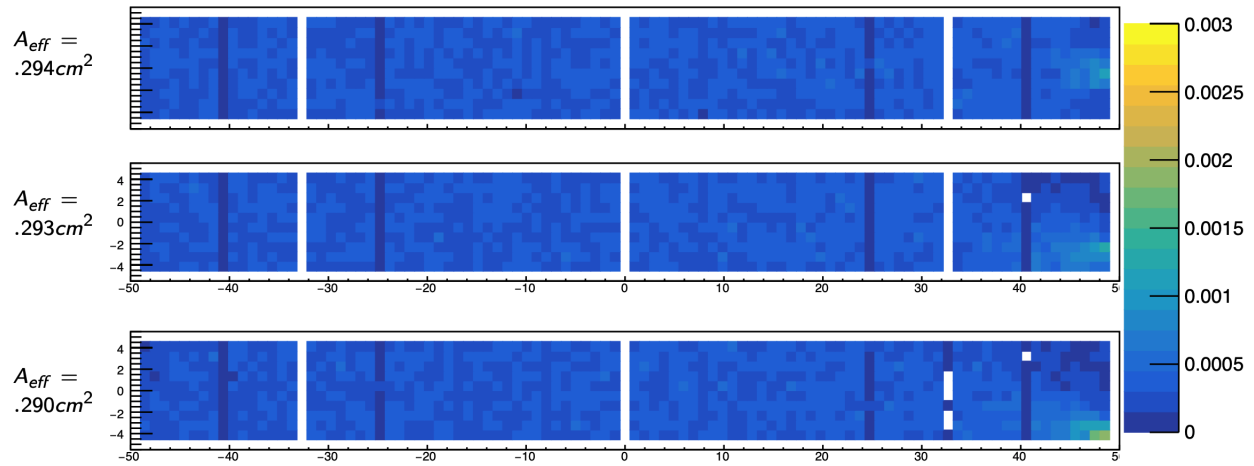
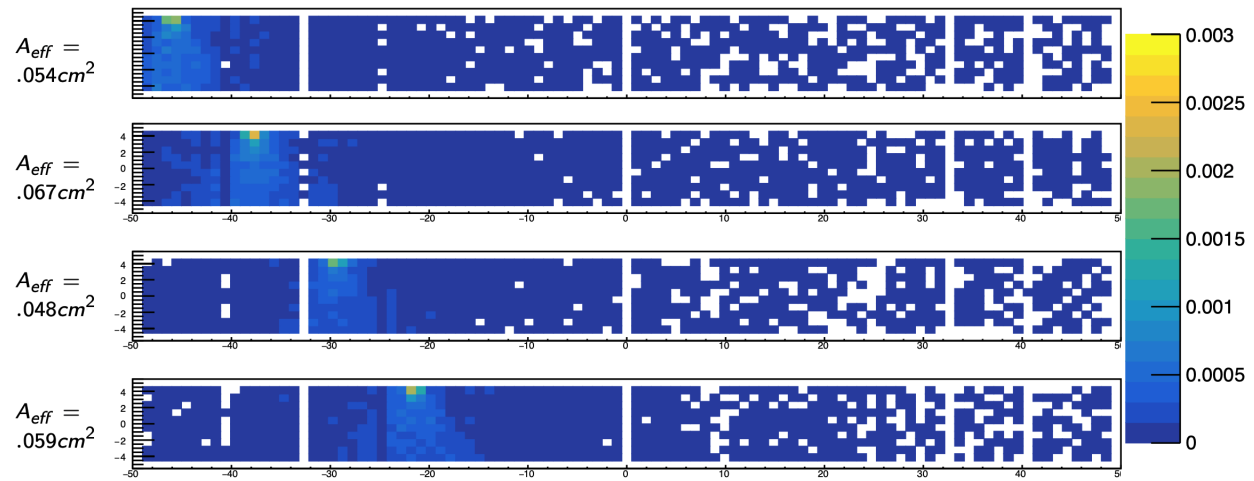


Figure 3.6: The position dependent efficiency for the end-scheme (top) and side-scheme (bottom) double-shift light guide designs.



(a)



(b)

Figure 3.7: (a) The position dependent PDE for various SiPMs mounted on the end of a DSLG, with the effective area for the single chip shown to the left. (b) The same as (a) but for various side mounted SiPMs.

Expanding this work to include the ARAPUCA, a few choices were made to simplify the transition and make the comparisons to the double-shift light guides easier. First, we choose to simulate the same SiPM, as stated previously. We also choose to test two different compositions of ARAPUCA. The first is the baseline design, a cartoon of which is shown in 3.8a, with a second taking the wavelength shifters of the DSLG, utilizing TPB on the exterior and a green WLS on the interior, a cartoon drawing of this is in 3.8b. For this, we note two things about the materials. For the baseline design, p-Terphenyl is used as the first WLS, but this material is not well characterized in the VUV region. To overcome this, we simulate the response identically to TPB. This is a strong compromise, but literature has shown that pTP can be trusted to behave in a similar way. For the ARAPUCA with the green WLS, we simulate a fake material similar to EJ-280, with some physical properties shifted to better emulate a thin crystal deposition layer. Finally, dichroic filters are a novel feature in GATE. This behavior had to be validated within the software itself. Once this is done, we take the dichroic filter data we received from the ARAPUCA manufacturer and shift it into the region between the TPB and the green WLS for the second ARAPUCA.

To validate the implementation of the dichroic filter, we simulate a double-shift light guide with this feature, as seen in 3.9. The same simulation procedure described above was used to track how the performance was impacted by the increased light trapping. A comparison of the design scheme with the SiPMs on the end with and without the filter is given in figure 3.10. The same comparison was made for the side mounted design as well, with both outperforming the baseline design by nearly  $2\times$ . The effective areas for the end and side mounted designs with the filter are  $22.11\text{cm}^2$  and  $25.23\text{cm}^2$  respectively. Worth noting is that, similar to figure 3.7a, a cone of maximal absorption is seen if single chips are simulated. The inclusion of a dichroic filter increases the effective area seen by a single chip by more than  $2\times$ , and in the case the side mounted SiPM design this number is greater than 3, allowing these geometrically limited detectors to see light from the entire light guide. This behavior seems to validate the design of the dichroic filter in the simulation, successfully trapping the light in the guide, as well as its inclusion into the ARAPUCA design. From here, we can confidently simulate and characterize the ARAPUCA designs.

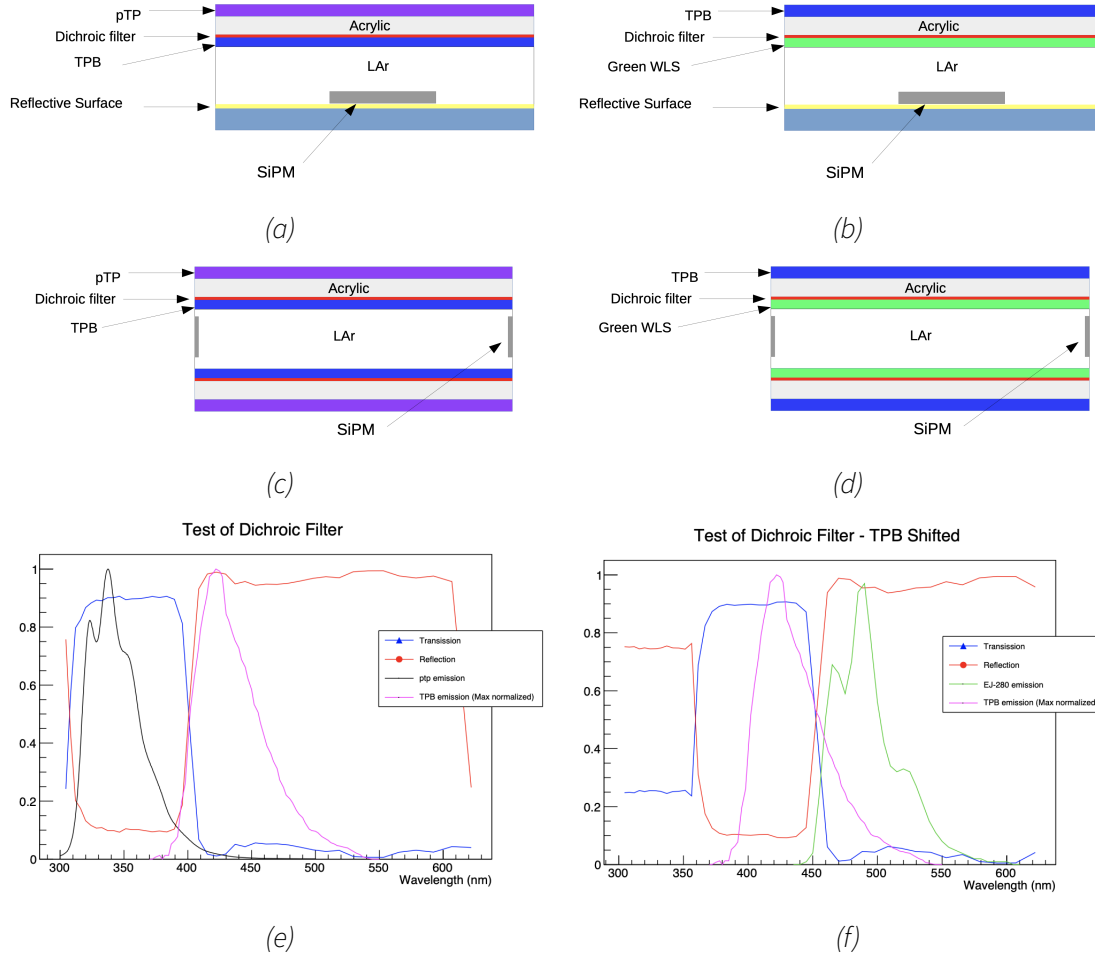


Figure 3.8: Cartoons of the design of the two different types of ARAPUCAs, one for being mounted on the inner APAs in DUNE-HD and one for being mounted on the exterior. The second row are these designs with the green WLS implemented, to mimic the shifter design of the double-shift light guide.

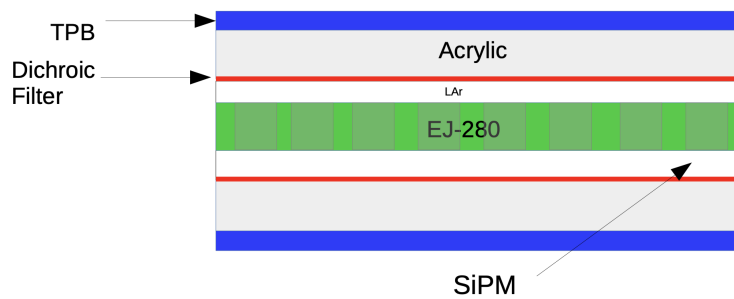


Figure 3.9: A cartoon drawing of the double-shift light guide with the dichroic filter implemented.

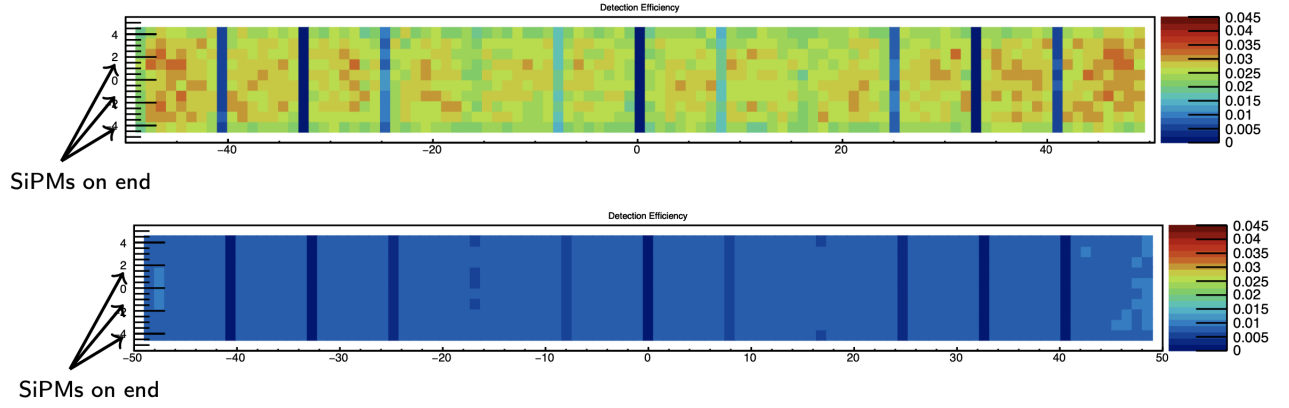
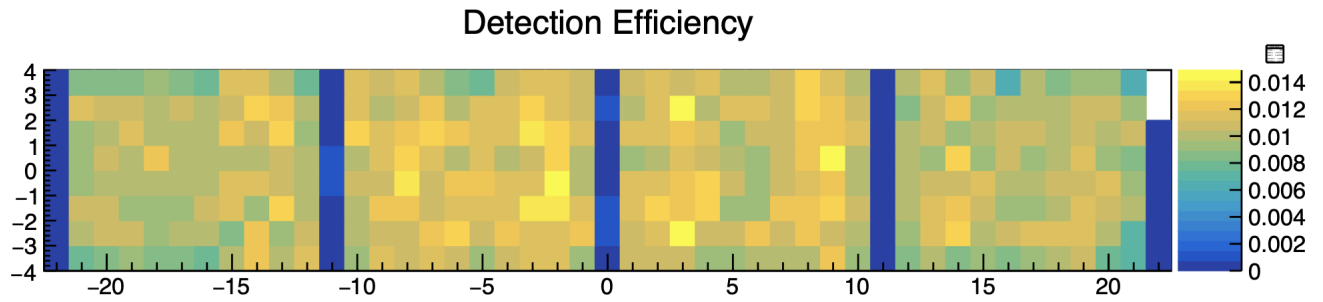


Figure 3.10: A comparison of the photon detection ratio for the double shift light guide with the dichroic filter (top) and without (bottom).

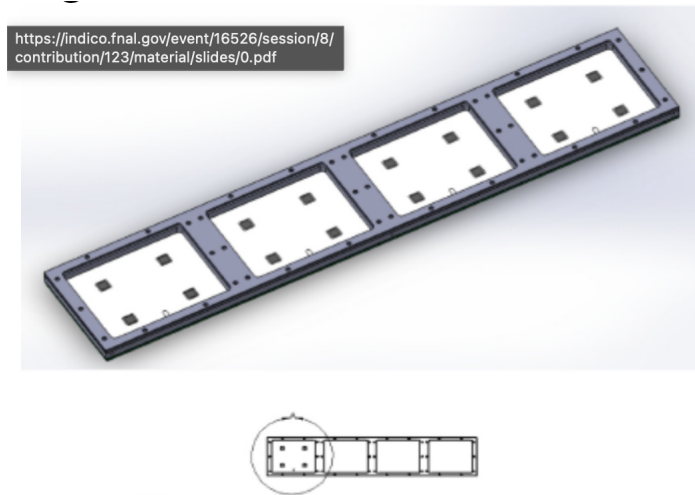
After validating the dichroic filter implementation and design, we build out the ARAPUCA model. We use the designs for the ARAPUCA installed in TallBo, which was an experiment that was operated at FermiLab. The purpose of the TallBo experiment was to characterize the bar-type detectors that were planned and designed for DUNE. A XXL cryostat was filled with liquid argon and prototypes for the three PDS module technologies were inserted and exposed to cosmic rays. The performance of the various designs was then documented for consideration and design iterations before ProtoDUNE-SP [58][59]. From this, an absolute efficiency of the ARAPUCA design was calculated. The technical drawing for the design and the results from the initial simulation are shown in figure 3.11. The result for this module in the simulation is a gain of  $g = 4.67$  and  $A_{eff} = 3.44 \text{ cm}^2$ . In TallBo, the total area of the ARAPUCA designed is  $9.8 \times 7.8 \times 4 = 305.76 \text{ cm}^2$ . The measured efficiency was .0077[59], resulting in a total effective area of  $A_{eff} = 2.35 \text{ cm}^2$ . For the simulated ARAPUCA, the effective area is slightly larger than this. After an exploration into all of the components of the model and the simulation suite, and a reflection on all of the validations we have performed to this point, we have settled this difference by implementing a "TallBo factor" of 0.7 to the pTP, the least validated input, in the ARAPUCA design.

From here, we simulate both designs of ARAPUCAs, the two sided module for the interior APAs and the single sided designs for the exterior APAs with both the pTP and TPB WLS setup, as well as the TPB and Green WLS setup. The results from the simulations can be seen in figure 3.12, with a full





(a)



(b)

Figure 3.11: (a) The collection efficiency of the simulated ARAPUCA installed in TallBo. (b) The design cartoon of the same ARAPUCA.

summary of the results in table 3.1. The simulation was then finalized for the X-ARAPUCA, which is essentially a repurposed simulation of the designs of the DSLGs with a filter implemented with slight changes. Due to the similarities, no graphs are provided for these configurations but the results are included below.

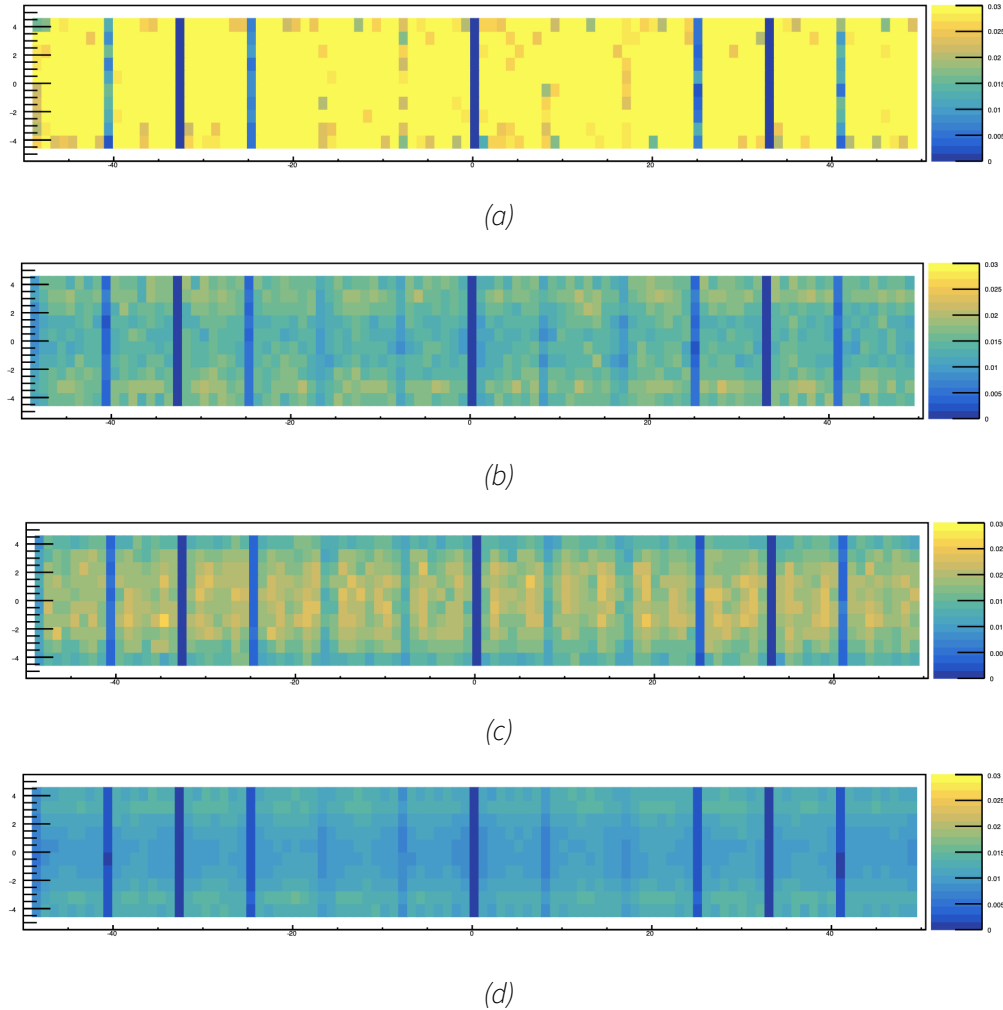


Figure 3.12: Photon collection efficiency for simulated light sources applied across the entire modules for the X-ARAPUCAs with the two configuration of SiPM locations and WLS combinations.

### 3.2 Dichroic Filter Stability Tests

Concurrent with these optimization simulation studies, the individual materials intended to be used to construct the ARAPUCA modules were being tested and characterized. As the ARPAUCA is a very novel idea, many of the components need to be tested in a variety of use cases to better

Design	$A_{eff}(cm^2)$	# SiPMs	$A_{eff}/SiPM(cm^2)$	$g$
DSLGL - End	14.7	48	.31	6.66
DSLGL - Sides	14	192	.07	1.59
Int. ARAPUCA - pTP	27.9	192	.15	3.16
Int. ARAPUCA - Green	21	192	.11	2.38
Out. ARAPUCA - pTP	33.25	192	.17	3.7
Out. ARAPUCA - Green	32.6	192	.17	3.70
X-ARAPUCA End	48.5	48	1.01	21.97
X-ARAPUCA Side	49.62	192	.29	6.30

*Table 3.1: Here, the final results of the simulations is presented for all photon-detector designs presented. The gain in effective area for the X-ARAPUCA over the other designs can be clearly seen, regardless of where the SiPMs are mounted.*

understand the technology. One such test is the longevity test of the dichroic filter in a liquid argon environment. Since this filter is a deposited film on a sheet of acrylic or silica, there is some possibility for flaking with age or sudden thermal shock. As with many materials, the rate of thermal contraction when moving from room temperature to cryogenic temperatures is different between the coating material and the plate. Studies need to be performed to develop a good procedure for thermalizing the plates, and their durability in a flowing liquid cryogenic state needs to be characterized.

To perform this test, a large 50L cryostat was obtained in which to submerge these plates in flowing liquid argon. To simulate flow, an impeller was installed in the lid of the cryostat, reaching into the liquid and moving it around the plates and their mount. The impeller has 4 inch blades pitched at 40 degrees. The volume flow rate from the impeller in a liquid can be calculated from the area of the blades times the frequency of rotation. The resulting flow rate of nearly 1500 liters per second results in an argon flow over the plates of 1m/s. From figure 3.13, every second of operation in the cryostat flows approximately 10 times the maximal flow expected in the DUNE far-detector. The mount was made of stainless steel and consists of two circular disks joined by three legs, leaving a hole in the top and bottom.

The mount was encased with a plastic collar, to direct the flow better over the plates, while still

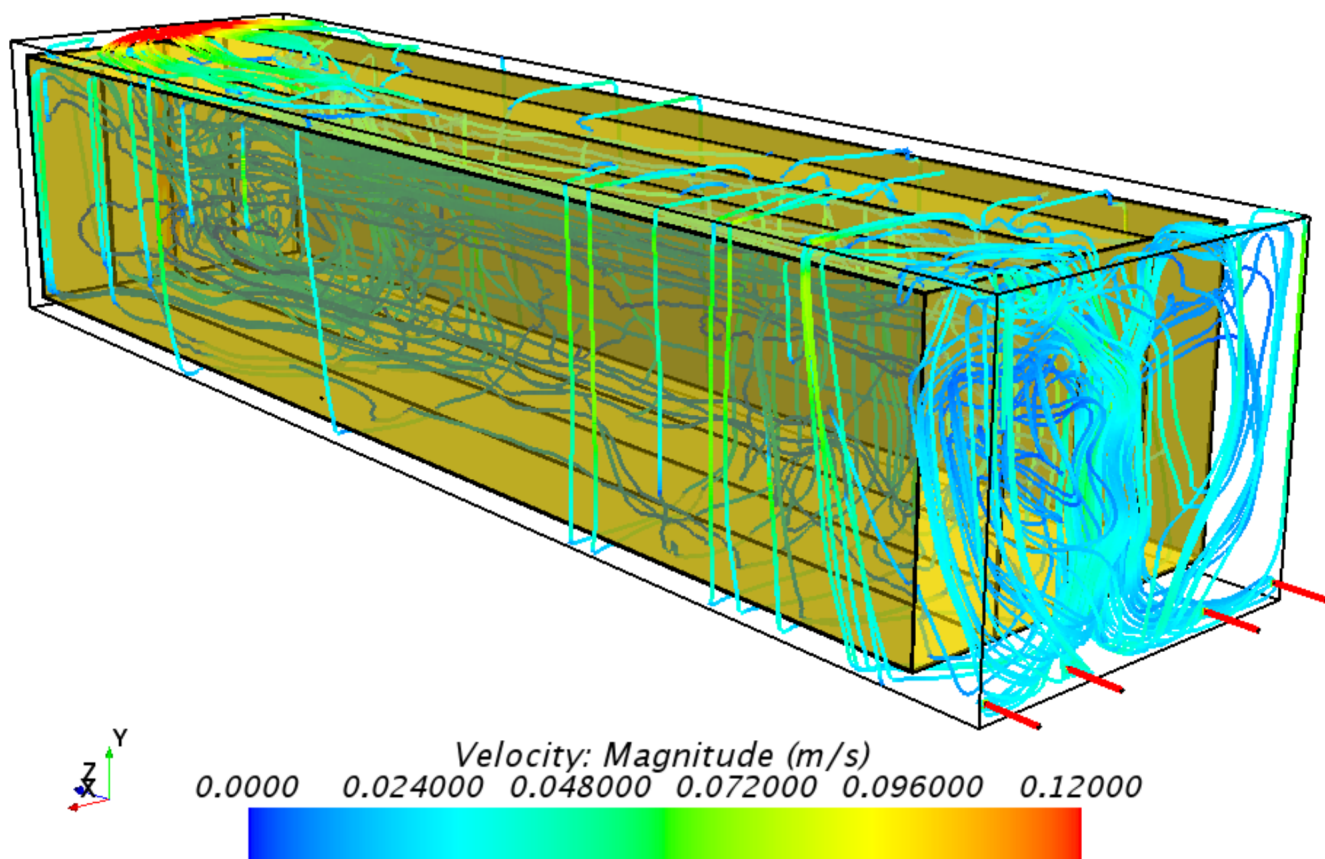
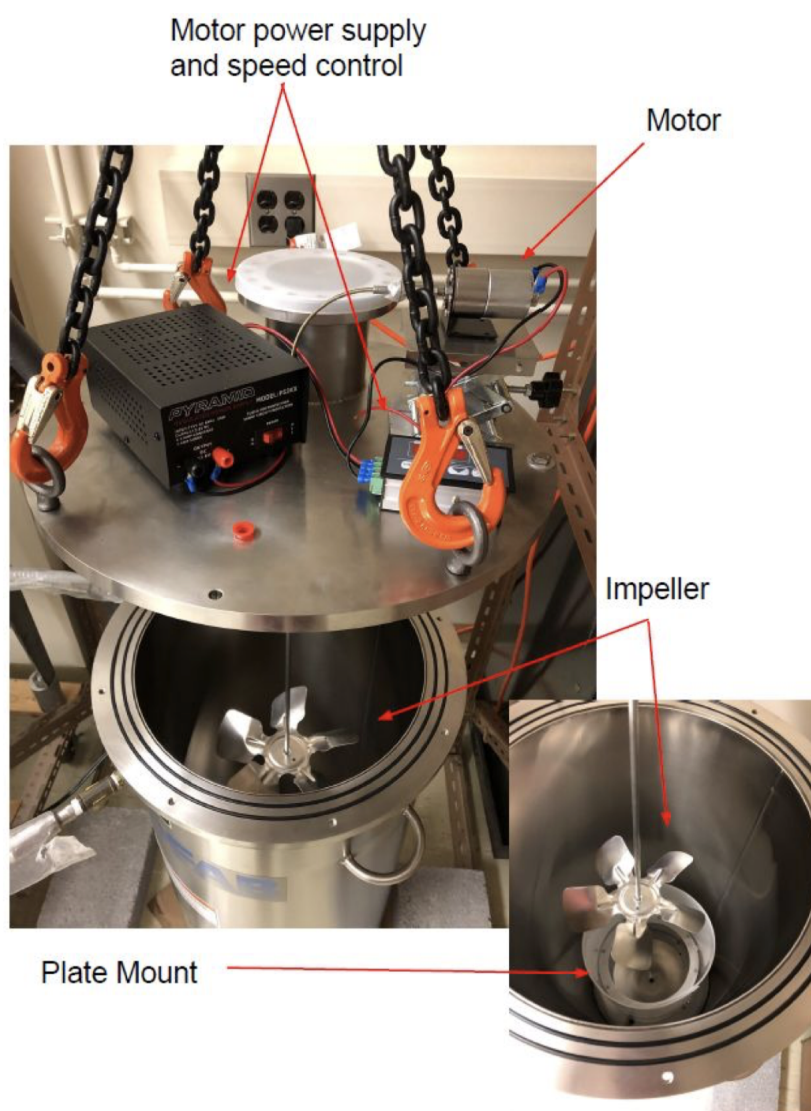


Figure 3.13: A model of the flow of argon within the DUNE far detector. The maximal flow expected is at the reinjection point of the argon and is .1m/s.[60]

allowing adequate access to the plates for insertion and removal. This allows the LAr to flow over the plates mounted within freely, creating a low turbulence environment as would be expected in the majority of the DUNE detector. A photo of the cryostat and mount is shown in figure 3.14.



*Figure 3.14: A labelled photo of the final construction of the cryostat, mount, and impeller used to characterize the transmission of light through the WLS plates.*

Mounted into this setup are silica plates. Initially, a set of six plates with a dichroic filter applied to one side and a TPB wavelength shifter applied to the other side were obtained for testing. Prior to insertion into the flowing argon, these plates need to be baselined, since it is not expected that degradation of either of these coatings will be visible by eye. To measure the performance and re-

sponsiveness of these coatings, a dark box was built in which plates can be mounted and scanned at various wavelengths across their surface. To do this, inside of the dark box there are two rails installed. Along the long axis, a rail is installed on a screw axis, run by a single MODEL stepper motor. The short axis is run by the same stepper motor but is a freestanding screw based actuator mounting on the slides for the bottom two rails. A plate mount was constructed out of slotted aluminum to mount two plates to be scanned.

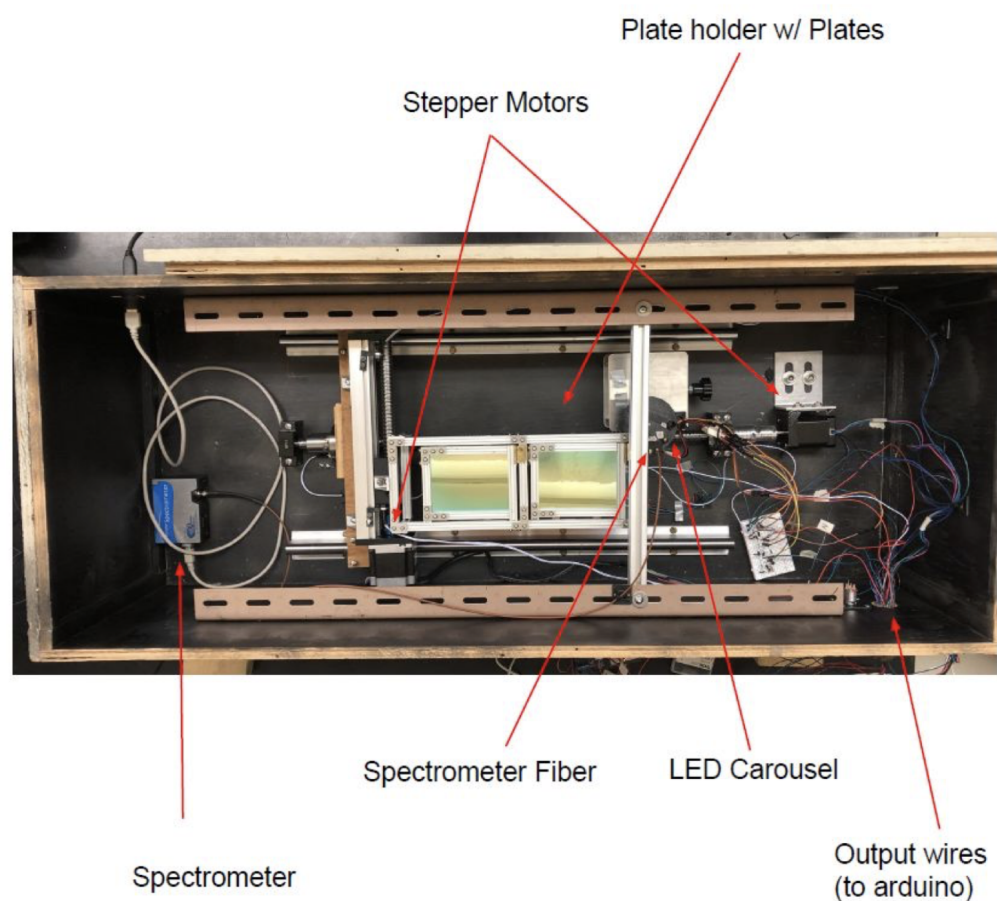


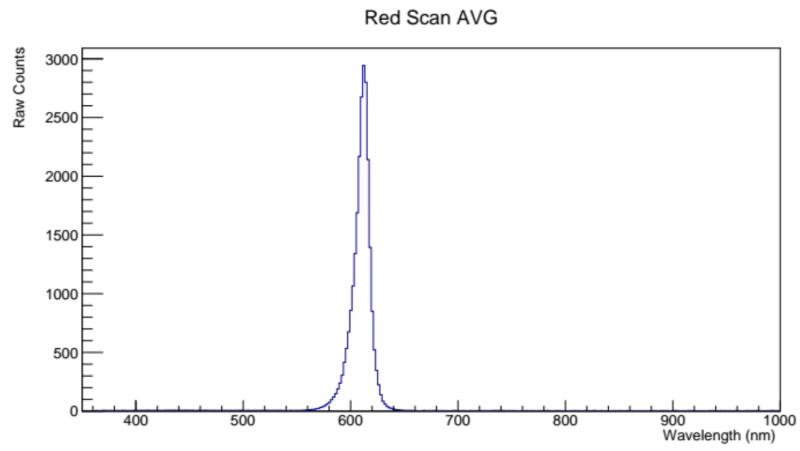
*Figure 3.15: A labelled photo of the final construction of the dark box and scanning mechanism used to characterize the transmission of light through the WLS plates.*

To scan, three LEDs were installed with wavelengths of 610nm, 430nm, and 385nm. The LED wavelengths were chosen such that they were beyond the upper cutoff wavelength of the filter, in the central region, and in the region that can be excited by the wavelength shifter. This multiple wavelength illumination allows for a characterization of both the dichroic filter and WLS on the plate.

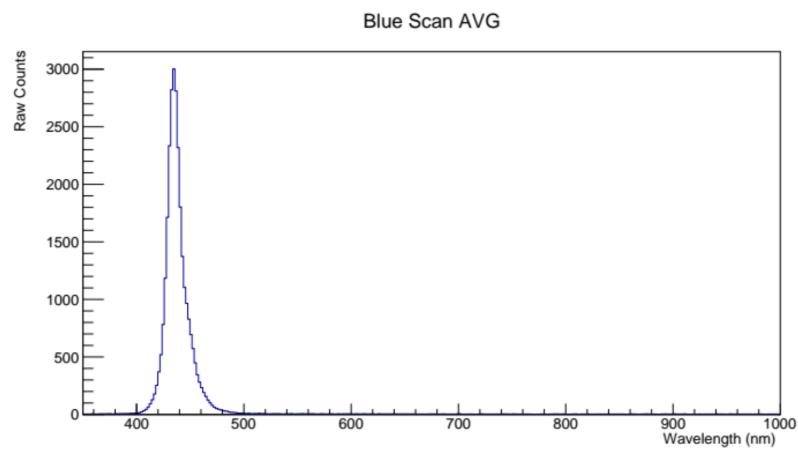
These LEDs are mounted on a carousel, which is mounted on a servo motor and can be controlled to illuminate one point with all four LEDs consecutively. The light that passes through the plate is readout by a OceanView Spectrometer. The completed dark box setup is shown in figure 3.15

The entire setup is automated and is controlled via an Arduino Mega micro-processor. This micro-processor was coded to have a series of functions that perform the necessary tasks, i.e. one to move a servo, one to shift the stepper motors and the axes, etc. This Arduino communicates with LabView via the Wolf package, allowing LabView to send commands to the Arduino and collect data. A LabView interface was designed, allowing the user to control the number of points scanned in both directions, the number of plates scanned per run, save the file in a user-defined location, and have live updates as the scan occurs. A screenshot of this interface is shown in figure ???. The spectrometer also interfaces with LabView, allowing the code to signal when to readout the spectrometer and collect data. To validate the performance of the spectrometer, as well as to baseline the gain and light readout signals and check for proper alignment, a series of calibration and stability runs were performed on the LEDs. First, a simple readout of the LEDs illuminating the spectrometer, shown in figure 3.16, was taken. Runs were also taken ten and eleven days after this initial run to see if the LEDs were stable over time. These stability graphs are included in figure 3.17. This allowed validation of the readout scheme by comparing the data to the provided spec sheets for the LEDs. This also allowed for calibration of the integration window of the spectrometer. If left to read in light for too long, we saturate the readout and no longer have a proper understanding of how much light is expected to be illuminated on the plate.

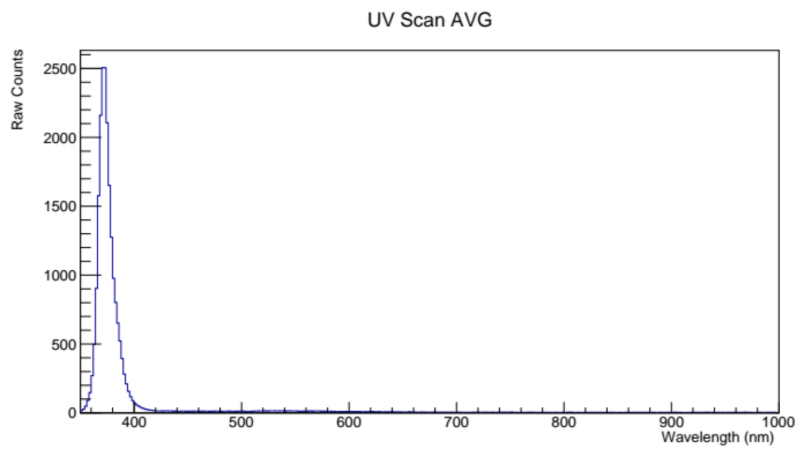
The procedure to run was designed so that the expected LED emission was taken before each plate was illuminated. This means that when the run is initialized by the user, the plate mount moves out of the way and a series of data are taken where the LEDs directly illuminate the spectrometer. This process is repeated after the plate has been scanned, and the average of these two illumination profiles is used to calculate the LED intensity incident on all points in the scan. After the scan is taken, the spectrometer and location data is stored in a multi-line text file, which is then imported into a



(a)



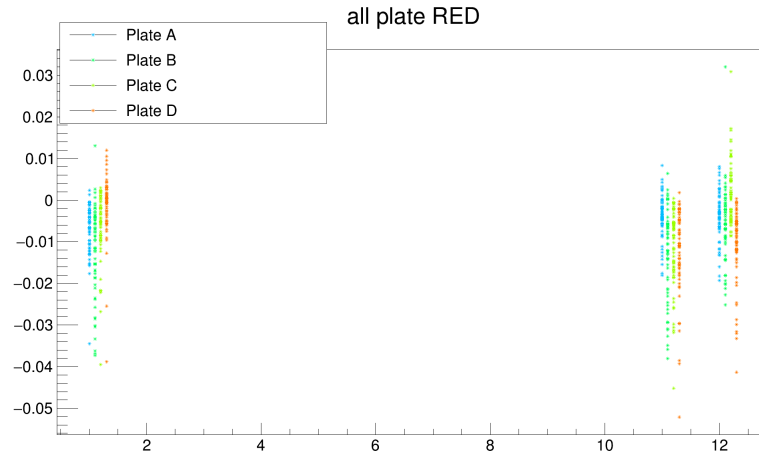
(b)



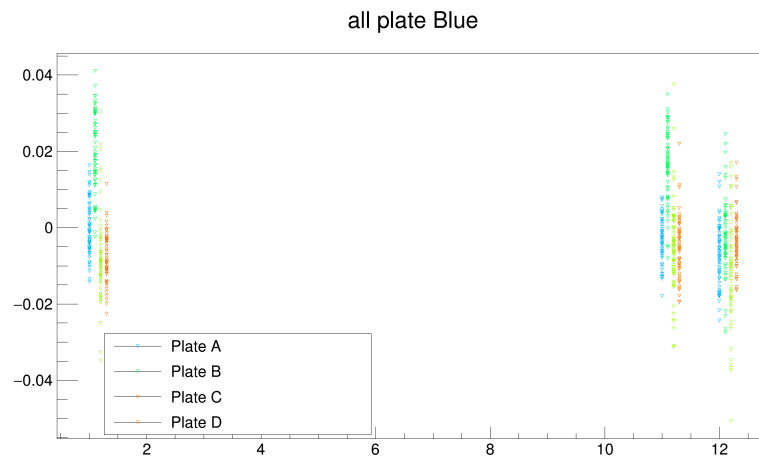
(c)

Figure 3.16: Output spectra of the (a) 610nm LED, (b) 430nm LED, (c) 385nm LED.

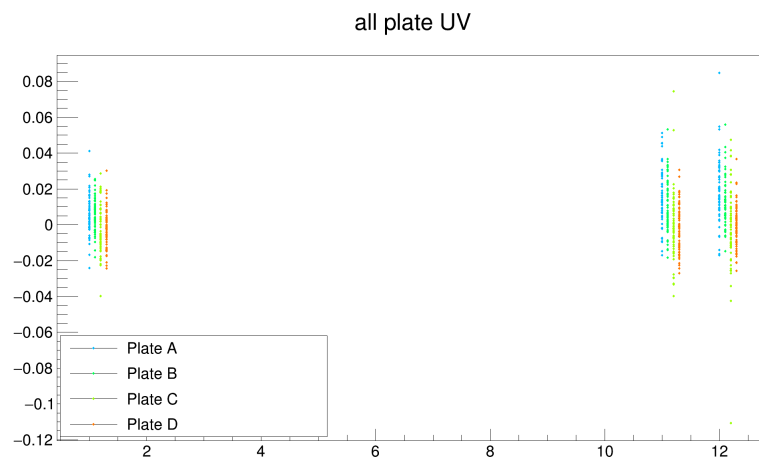




(a)



(b)



(c)

Figure 3.17: Stability plots over multiple days for the initial 3 LEDs in the dark box setup. (a) The 610nm LED. (b) the 430nm LED. (c) the 385nm LED.

custom ROOT code where the readout from the spectrometer is integrated over the LED emission range and plotted for every point scanned. An example of these for a coated acrylic plate for all three LEDs is shown in figure 3.18.

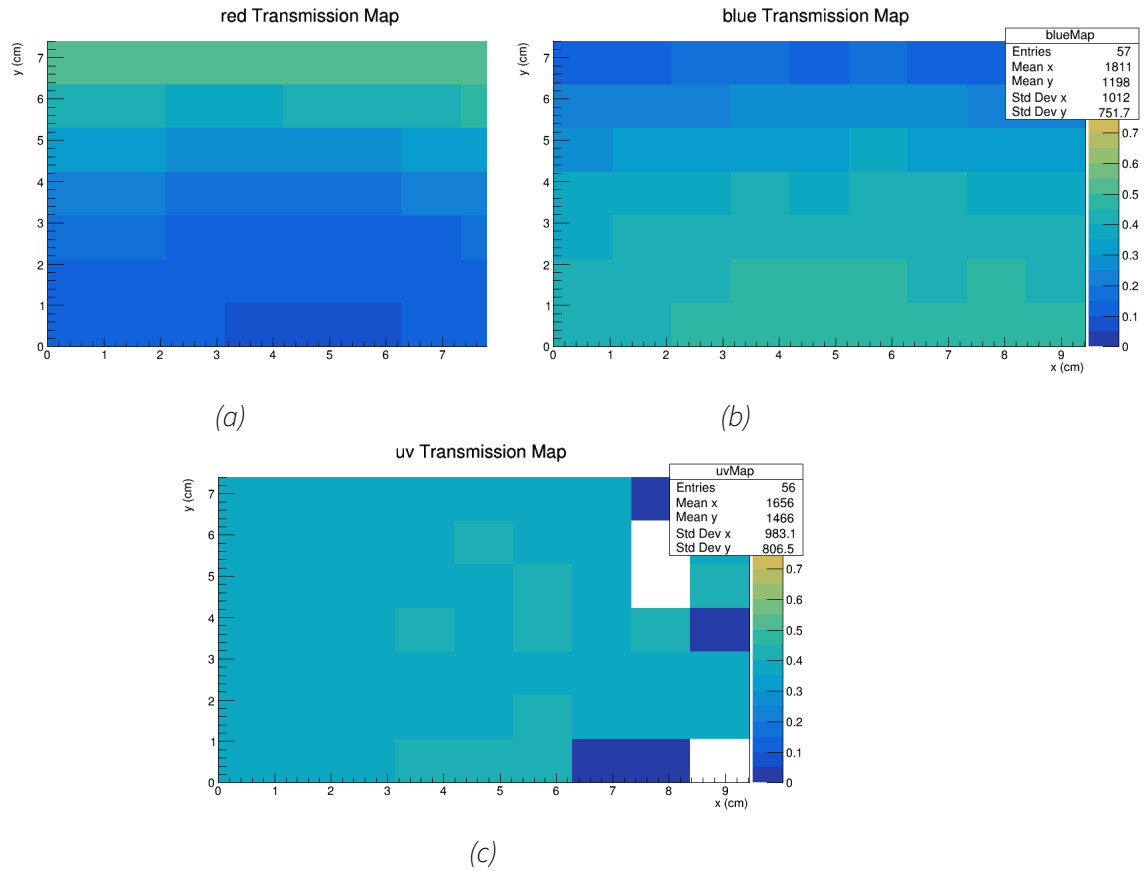


Figure 3.18: Transmission maps for a clear acrylic plate used to baseline the darkbox scanning procedure.

Before inserting the plates into the liquid argon, it was noted that the plates exhibit a circular pattern in their transmission of red and blue light. There seems to be a clear non-uniformity in either the WLS or dichroic filter coating, with the latter being significantly more likely, given the nature of the coating and light response. With this gradient, it would seem that the dichroic filter coating was applied in such a way that the lower edge of the plate got a thicker layer than the top. An analysis was performed to look at the wavelength transmission at a point roughly equal to (4.5, 2) and (4.5, 5), labelled "bottom" and "top", to see how these two points react to light illumination. When analyzing the detected spectra at these when compared to the incident spectra, one can see that

the two points have different wavelength dependent behavior as in figure 3.19. The far right edge of the spectrum for the blue LED differs between the two points, as does the far left side of the red. There are of particular interest because these are right at the interaction with the dichroic filter. Figure 3.19c shows how the transmission spectra at the two points differ from each other, as well as how they compare to the theoretical reflection and transmission curves. It can be seen that there is a fairly stark disagreement between the two.

After consulting with the manufacturer, it was decided that the circular pattern that results in non-uniform layers of filter thickness was a result of the coating process. Though the effect appears quite stark in these maps, the difference in thickness does not appear to have a negative effect on the filters. Nonetheless, the coating procedure was slightly changed to help alleviate this effect. A second set of plates was later received for this testing and, as will be seen, they do not exhibit this behavior.

The misalignment between the data and expected values of the dichroic filter cutoffs is the result of the angle of incidence of the incoming light. Within the LArTPC, the average photon has an angle of incidence of  $45^\circ$ , so the dichroic filter was designed as such. The filter does have some angular dependence, and the  $90^\circ$  angle of incidence that was designed in this scanning procedure shows the deviation with angle in the cutoff wavelengths. This issue was addressed with the manufacturers and the filter was tuned to reduce this discrepancy, since it could have a appreciable effect on the detection efficiency in the detector.

Given the interaction with the dichroic filter a fourth LED was obtained and installed in the dark box, a ThorLabs LED525L, with a wavelength of 525nm. This lies firmly in the reflection window for the dichroic filter, and allows for a better characterization of any degradation of the filter.

To summarize, prior to submersion in the LAr, we have profiled the plates with LEDs that are firmly in the reflection band of the filter, firmly in the transmission region, and overlapping both edges. For the initial run, only two plates were inserted into the cryostat. This left two plates as backups if

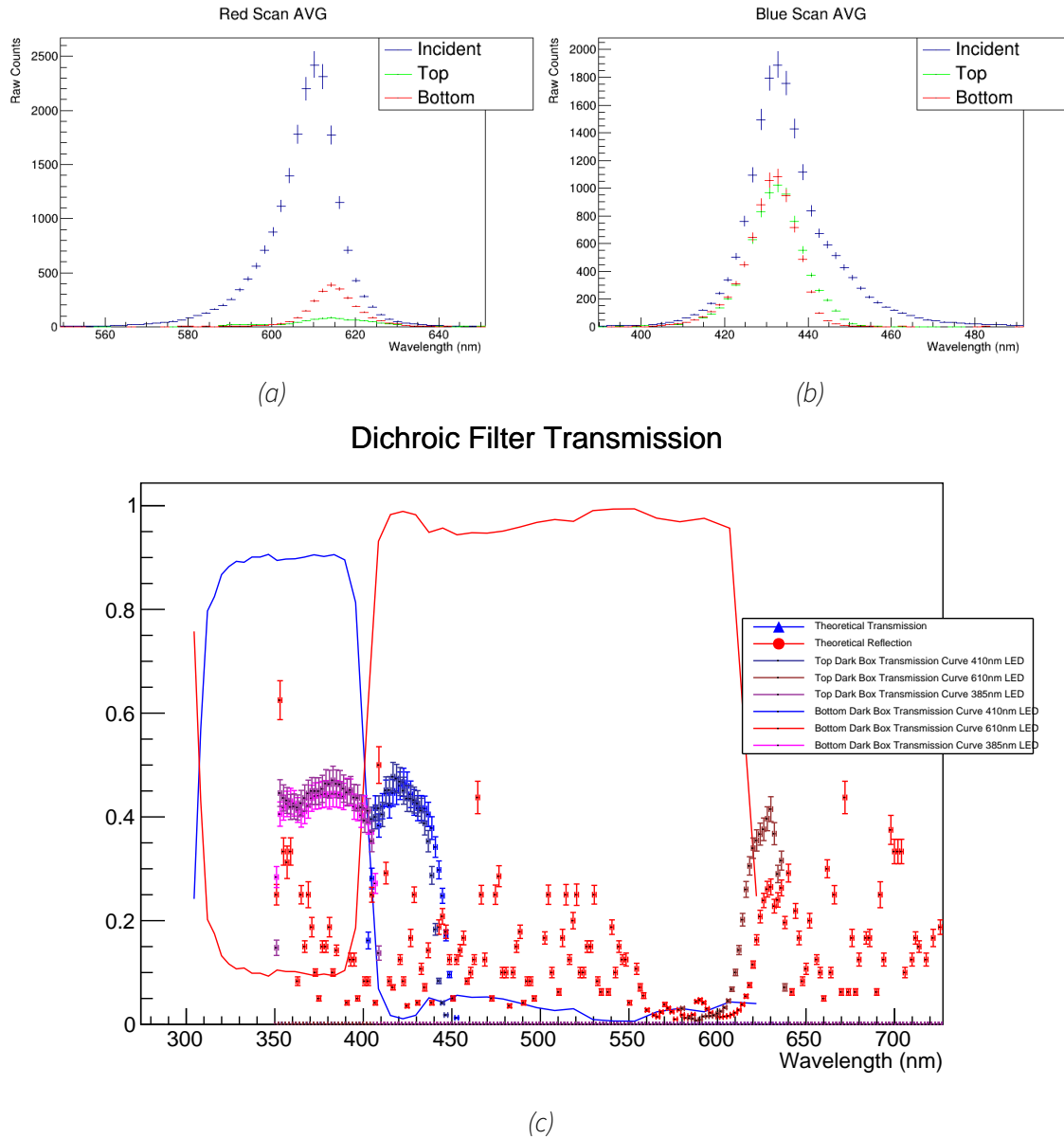
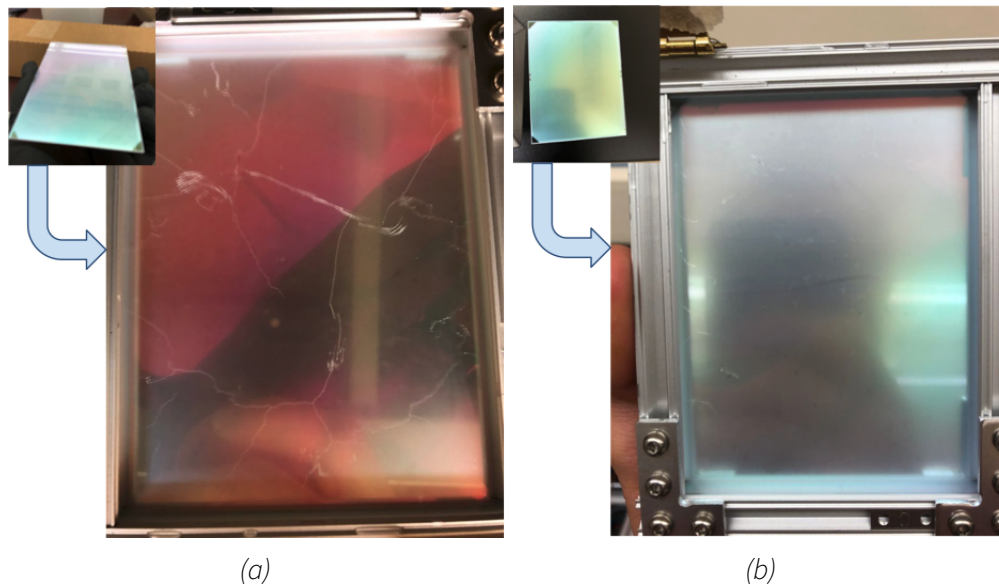


Figure 3.19: The incident and transmission wavelength for two points on opposite edges of the plate for the (a) red and (b) blue LEDs. A clear shift due to inconsistent coating can be seen. (c) The total spectra of these two points plotted over the cutoff wavelengths of the dichroic filter, which clearly exhibit unexpected behavior.

something about the thermalization process went poorly and ruined a plate. The two plates were inserted into the cryostat and then exposed to a trickle gaseous argon for two days, allowing them to thermalize slowly. The cryostat was then filled over the course of three days, reaching liquid argon temperature slowly to prevent shock. After this, the impeller was set to a speed of 60RPM and the experiment was run in this state for 220 hours, with daily top-offs of LAr to compensate for boil off. This was the equivalent of nearly 90 days in the far detector environment.



*Figure 3.20: Before and after photos of the two plates used for stability tests in run-I.*

To thermalize back to room temperature, the impeller was shut down and the LAr was allowed to boil off, while again trickling in gaseous argon. While in the gaseous argon, the plates were lifted out of the remaining liquid and slowly allowed to come to room temperature. Once at room temperature, the plates were visually checked for defects. Photos comparing the plates before and after submersion are in figure 3.20. They were then scanned using the same procedure as before insertion. The output transmission maps were analyzed to check for obvious differences, comparing the absolute change in transmissions. Histograms of the absolute change in transmission at every scan point for both plates are shown in figure 3.21, with a summary table in 3.2. Despite the obvious crazing seen in the first plate's WLS layer, most likely from thermal shock, the scan results do not differ drastically from the second plate. Both showed an increase in transmission for the 385nm

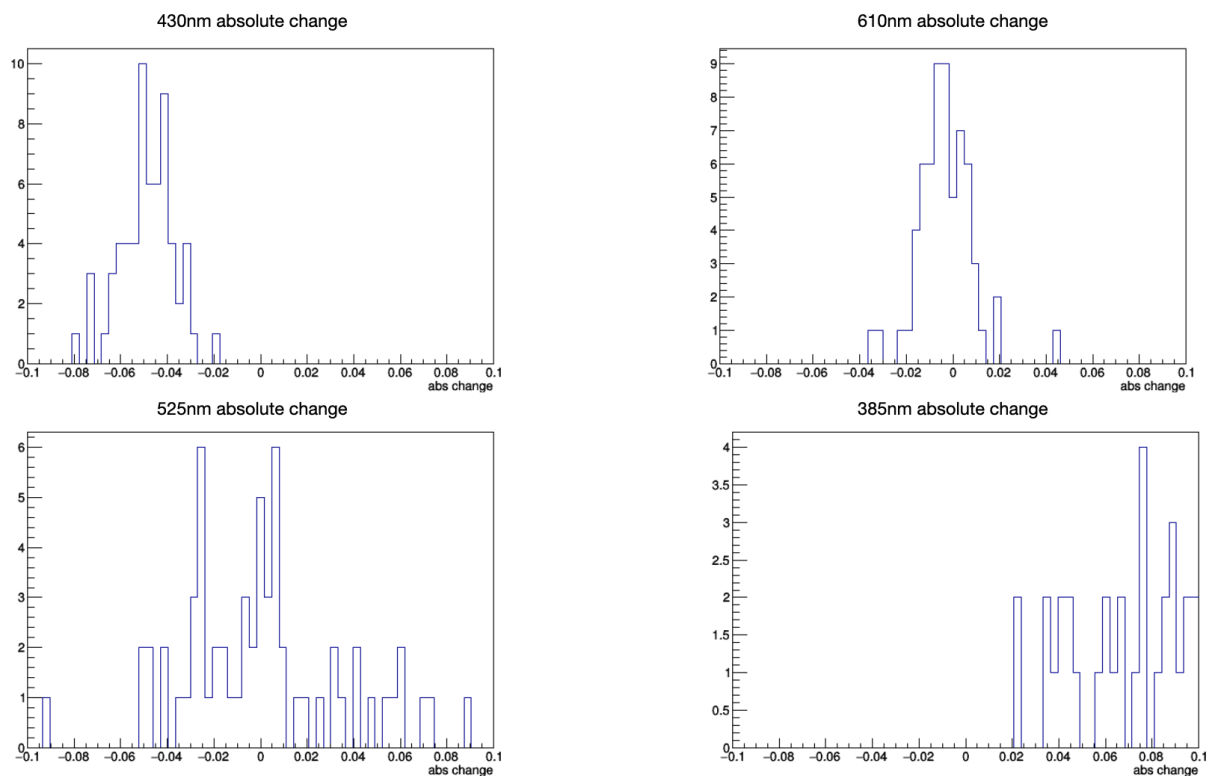
and 430nm LEDs, those in the transmission window of the filter, but were stable over the higher wavelengths. There was also no physical sign of degradation of the dichroic filter over this period.

Wavelength (nm)	Plate 1 Transmission	Plate 2 Transmission
385	10% increase	5% decrease
430	5% decrease	6% decrease
525	stable	stable
610	stable	stable

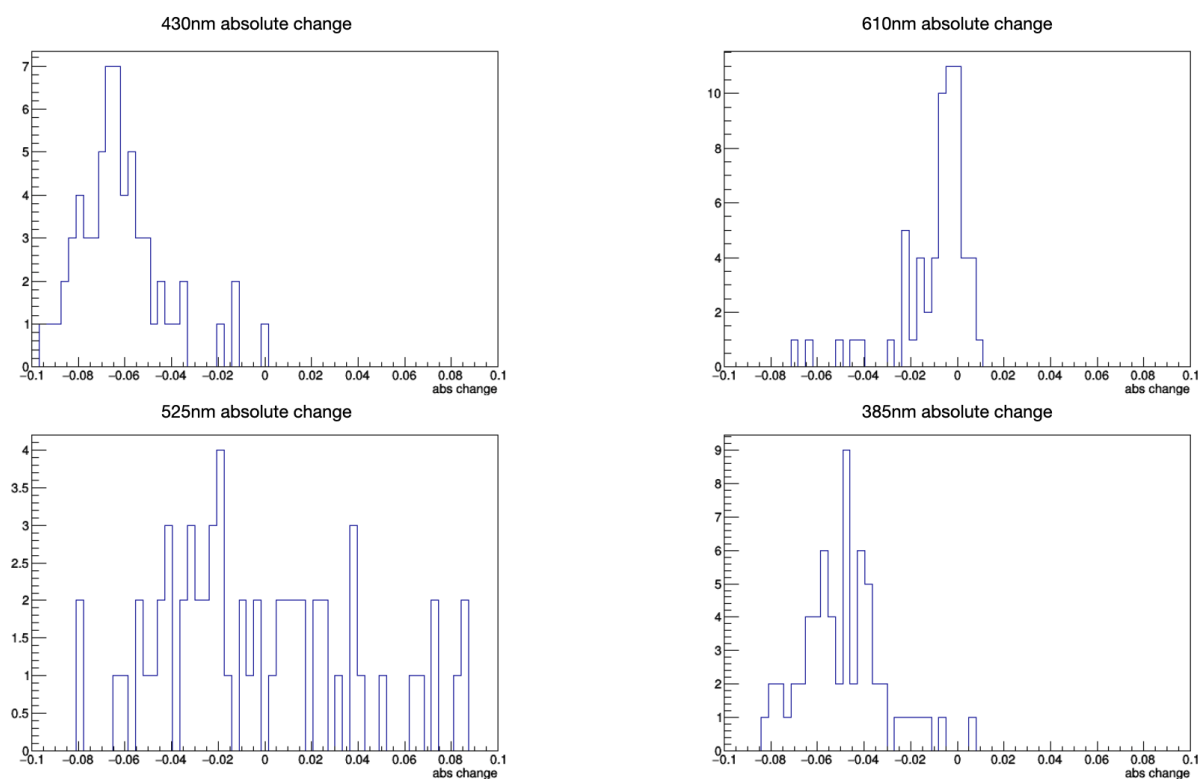
*Table 3.2: The total changes in the transmission and conversion of the two plates after submersion in LAr for run-I.*

After this study, four new plates were obtained, with dichroic filters from OPTO, and a WLS coating performed by the scientists at UNICAMP. These were coated using an updated procedure and showed more uniform photon response, as well as a more expected response to the dichroic filter. A fifth LED was also installed in the carousel, a ThorLabs LED285W 285 nm LED. This wavelength is within the excitation region pTP, meaning that this additional LED gives us insight into how the WLS is affected by submersion. This is well out of the detection spectra of the spectrometer used, so any light observed in these scans is from excitation of the WLS. Figure 3.22 shows the response of one plate to all LEDs. The 525nm and 610nm is almost entirely undetected, as both of these wavelengths lie in the reflected region of the dichroic filter. The 385nm light is almost entirely transmitted, which is expected from the dichroic filter transmission range. The 430nm light lies just past the cutoff wavelength between the two filter modes, and has a spread of approximately  $\pm 10$  nm, so some light is transmitted, as shown in the map. A value greater than 1, indicating more detected photons than were measured in the calibration scans, is calculated for the 285nm LED, indicating a fairly uniform excitation of WLS and subsequent transmission of that light. This response is standard for all four plates.

This second run lasted 24 days, resulting in nearly 480 hours under flow, which is roughly equivalent to 166 days of exposure in the DUNE-FD. The plates experienced one thermal cycle, and before and after photos are given in figure 3.23. Following the same scanning procedure as before, the



(a)



(b)

Figure 3.21: The absolute change in the transmission for both of the plates submerged in LAr for run-1 of the stability tests. A clear shift can be seen in some, but not all wavelengths.

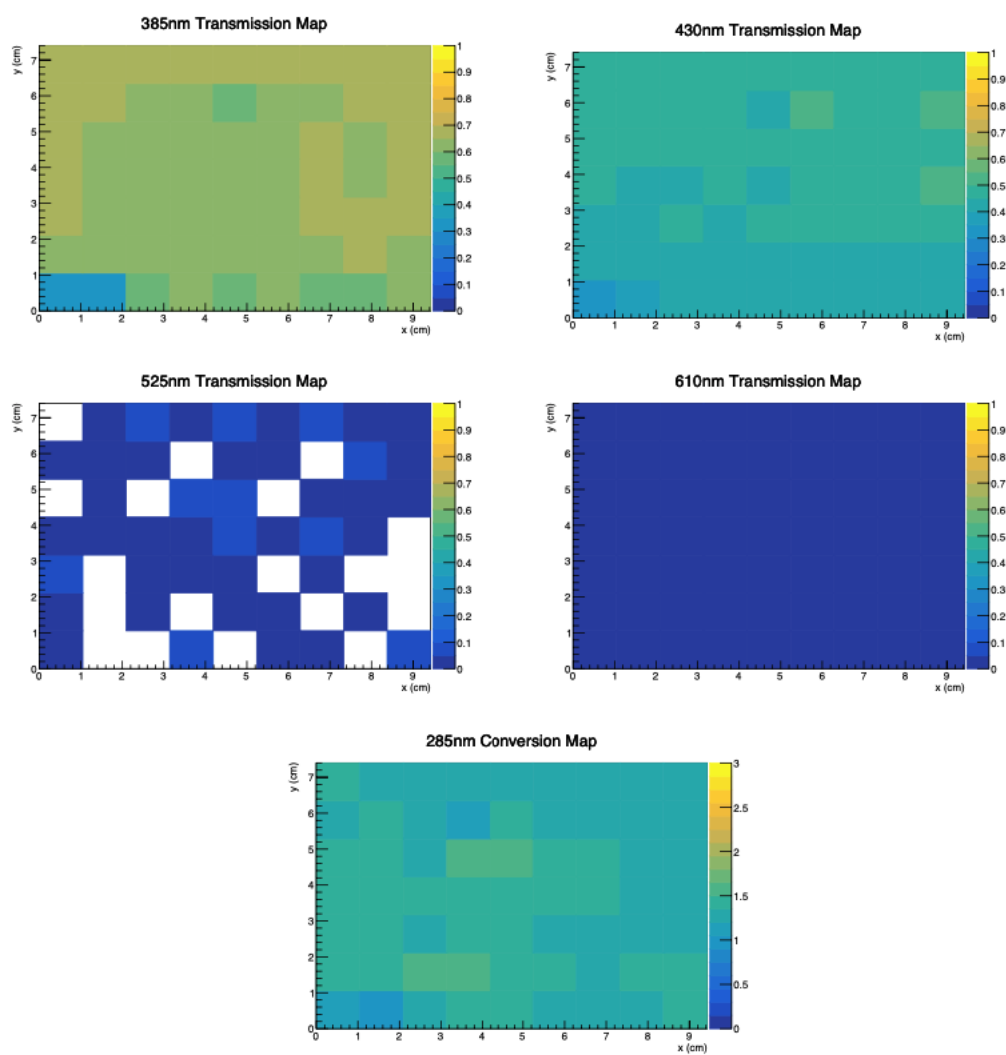


Figure 3.22: The absolute change in transmission and conversion maps for a single plate from run-II.



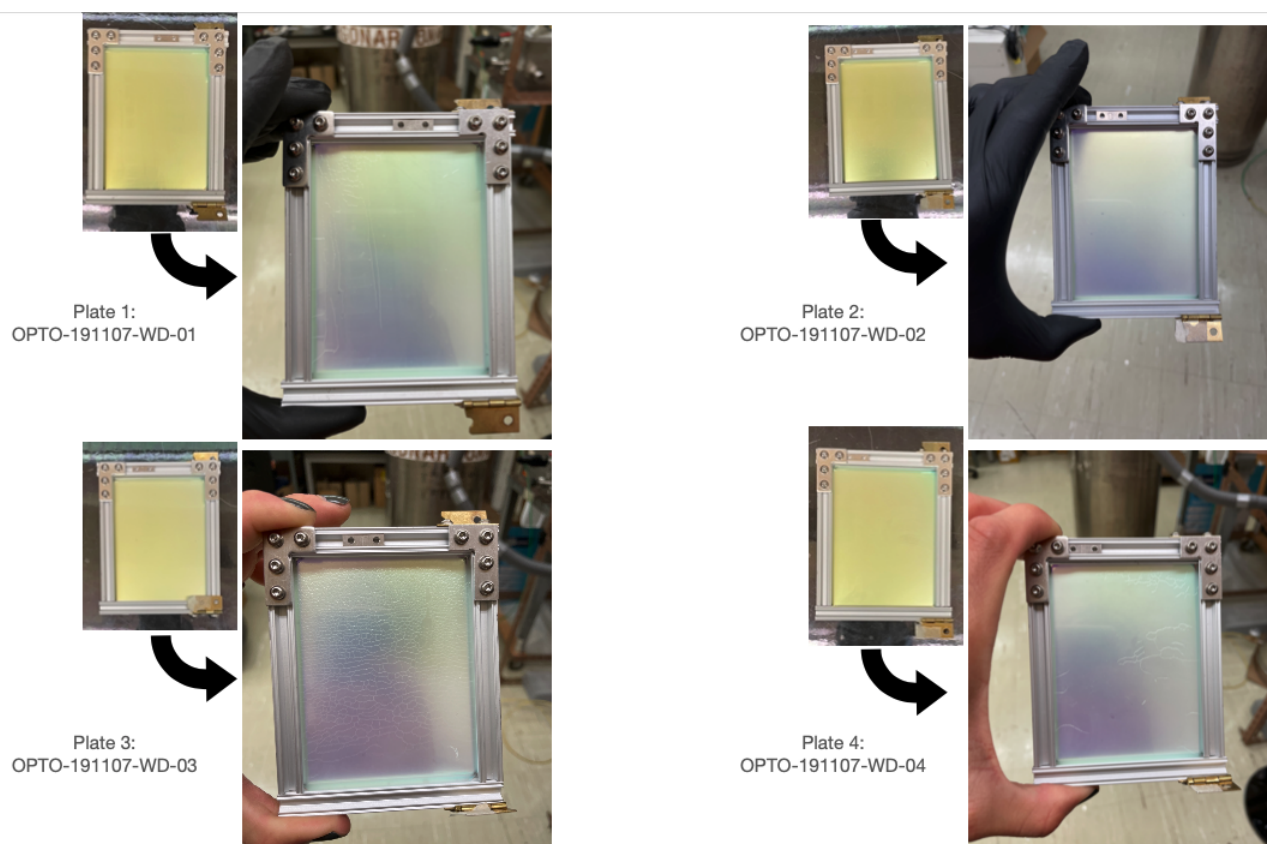


Figure 3.23: Before and after photos of the four plates used in run-II of the stability tests. Crazeing can be seen on two of the plates, likely due to thermal shock.

Wavelength (nm)	Dark Fluctuations	Plate 1	Plate 2	Plate 3	Plate 4
285	-	20%	30%	stable	stable
385	$\pm 2\%$	5%	3%	2%	5%
430	$\pm 2\%$	5%	3%	2%	4%
525	$\pm 2\%$	stable	stable	stable	stable
610	$\pm 2\%$	stable	stable	stable	stable

*Table 3.3: The total changes in the transmission and conversion of the four plates after submersion in LAr.*

results from this second run are reported in table 3.3. As with the first run, there is a slight increase in the light transmission in the region below the dichroic filter cutoff. There also seems to be a substantial increase in the excited light from the 285nm LED in two of the four plates, though this is the least controlled number. Apart from these, there does not seem to be any substantial change to the performance of the plates, despite two plates having clear damage from thermal shock. Overall, these are positive results for the stability of these coating in the DUNE-HD detector.

## Chapter 4

# Measurement of Attenuation of Light in Liquid Argon

### 4.1 Data selection

Data used for the pure LAr analysis was taken between the commissioning of the PDSP detector, and May of 2019. During this time, the liquid argon purity was calculated using the measured electron lifetime, which averaged above 30ms during all data collection periods. The event readout was triggered by a coincident signal in one front and one back CRT panel, with a coincidence window of 80ns. As stated in section 2.4.3, the layout of the beam-pipe and CRTs, the spacing between front and back assemblies on the beam-left side was shorter than the beam-right side, which caused this CRT trigger coincidence window to bias data to the beam left side. For this reason, and the central location of the ARAPUCA in the APA plane, this analysis uses only data from this drift volume.

Since a measurement of the light attenuation necessitates a strict understanding of the track location, building a track and photon detection system matching algorithm was necessary. Though the time matching of the PDS and CRT was well understood by this point, a better understanding of the TPC timing and location matching was important to improve resolution. The TPC timing relied heavily on a firm understanding of the raw data fragments from the CTB. Since the detector is still

prone to a front to back ambiguity, position based matching with a second subsystem was also very important.

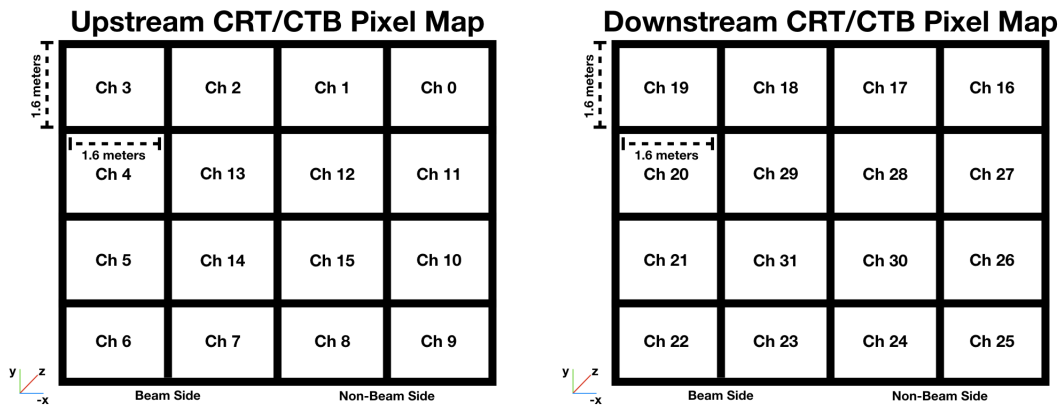


Figure 4.1: A labelled map of the front and back CRTs, with CTB channel numbers and dimensions labelled.

Position matching to the PDS is a possibility, as position is built into the structure of an optical flash, but with ProtoDUNE sitting on the surface and having a high flux of cosmic activity there is no way to guarantee an optical event lines up with a TPC event. The CRT panels, however, are the perfect medium for position matching to TPC tracks. Once two CRT signals have been detected, one can create a "track" by drawing a line between these two points. If a TPC track is well aligned with this line, then a match is found. However, the very large size of the CRT makes this an imprecise measurement, unless one has access to the fine grain resolution of the internal straw tube channels that make up the CRT panels. Though not originally planned for use in PDSP, the CTB raw data fragments carry the individual CRT straw tube channel information that can be interpreted and utilized, as long as one understands the map from channel to position. This information was located and mapped in another study, and implemented in this work.

Mapping the CRT pixels, a coincident hit in two intersecting straw tubes within the panel, can be done in a variety of ways. The simplest method is, naturally, brute force. After collecting a large number of CRT triggered through going tracks, one can find the individual channels that were activated in the trigger and time match that to the trigger itself. Given enough coverage of the detector,

a complete map should be attainable. Once this is complete, matching TPC Tracks by position and pairing this with a time matched CRT-PDS system allows for a precise determination of which track has caused the light signal and event trigger.

The distribution of cosmic ray muons incident on the PDSP detector can be seen in figure 4.2, which shows the hits on both of the front and back CRT modules. The beam left bias can be seen here, as well as the general direction of the muons. They typically come in with a downward trajectory, and are typically traveling from the BL to BR side of the detector. There is some concern that this could introduce some geometrical bias in the light yield. The central location of the ARAPUCA alleviates this, which was the sole purpose of its chosen positioning here. For the DSLGs, the possible geometrical effects are largely removed due to the full coverage these modules have in the APA planes, with DSLGs of both sensor type covering top to bottom in one APA.

Events were selected using a matching algorithm between the pandora reconstructed TPC track, and the flight path created by the hits in the front and back CRT panels. If the cosine of the angular difference between these is larger than .99, the event is rejected. The TPC track beginning and end must also be located within  $40\text{cm}$  of the projected CRT track entry point in both the x and y coordinates. The selection criteria results in a  $> 99\%$  purity in selection of through going muons that produce a TPC track. The start point of the track was also subject to a fiducial volume cut, defined here as within  $350\text{cm}$  of the cathode, and  $10\text{cm} < y < 580\text{cm}$ , which encompasses most of the detector but removes any track originating too close to the edge of the TPC. The previous selections still allow for tracks to originate in one drift volume and pass into the other, possibly resulting in a triggered event that records lower than expected photon yield, particularly near the far distance samples. To alleviate this, we implement a strict cut that the start and end points of the track lie in the same, beam left, drift volume.

For the PDS, a light scintillation signal must be readout in any module in 2 of the 3 APAs within  $2\mu\text{s}$  of the CRT trigger time. This cut serves as a backup for the TPC matching, and also removes low-light outliers from the final sample. If an event passes the PDS and CRT cut criteria, the log of the

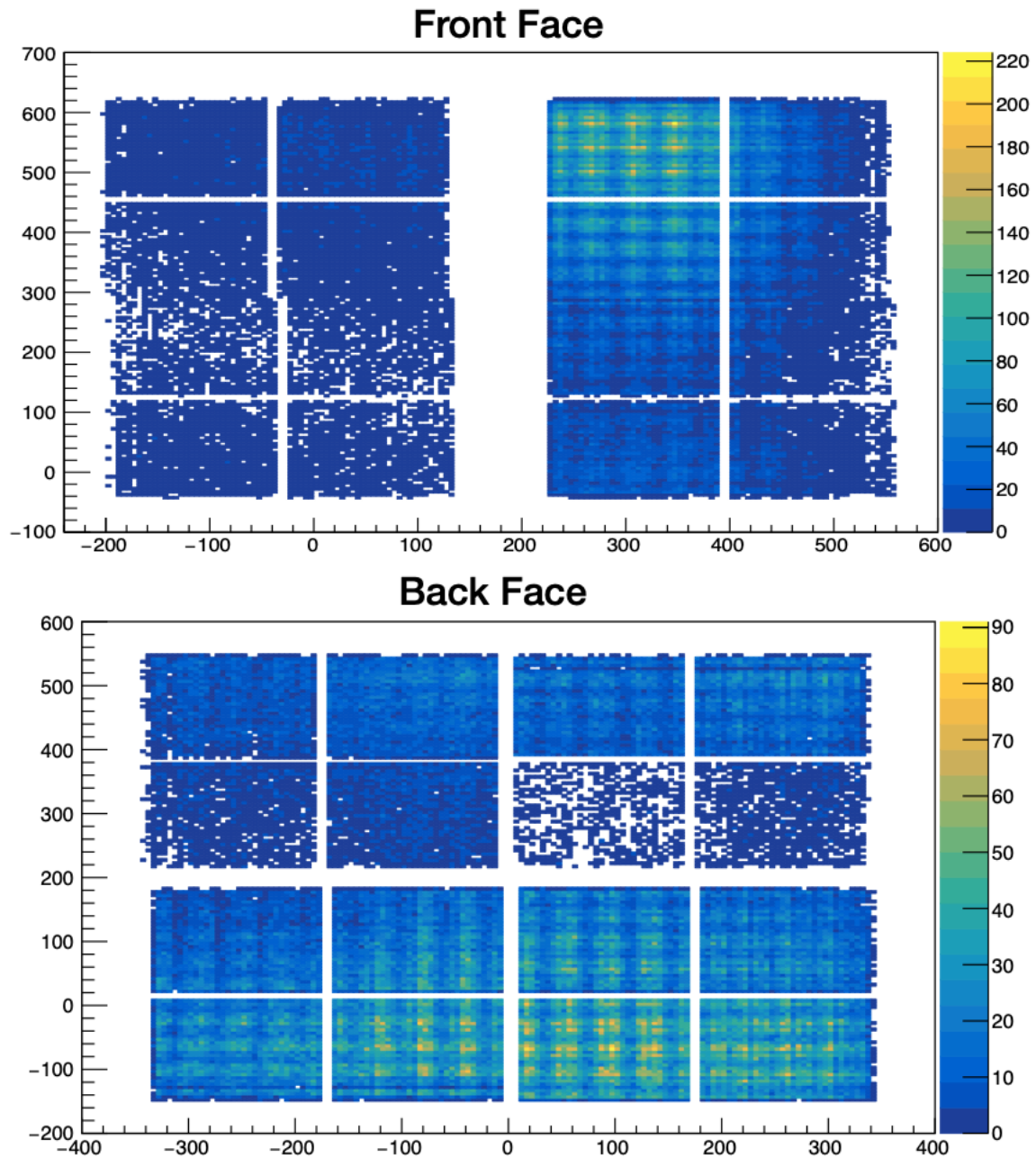


Figure 4.2: Distribution of CRT hits on the front (top) and back (bottom) CRT panels for all events recorded during the entire data-taking period. The left-right asymmetry in the front CRT face is clearly visible here.

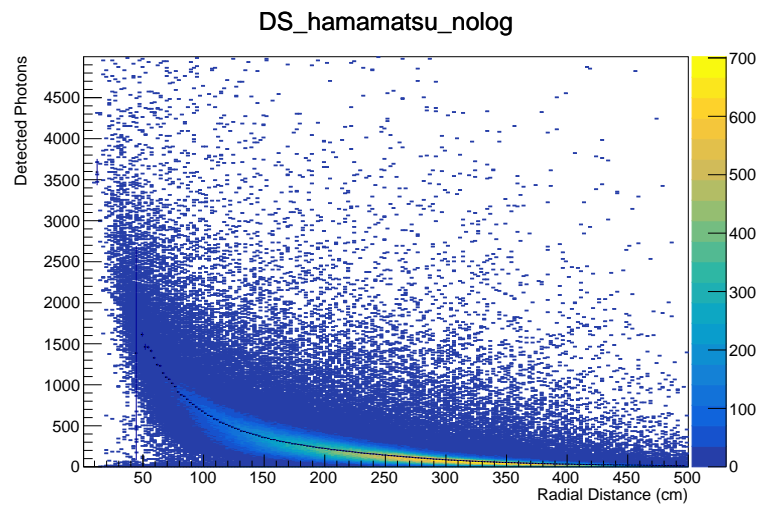
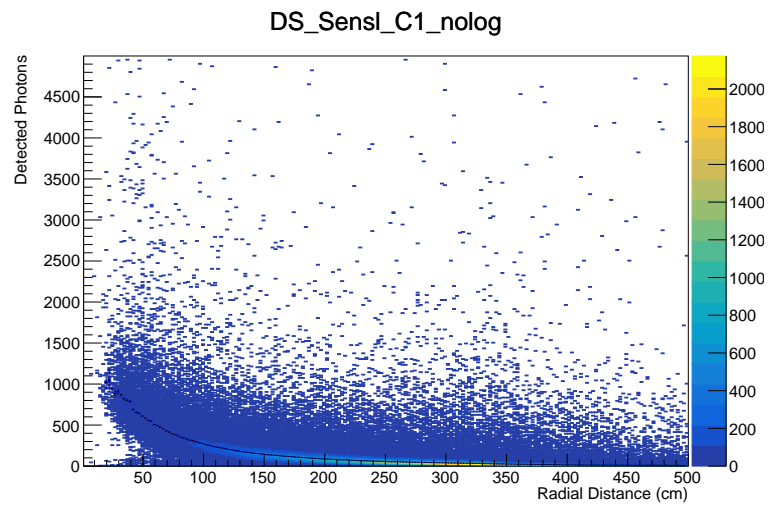
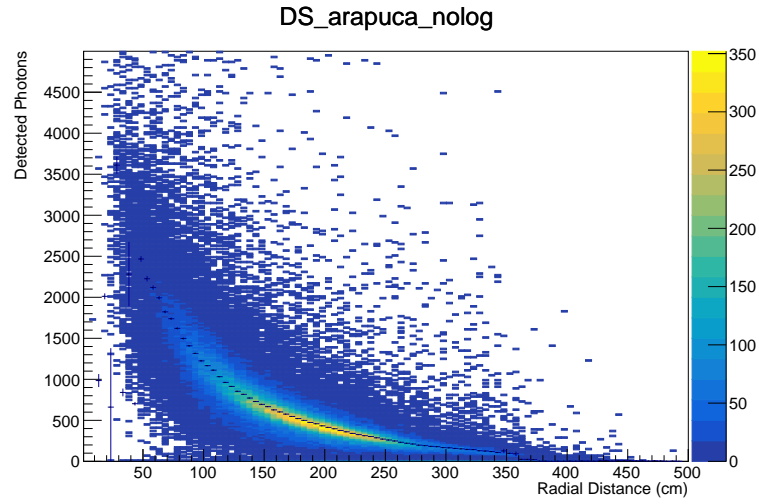


Figure 4.3: The light yield versus radial distance curves for the three detector groupings.

number of detected photons on all PDS modules is recorded as long as more than one photon was incident on that module and also that the module was not saturated. For every passing track, the radial distance between the center of the individual PDS modules and the point of the track that passes closest, in the z-direction, to that module is recorded. We choose the log of the number of photons so that we may more easily cut out the low photon noise we expect to be our main source of error. A measurement of the log of the number of photon less than one is removed, and the data is then exponentiated.

This data is then plotted in a 2-dimensional histogram, as see in figure 4.3, and the light detection as a function of distance from the photon detector module is observed. Due to high noise rates, the dip-coated light guides are not included in the analysis. The double-shift light guides are grouped into two categories, one for each type of readout SiPM, since the two have very different gain behaviors and are not directly comparable. For these two groups, there is one data point in the final plot for each individual DSLG bar, meaning that the two DSLG plots will have nearly ten times the number of entries of the single ARAPUCA plot. The 2-dimensional histograms are then profiled along the distance axis by fitting the central 66% of each bin with a gaussian function to produce a trend line. The resulting profile, superimposed on each distribution in figure 4.3 is not a direct measurement of the attenuation length but serves as a pseudo-attenuation curve, representing the effective attenuation of the liquid argon scintillation light from absorption and Rayleigh scattering.

## 4.2 Simulation

To determine the Rayleigh scattering length from the pseudo-attenuation curves, we simulate cosmic-ray muons in ProtoDUNE-SP under a variety of simulation parameters to find the configuration that best matches the data. From the tracks that pass data selection described above, the reconstructed track start positions and momenta are recorded. This information is then fed into a single particle gun monte-carlo generator and 6 GeV muons are simulated in the ProtoDUNE-SP detector using the standard ProtoDUNE-SP simulation procedure using Geant4, within the standard ProtoDUNE-



SP geometry. Due to the extremely large size of ProtoDUNE-SP, the simulation of the scintillation light is omitted from the Geant4 simulation, and instead relies on a pre-generated photon library. This library is generated separately and serves as a look-up table for all particle generating monte-carlo.

To generate the library, photons are simulated in  $10^6$  voxels,  $100 \times 100 \times 100$ , within the active volume under a specified set of liquid argon scintillation properties. Within each voxel, the probability of a photon reaching the photon detectors is determined, and this probability is used to determine the number of photons incident on the PD from a generated track given its energy deposition. In the simulation, all PDS modules are simulated with the same quantum efficiency (QE), which is calibrated off of a DSLG with SensL-C1 SiPMs. A quantum efficiency (QE) of 0.41% is assigned to each module corresponding to the value measured in a separate study [57]. The simulated number of scintillation photons incident on the module is multiplied by this QE factor, the attenuation along the length of a typical DSLG, and a reduction factor of 70% to model shadowing from the APA wire plane.

Using the data tracks as inputs to the simulation reduces fluctuations in incoming muon tracks and allows for fewer systematic errors in this procedure. Once simulated, only the PDS readout is reconstructed, to save computational time, and the radial distance is calculated as the distance from the center of the PDS module to the point of closest approach of the vector created from the start and end point of the true monte-carlo track. Two dimensional histograms similar to those in figure 4.3 are created for all combinations of simulated parameters and profiled as described above. As seen in figure 4.3 , the DSLGs with the Hamamatsu SiPMs, and the ARAPUCA are significantly more efficient than the DSLG with SensL SiPMs. Due to this, we simulate not only a parameter space exploring Rayleigh scattering lengths and LAr absorption lengths, but also sets of QE scalings for each of the three detector subsets.

Based on previous works[61][62][63], the two most probable values for the Rayleigh scattering length are 60cm and 90cm, to fully probe the space, we simulate RS lengths of 50 – 120cm in increments

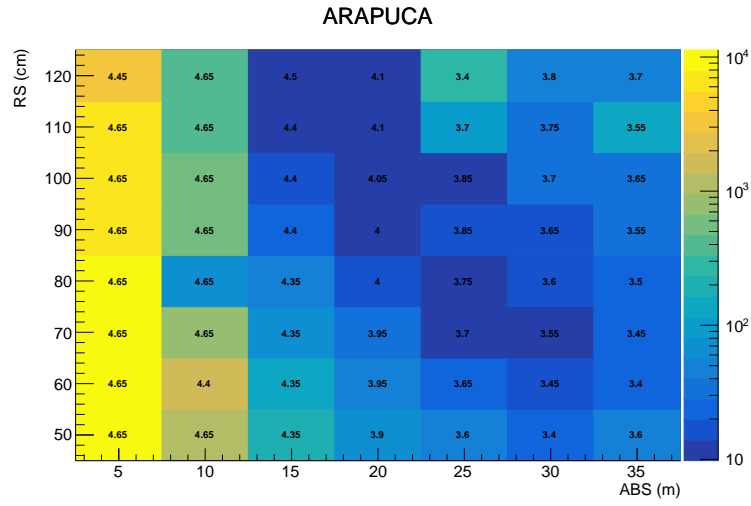
of  $10\text{cm}$ . As the absorption of  $128\text{nm}$  light on pure LAr is unknown, as well as the exact amount and composition of impurities within the detector, we scan a wide range of absorption lengths,  $5 - 35\text{m}$  in increments of  $5\text{m}$ . Finally, from the data, we can see that the DSLGs with MPPCs are approximately twice as efficient as the DSLGs with SensL-C1 SiPMs, and the ARAPUCA is approximately four times as efficient, so we simulate QE scales surrounding  $1\times$ ,  $2\times$ , and  $4\times$  in increments of  $.05\times$ . This creates a large number of monte-carlo simulations to produce, and this computational load is the main limit on the sensitivity of the results. For context, the histograms in figure 4.3 are created from 136,000 tracks. To simulate the entire parameter space, simulation are done of these 136K muons for 7 different absorption lengths, 8 different Rayleigh scattering lengths, and more than 40 QE scales.

### 4.3 Pure LAr Results

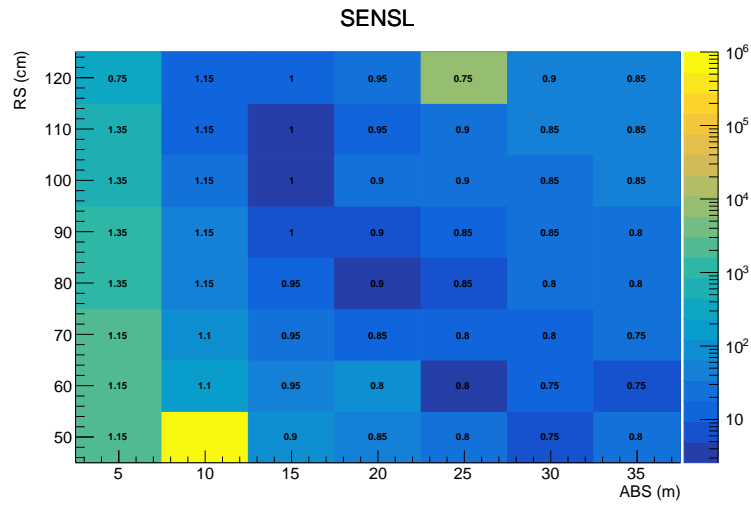
The results of the simulation are compared to the data profiles with a simple ratio. The closer the ratio of monte-carlo to data is to 1, the more accurate our simulation is. For all combinations of RS, absorption, and QE scaling, we find the ratio of the output to the data for all 3 detector types used, and fit that ratio to 1. The resulting  $\chi^2$  of that fit is then our metric of goodness for the simulation.

To visualize the results, and find the best fit values of absorption and Rayleigh scattering, we find the best  $\chi^2$  of all QE scaled results and plot those in a histogram, shown in figure 4.4, where the x-axis is the absorption length of the argon, the y-axis is the Rayleigh scattering length, and the color axis is the best  $\chi^2$  of all QE scalings for that detector type at that value of x and y, with the best QE scaling entered over the bin in text.

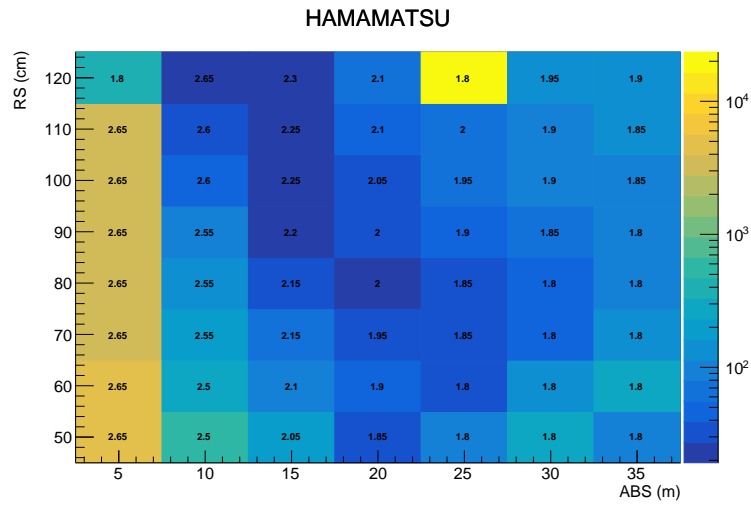
From the plots in figure 4.4, we resolve the values of Rayleigh scattering and absorption length in ProtoDUNE-SP to be those shown in table 4.1. The errors on these measurement are taken to be half of the bin width in each of the parameters. As stated in section 4.2, this analysis was limited by the amount of samples the were reasonably producible, and it can be seen in the plots in 4.4 that a finer binning would produce a better fit to the variables.



(a) ARAPUCA



(b) DSLGs with SensL-C1



(c) DSLG with MPPCs

Figure 4.4: Three dimensional plots that show the values of  $\chi^2$  to 1 of the ratio between monte-carlo and data with the simulated parameters for Rayleigh scattering length, absorption length, and a QE scaling equal to the values on the x-axis, y-axis, and bin text respectively.

	QE	RS(cm)	Abs(m)	$\chi^2/dof$
ARAPUCA	4.0	$90 \pm 5$	$20 \pm 2.5$	10.23
SensL DSLG	1.0	$100 \pm 5$	$15 \pm 2.5$	2.59
MPPC DSLG	2.20	$90 \pm 5$	$15 \pm 2.5$	18.59
Average		$93 \pm 3$	$17 \pm 2$	

Table 4.1: Results of the best fits to quantum efficiency scaling of the PDS modules, Rayleigh scattering lengths on 128nm light, and absorption length of the liquid argon in ProtoDUNE-SP.

It is clear that the simulations involving the DSLGs with Hamamatsu SiPMs show a higher degree of disagreement throughout the entire parameter space. A sample ratio plot is shown in figure 4.5, and a clear bump can be seen in the center of the plot. This disagreement between data and monte-carlo persists throughout all simulated sample sets. The source for this disagreement is left unknown, but work was done to remedy this. First, a cut on the angle of acceptance of the individual detectors was implemented, allowing only light from tracks that pass within a  $\pm 30^\circ$  window to be analyzed. This removes tracks that lie off axis from the PDS, which are more likely to be effected by non-trivial shadowing effects from the wire planes in front of the module face.

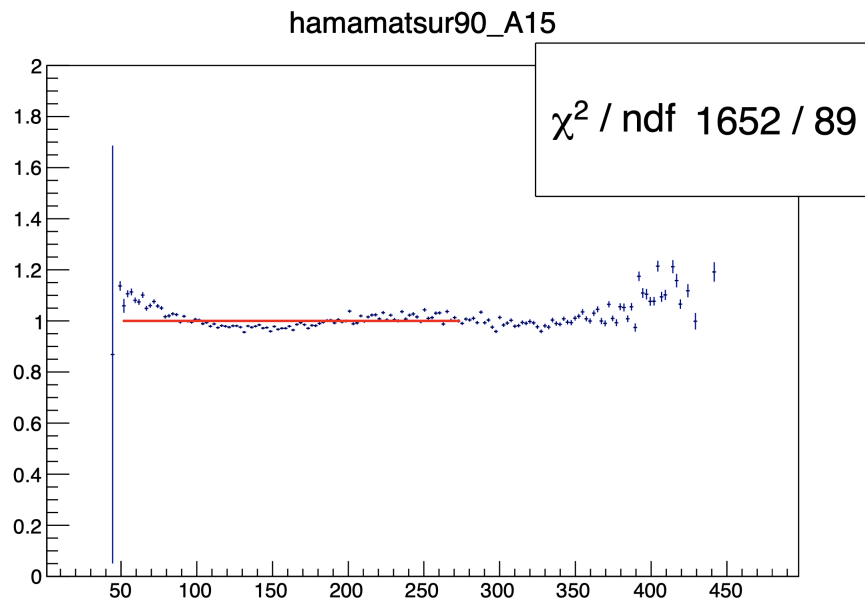


Figure 4.5: An example of the data to MC ratio for the DSLGs with Hamamatsu SiPMs. The multi-nodal shape is clear, showing clear and systematic disagreement between the two samples near 225cm radial distance.

After this did not yield a correction, the analysis was separated into individual APAs, meaning that instead of storing (and plotting) the data from all DSLGs with Hamamatsu SiPMs in a single histogram, we separate those in the first and those in the second APAs for two analyses. These two APAs get illuminated by fundamentally different collections of muons, since these cosmic tracks tend start high at the front face and travel downwards through the detector to the back face, the first APA tends to be exposed to tracks higher in the detector, with the middle APA seeing largely more centralized tracks. Also, as seen in figure ??, the first APA has only three of the modules, while the others are all of different types. This could also lead to biases in the sample. An analysis was done on these separated datasets with and without the angle cut, but this irregularity persisted. This mismodelling is currently thought to be the result of not modeling the simulations using the Hamamatsu waveform, rather using a standardized response from a SensL C-Series SiPM, though this has not been confirmed.

The overall efficiency for the DSLGs with SensL SiPMs was originally calculated in [57], and this calculation was what was implemented in the detector simulation. The agreement between the ProtoDUNE-SP data supports this measurement, and shows the stability of the technology. The QE scaling of the ARAPUCA reported is 4.0, meaning the ARAPUCA has four times the collection efficiency of the DSLGG with SensL SiPMs, which is very similar to the difference in efficiency from the simulations described in section 3.1.

Despite the discrepancies with the Hamamatsu DSLG simulations, we still report good agreement in the parameter space. Table 4.1 shows the resulting best fit values for all three technology combinations. Taking an average of the resulting Rayleigh scattering best fit points, we calculate a Rayleigh scattering length of 128nm light in liquid argon to be  $93 \pm 5\text{cm}$ , where the error reported is half of the bin width. The average returned from propagation through the average is smaller than this, but including this larger error from the bin width corrects for systematic and computational limits. The absorption length is calculated to be  $17 \pm 2.5\text{m}$ , again using half the bin width as the error to compensate for computational limits. Both of these results are in good agreement with expectations.

#### 4.4 Extension to Nitrogen contaminated Liquid Argon

As stated in 2.5, a failure in the recirculation system of ProtoDUNE-SP resulted in a large dump of contaminants and loss of purity in the detector. The recovery of the recirculation system allowed for a majority of the contaminants to be removed to an acceptable level, with Nitrogen being the notable remnant. The PDSP filtration system was not designed to remove large contamination of Nitrogen from the argon, so all operation of the LArTPC after this event will have some N<sub>2</sub> contamination. The amount of remaining N<sub>2</sub> contamination was not initially known, but an analysis of the photon scintillation structure allowed a level of approximately 5.7ppm to be measured[54]. The N<sub>2</sub> in the LArTPC has very little overall effect on the drift charge, so the TPC operation was able to continue unhindered. Nitrogen, however, is a major quencher of the scintillation light in LAr and so the photon yield for runs with N<sub>2</sub> contamination will be heavily reduced. The amount of reduction, as well as additional distance dependent absorption effects can be measured in the PDS using the procedures described above.

A series of runs were taken during November of 2019 for a study of the CRT system and cathode of PDSP. Due to these two items being the main focus of these studies, the distribution of the radial distance of the tracks from the PDS system is vastly different from the studies described above, but this does not change the procedure. After these pseudo-attenuation curves have been constructed for these data runs, shown in figure 4.7, one can take the ratio of the uncontaminated dataset to the contaminated one. The overall scale of this ratio measurement gives the quenching factor of the N<sub>2</sub> in the detector, and any slope of this ratio indicates additional absorption length effects.

Given the different CRT masking and track dispersion throughout this data-taking period, a direct comparison of the two datasets is not possible. The CRT masking for the nitrogen runs was purposefully concentrated on the center (around the CPA) of the detector, giving good statistics for tracks far away from the PDS, but missing any near tracks on the beam left side. To allow for a more uniform distribution of tracks around the CPA, the CRT coincidence timing was also altered. As stated before,

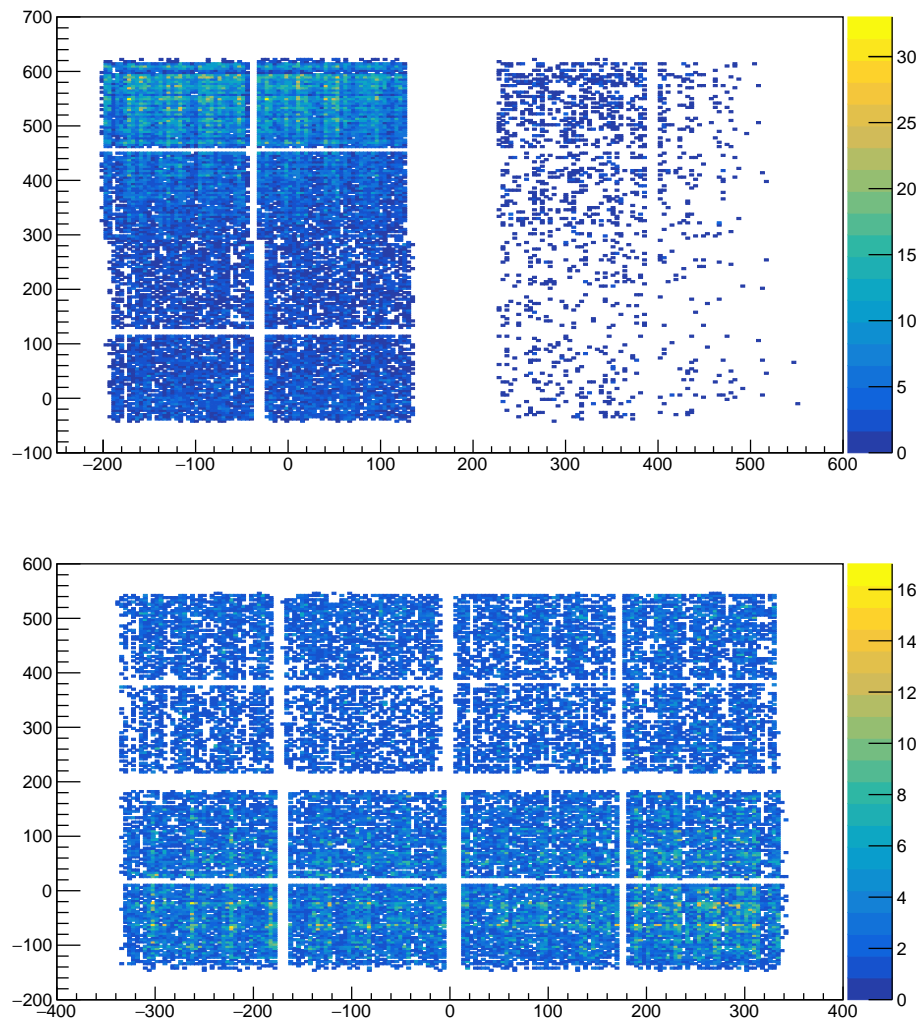


Figure 4.6: Distribution of CRT hits on the front (top) and back (bottom) CRT panels for all events recorded during the nitrogen contaminated data-taking period. One can see a more uniform distribution over the entire detector when compared to the uncontaminated sample.

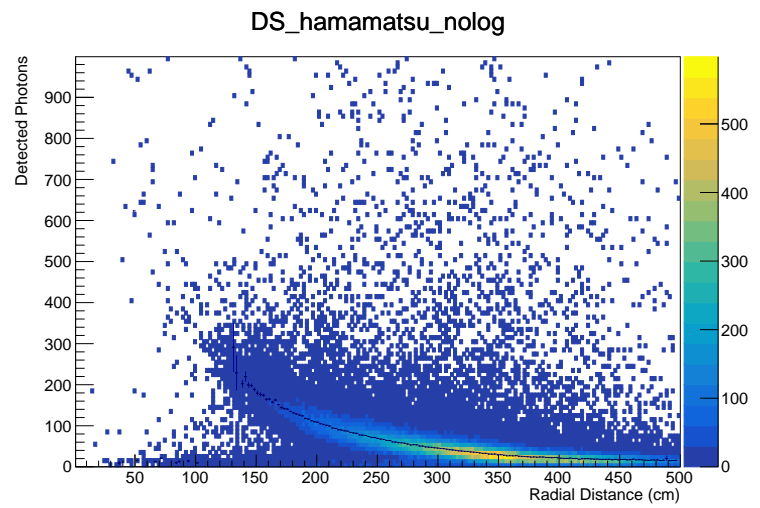
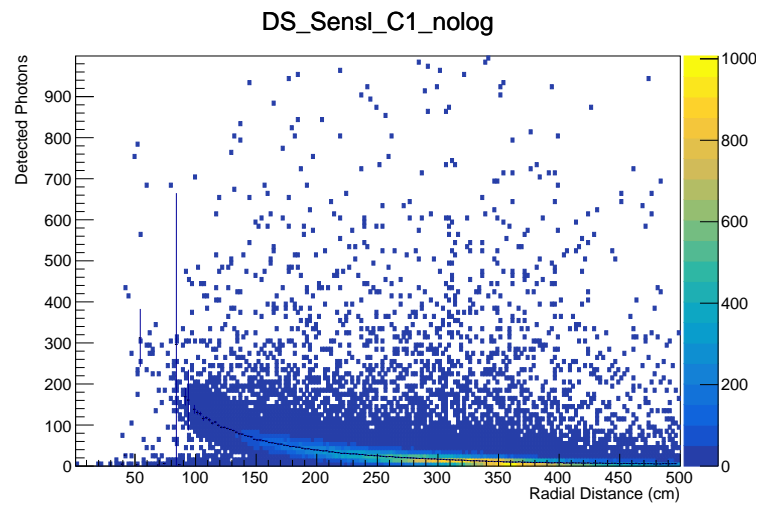
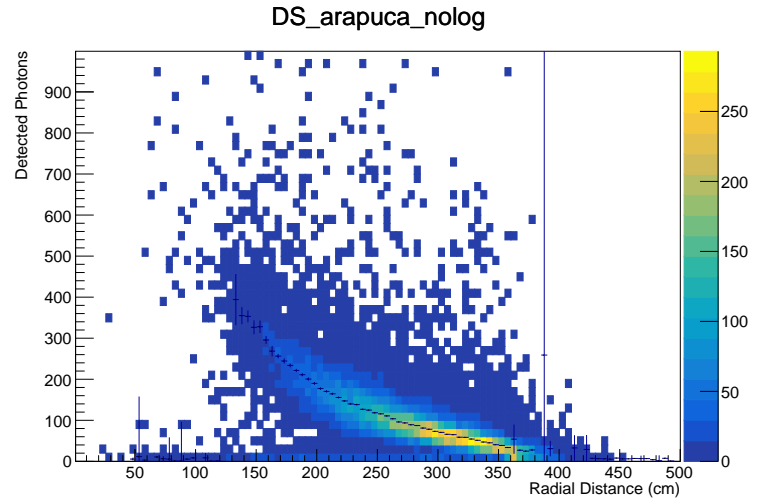


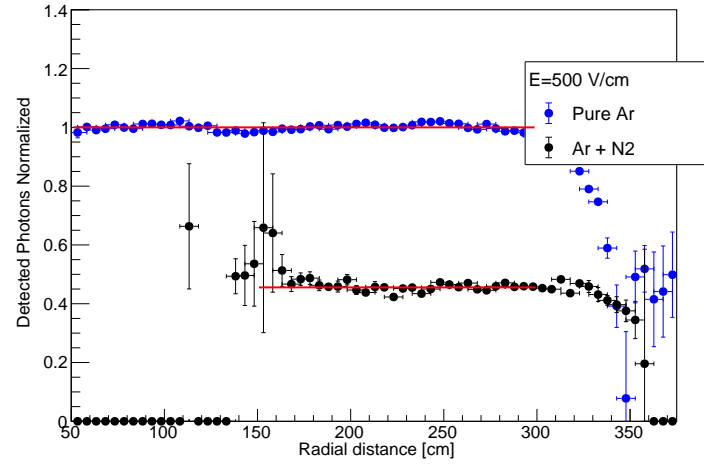
Figure 4.7: The light yield versus radial distance curves for the three detector groupings in nitrogen contaminated LAr.



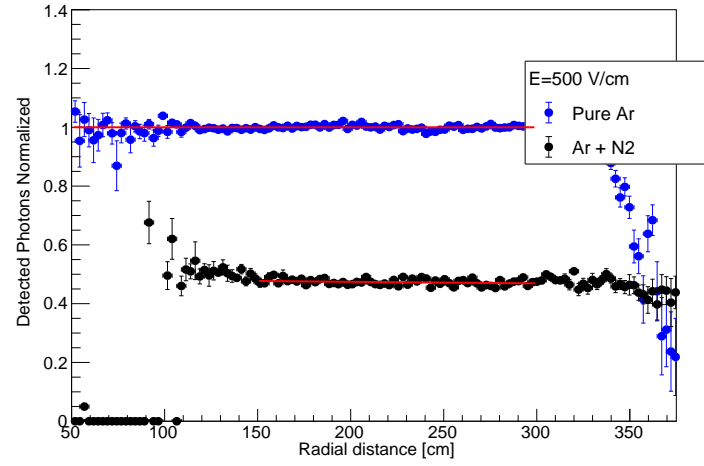
the value of this can greatly affect where tracks are distributed physically in the detector due to the CRT offset. Due to this change, this dataset has fewer tracks in the BL drift volume, only collecting 24,000 tracks. There are no additional changes to the operation of the detector, so what tracks we do collect are available for a comparison to the uncontaminated dataset.

Due to this lack of statistics, a comparison of data to data is difficult. The lower statistics and concentration at higher radial distances necessitate a changing in histogram binning, making a direct ROOT based division impossible. To alleviate this, and to gain as much low radial distance information as possible, a data-to-fit comparison was adopted. The pseudo-attenuation curves in the pure-LAr can be described by a double exponential curve. This model has no physical meaning, per-se, but does model the shape of the curves to high precision. This was initially done for visual purposes, as the fits do a relatively good job of describing the shape of the curves and are visually easier to compare than the data profiles. Though this double exponential model has no physical interpretation, in fact the parameters are largely degenerate, the fit has a very low  $\chi^2$ , and can be used in ratio comparisons. Avoiding any interpretation of the parameters, a comparison of the ratios of data to these fit curves can give insight on the difference in absorption in the pure vs. contaminated LAr datasets.

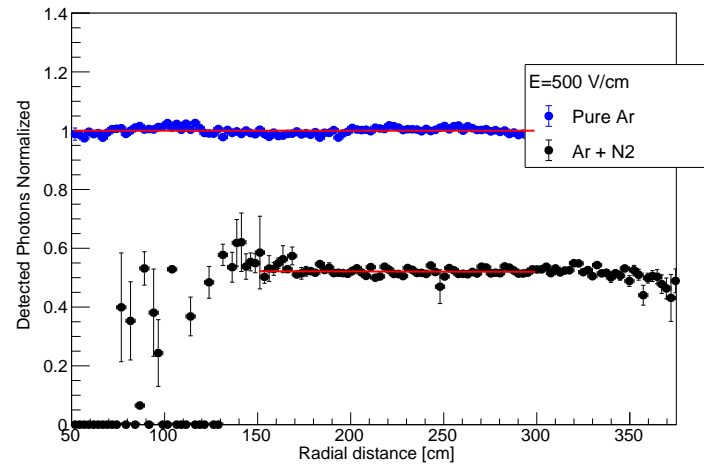
Since the N2 contaminated dataset is  $\mathcal{O}(20\%)$  of the original dataset, and the radial distribution is significantly shifted, the resulting two dimensional plots and profiles are statistics limited at large binning. A smaller number of radial distance bins results in good statistics, and a fit to these can be performed. After fitting the pure and contaminated LAr samples, the ratio of the data to the pure LAr fit is taken. This results in a nearly straight line at 1 for the pure LAr data-to-fit ratio, as expected. There is some long distance disagreement here, but this is well outside of the fit range and is attributed to increased space charge effects at the cathode. The magnitude of the contaminated LAr data-to-fit ratio can be interpreted at the quenching factor due to the nitrogen contamination, shown in figure 4.8 to be .5. Any slope in this ratio is an indicator of additional length-dependent absorption properties of the N2 contamination. The same figure shows that there is no significant slope is this



(a) ARAPUCA



(b) DSLGs with SensL-C1



(c) DSLG with MPPCs

Figure 4.8: Ratios of the pure and nitrogen contaminated data to a fit of the pure LAr data for all 3 categories of detectors discussed.

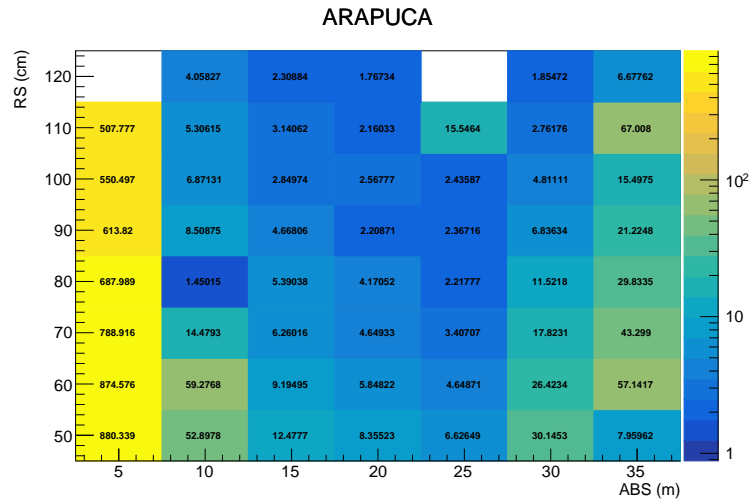
ratio, indicating no additional absorption effects due to the introduction of N<sub>2</sub>.

To further test whether the contamination of nitrogen introduces some absorption effect, a similar procedure to 4.3 was performed. A series of data-to-simulation ratios were taken with the simulated pure LAr samples, but with the data from the nitrogen contaminated pseudo-attenuation curves. Due to the large range of QE simulated, it was possible to perform this analysis for both the Hamamatsu DSLGs and the ARAPUCA. As stated above, the nitrogen results in a quenching of 50%, so QE scales of .4 or lower would be necessary to compare the SensL DSLGs in a similar manner. Since this step of the analysis was largely a cross check for what we have seen in other analysis, we did not simulate further samples. The results three dimensional plots are shown in figure 4.9. It can be seen that the minimums along the absorption axis in these plots aligns relatively well with those in figure 4.4. There is some disagreement overall in the two dimensional space, but given the two very different natures of the data and monte-carlo this should not be taken too heavily into consideration.

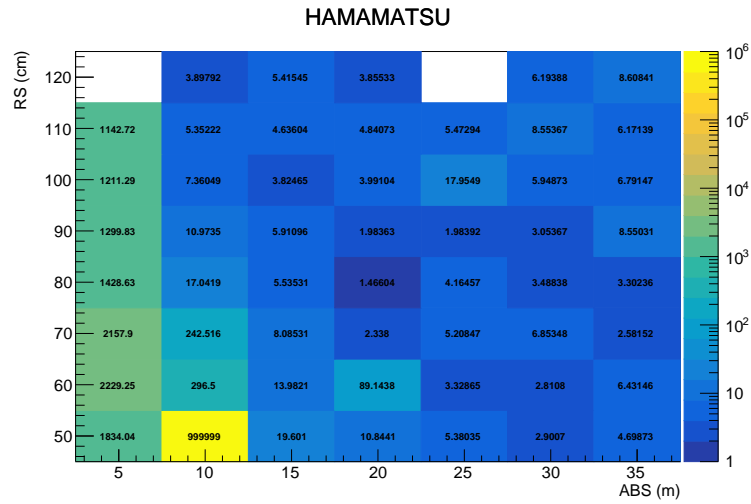
Simulation studies for this dataset were not performed. As there is no indication of changing absorption length, and the quenching causes a uniform 50% loss of light, there is no insight to be gained from undertaking a simulation campaign for the nitrogen contaminated dataset. The quenching can be accounted for by a QE scaling, as shown above, in further studies if necessary.

## 4.5 Extension to Xenon Doped Liquid Argon

After the staged introduction of 18.8ppm of Xenon into ProtoDUNE-SP, a series of CRT triggered data runs were taken to study the effects of the doping on the attenuation length of 175nm light in LAr. The doping process concluded very near the date set for the decommissioning of the detector, so there was a very short window of time available to gather a statistically comparable set of data under these detector conditions. As seen above, the standard configuration of the CRT does not promote a uniform distribution of tracks over all measurements of radial distance from the PDS system, and the use of this configuration would not yield the needed statistics in the short time frame available



(a) ARAPUCA



(b) DSLG with MPPCs

Figure 4.9: Three dimensional plots that show the values of  $\chi^2$  to 1 of the ratio between monte-carlo and nitrogen contaminated data with the simulated parameters for Rayleigh scattering length, absorption length, and a QE scaling equal to the values on the x-axis, y-axis, and bin text respectively.

for data taking. Figure 4.10 shows the location of the CRT activity for the entire data-taking period, emphasizing the selective criteria for triggering.

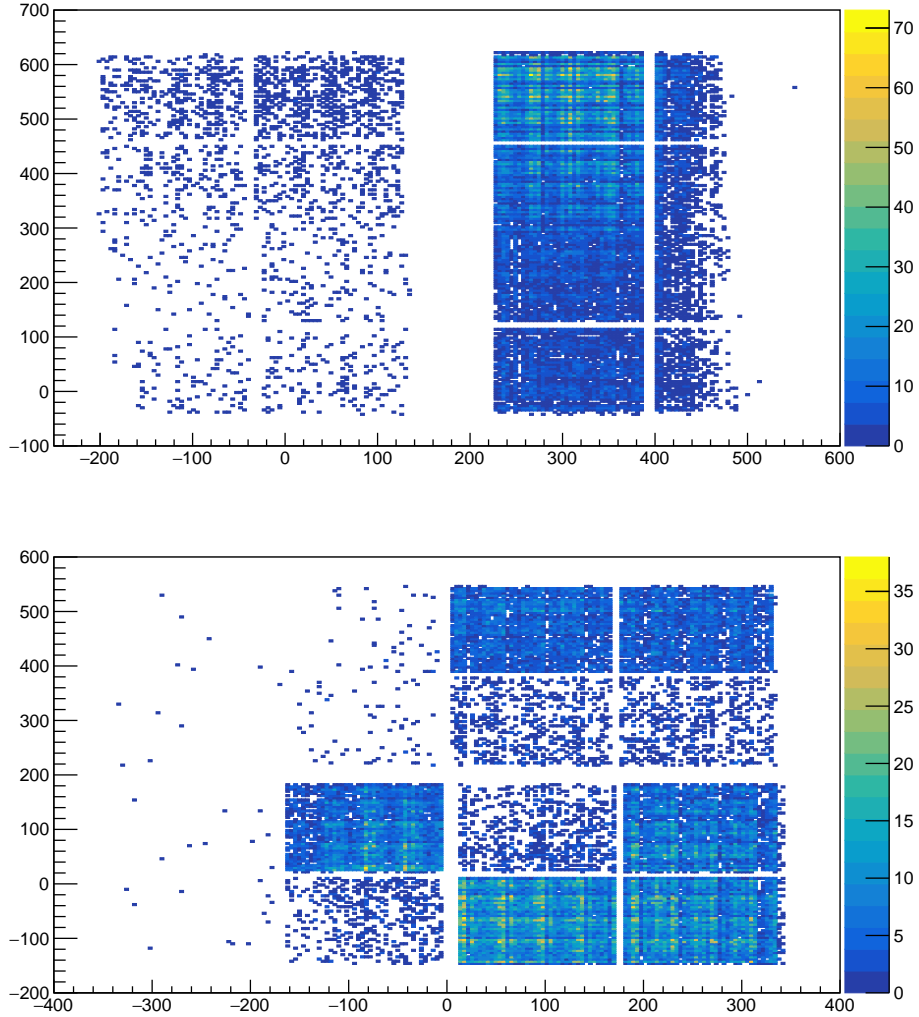


Figure 4.10: Distribution of CRT hits on the front (top) and back (bottom) CRT panels for all events recorded during the xenon-doped data-taking period.

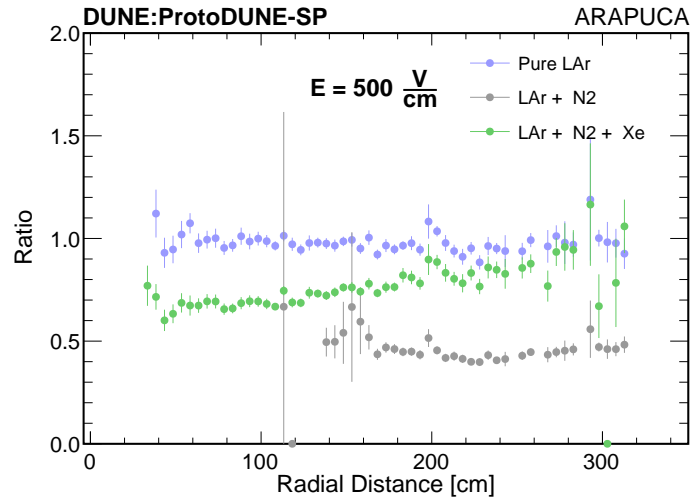
To overcome this time constraint, a series of CRT configurations were created that only triggered the detector on certain CRT panel pairs or sets of pairs, allowing for targeted collection of events within certain distance intervals from the PDS system. Data was taken during a concentrated period from June 16 - July 07 2020, using 11 different trigger masks to collect just over 19 hours of CRT runs. Once this data was taken, and the same analysis described above was completed, the resulting pseudo-attenuation graphs were created. Here, we take the ratio of all of the samples, (Pure Lar, LAr +  $N_2$ ,

LAr +  $N_2$  + Xe), w.r.t. the pure LAr fit. This gives us insight in to how the dopants interact with one another. Figure 4.11 shows these ratios for all three of the technologies focused on in this analysis.

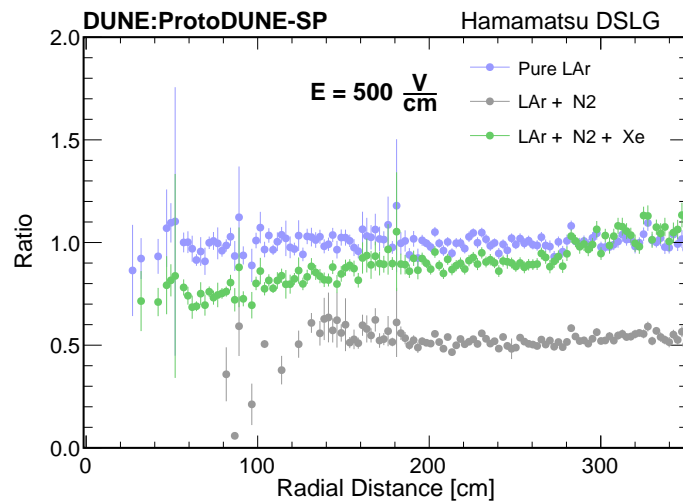
From these plots some key features should be acknowledged. As pointed out in the previous section, the introduction of nitrogen into the bulk medium reduces the light yield by approximately 50%, and does this fairly uniformly over distance. The injection of xenon has recovered nearly all of this quenched light, but does so in a distance dependent way. As expected from previous works, the increased rayleigh scattering length of the xenon and its scintillation light, the light yield is more uniform over distance, resulting in a light yield that is slightly lower than argon very close (due to less light being reflected back into the detector) and higher at long distances, since less light is scattered away on the path to detection. These two points largely support the use of xenon in LArTPCs to increase light uniformity, but also to alleviate the effects of quenching in the event of an accidental injection.

The simulation procedure necessitated the creation of even more light libraries, ranging from 800cm-975cm Rayleigh Scattering. In these libraries, the bulk material remained argon, but the scintillation light was shifted to  $175nm$ , to emulate the xenon doping. The size of the light libraries remained the same, simulating  $100 \times 100 \times 100$  voxels for the entire detector. For the monte-carlo generation, the same procedure was used. The tracks used in the data analysis were used as the input seeds for the MC track generation. It was expected, from previous works [64] that the absorption of the  $175nm$  light would not increase or decrease significantly from that of the  $128nm$ , so only three absorption lengths were simulated,  $(15, 20, 25)m$ . This also helped to reduce the computational overhead. From figure 4.11 we can see that the scale of the light yield is nearly the same for this argon, nitrogen, xenon mixture as for the pure LAr, so the same range of QE scales was used.

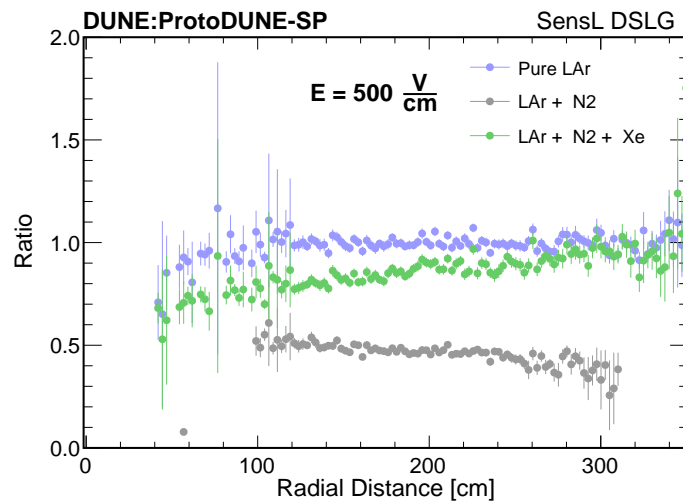
After completion of the simulation, a similar set of analyses were run as for the pure LAr data. The mismodeling of the Hamamatsu response persists, as expected, but a similar set of angle cuts, separations, and further angle cuts were performed in an attempted to alleviate the issue and provide the best agreement possible. The resulting  $\chi^2$  graphs for the xenon doped mixture are less defini-



(a)



(b)



(c)

Figure 4.11: After fitting the pure LAr pseudo-attenuation curve as a baseline, the ratio of the data profiles to this curve were taken and presented here for (a) the ARAPUCA, (b) the DSLGs with SensL SiPMs, and (c) DSLGs with Hamamatsu SiPMs. One can clearly see the quenching due to nitrogen in black, and the subsequent gain from the xenon injection on green.

tive than those presented in figure 4.4, largely due to the disagreement in the Hamamatsu plots. If one takes into consideration the large irregularities in these ratios and interprets these are relatively large errors in the measurements, a local minimum seems to be clear in the plots. Taking the average of the resulting Rayleigh scattering values from the three plots, we calculate a value of  $867 \pm 12.5\text{cm}$ , where the error on this calculation is taken to be half the bin width of the histogram. A slightly longer absorption length best fits the xenon data, with all three technology types preferring 25m absorption. This shows agreement in a slightly longer absorption length for  $175\text{nm}$  light and a Rayleigh Scattering Length of nearly  $900\text{cm}$ , almost nine times that of pure LAr, which agrees with expectation from calculations.

	QE	RS(cm)	Abs(m)	$\chi^2/dof$
ARAPUCA	2.6	$900 \pm 12.5$	$25 \pm 2.5$	4.99
SensL DSLG	1.0	$900 \pm 12.5$	$25 \pm 2.5$	5.7
MPPC DSLG	2.35	$800 \pm 12.5$	$25 \pm 2.5$	10.63
Average		$867 \pm 12.5$	$26 \pm 2.5$	

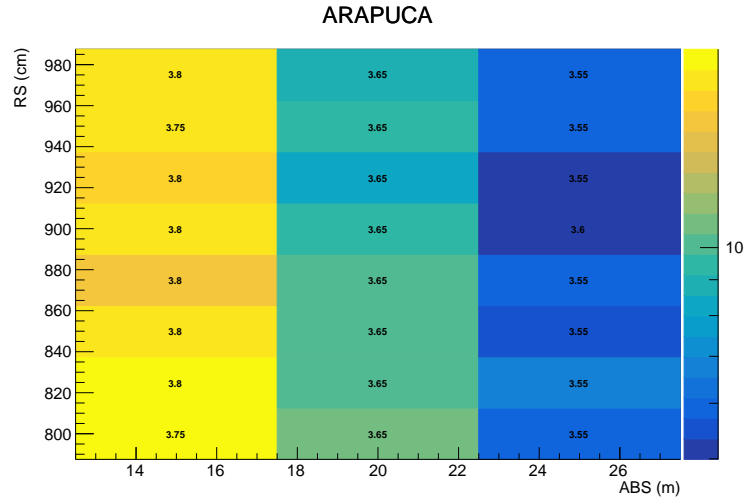
Table 4.2: Results of the best fits to quantum efficiency scaling of the PDS modules, Rayleigh scattering lengths on  $128\text{nm}$  light, and absorption length of the liquid argon in ProtoDUNE-SP.

## 4.6 Field-on and Field-off Comparisons

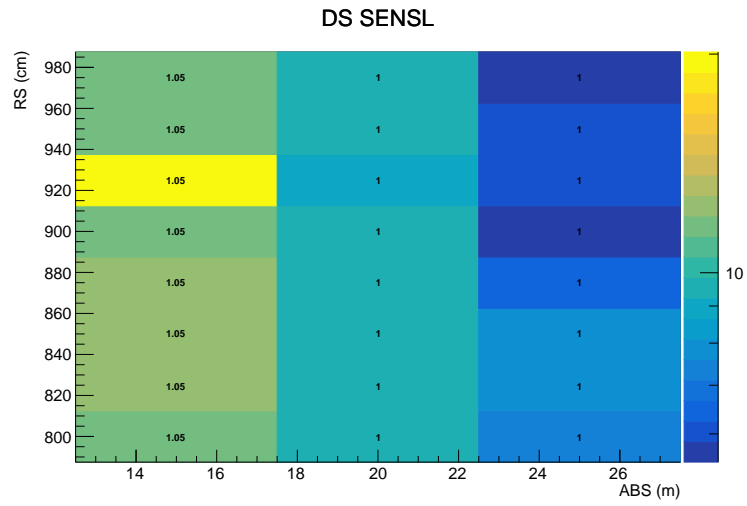
As discussed in section 2.5, the majority of Xenon dopings were done with no electric field present in the TPC. The lead to a track matching algorithm and analysis to be developed specifically to handle this data. To better compare and baseline the effects of the xenon, a similar series of track matched pseudo-attenuation curves and ratios were developed for ProtoDUNE-SP data with no electric field present. This analysis slightly disagreed with some of the conclusions mentioned above, with the main exception being some indication of an increased absorption due to the nitrogen contamination.

The data from these runs was collected and a direct comparison to the field on data was performed. The first step is a direct comparison of the profiles shown in figure 4.13 to those presented throughout this chapter. Figure 4.14 shows the two profiles, redone to have matching binning, and their

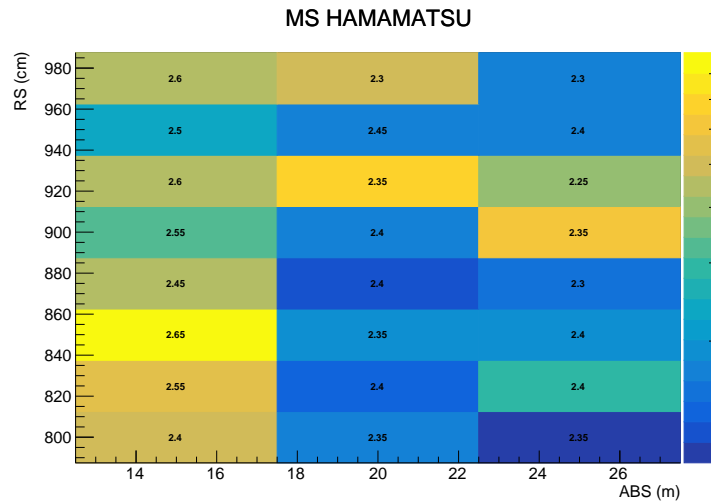




(a) ARAPUCA

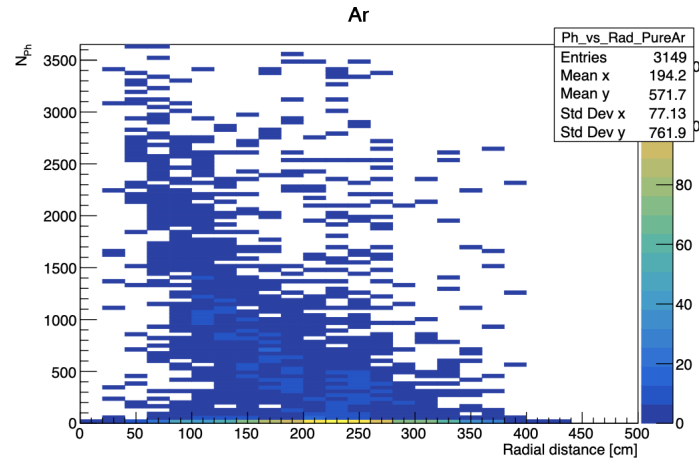


(b) DSLGs with SensL-C1

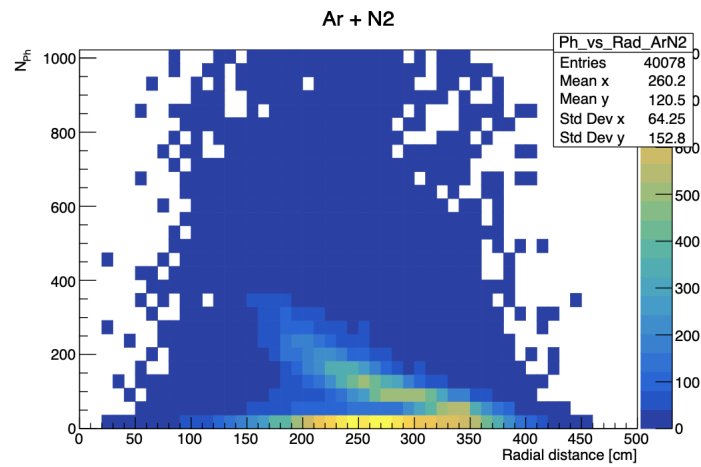


(c) DSLG with MPPCs

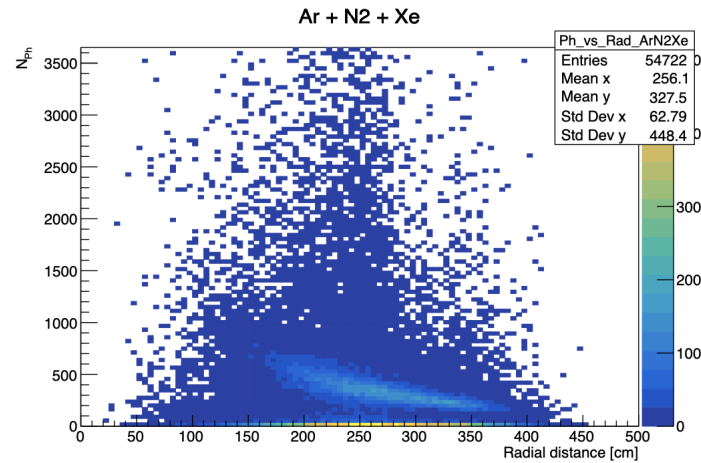
Figure 4.12: Three dimensional plots that show the values of  $\chi^2$  to 1 of the ratio between xenon doped monte-carlo and data with the simulated parameters for Rayleigh scattering length, absorption length, and a QE scaling equal to the values on the x-axis, y-axis, and bin text respectively.



(a)



(b)



(c)

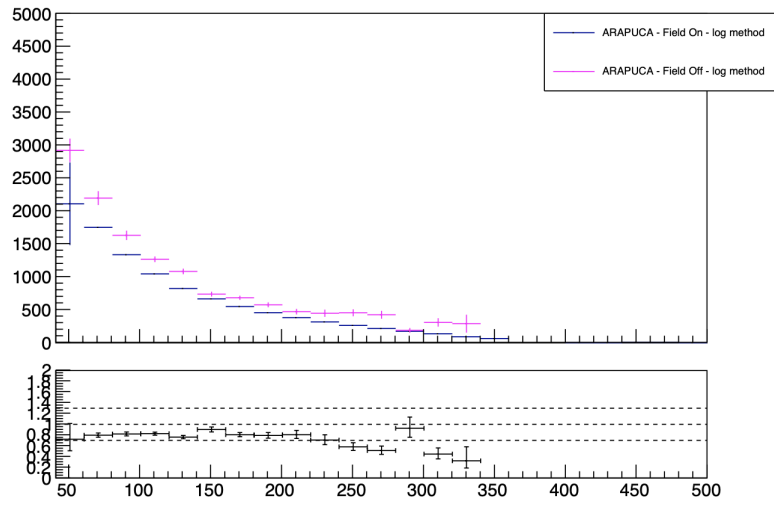
Figure 4.13: Plots of the distribution of detected photons versus radial distance for events where no electric field was present in (a) pure LAr, (b) nitrogen contaminated LAr, and (c) xenon-doped nitrogen contaminated LAr.

respective ratios. A clear trend can be seen indicating that the field off data has a different distance dependent behavior than the field on data, as all of these ratios have some distance dependent slope. These plots also show a good agreement with the results from [37]. In the reference, it can be seen that a field of  $500\text{ V/cm}$  should lead to approximately a light yield reduction of 35%, which aligns well with the results shown here.

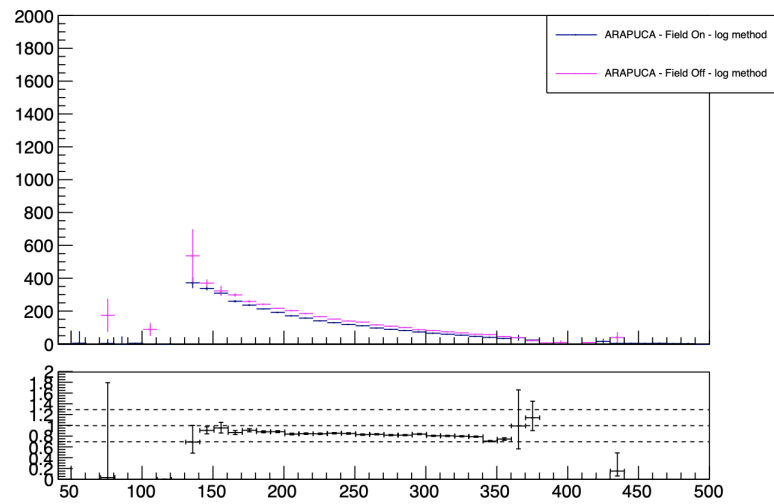
In an effort to alleviate the statistical limitations of the field off data, an analysis method was developed similar to that described in section 4.4, where a fit to the pure LAr dataset was done to be used in a ratio-based comparison method. Built on top of this, due to the clear difference in the radial distance of the collected data, a simultaneous fit method was developed. In this method, both the pure and nitrogen contaminated datasets are fit simultaneously, with the pure dataset being fit with a double exponential and the contaminated dataset being fit with this same exponential time a quenching factor and an additional absorption exponential term. Initial results indicated an additional absorption factor due to nitrogen, with results as shown in figure 4.15.

This analysis was also applied to the field on data that has been collected as described in this chapter. This data was also simultaneously fit in an attempt to locate an absorption factor in agreement with the field off data. The fit to the field on data showed no indications of additional absorption. Further, when a ratio to the field on pure LAr data is performed, as seen in figure 4.16, there is also no indication of an additional absorption length. The fit ranges in both the field on and field off simultaneous fits were varied together, searching for a fit range that showed agreement between both datasets. During this process, it became evident that this double exponential fit was highly dependent on the long range behavior of the pseudo-attenuation curve. This parameters of the fits are otherwise largely correlated due to the short range behavior acting essentially as a single exponential. The lack of long range data in the pure LAr dataset for the field-off data means that there is very little to compare these absorption effects to.

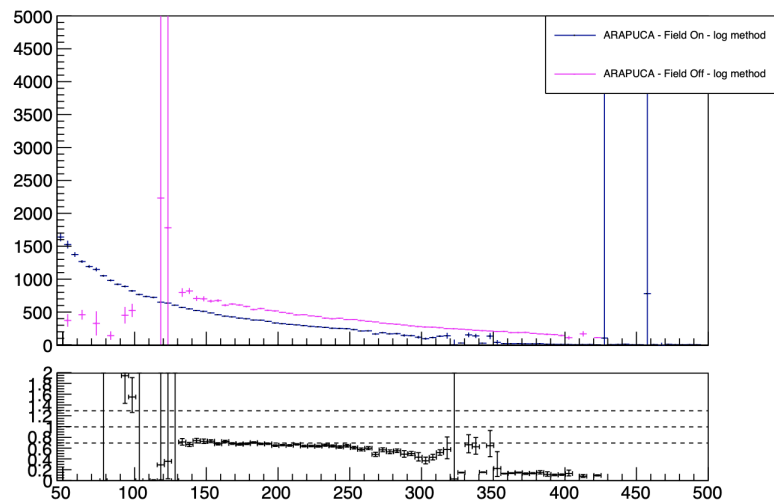
The difference in the two datasets is clear, though the source of this discrepancy is unknown. The introduction of TPC matching means that the field -on data should have a higher purity than the



(a)



(b)



(c)

Figure 4.14: A comparison of the pseudo-attenuation curves with and without an applied electric field for the (a) pure LAr, (b) nitrogen contaminated LAr, and (c) xenon-doped nitrogen contaminated LAr.

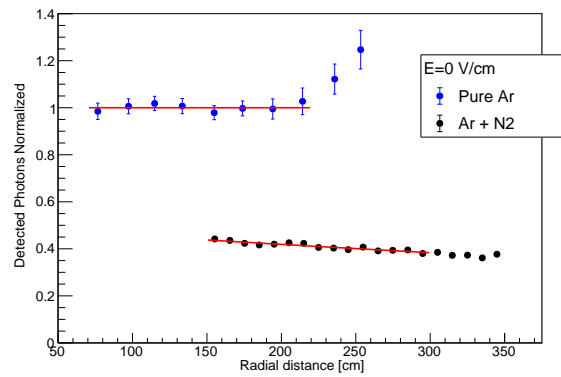


Figure 4.15: The pseudo-attenuation curves for the pure and nitrogen contaminated LAr without an applied electric field taken as a ratio to a fit of the pure LAr curve using a double exponential fit.

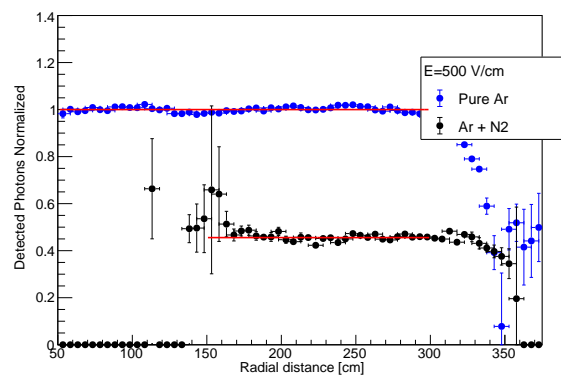


Figure 4.16: The pseudo-attenuation curves for the pure and nitrogen contaminated LAr in the presence of an electric field taken as a ratio to a fit of the pure LAr curve using a double exponential fit.

CRT-only matched dataset. There is some evidence, though, that the differences in the data could be the result of the field, with there being some distance dependent effect on the recombination of the argon atoms and thus a different behavior in the absence of the field.

## Chapter 5

# Effects of Xenon Doping on Proton Decay Observations

In addition to the insights into neutrino oscillations, the DUNE detector is also designed to be capable of setting new limits on the proton lifetime. The energy resolutions in LArTPCs make them particularly capable of measuring the proton decay (PDK) channel  $p \rightarrow K\bar{\nu}$ . The kaon in this decay is very low energy, of order  $500\text{MeV}$ , which is below the threshold for other types of neutrino detectors, such as water Cherenkov detectors, to observe. The large volume of the DUNE detectors and the expected operational lifetime of more than a decade paired with the fine energy and spatial resolutions of the LArTPC technology, DUNE is situated to place a world-leading lifetime limit on this decay channel.

An analysis has been completed, setting the expected limit that DUNE will set in this channel at  $6.6 \times 10^{33}$  years [65]. The analysis was performed using TPC based information, such as reconstructed track characteristics and energy deposited, in a pure liquid argon medium. As discussed in the previous section, the addition of xenon into the DUNE detectors will result in an increased uniformity of light distribution and improved calorimetric abilities using the PDS. The addition of xenon is not expected to have a large impact of the charge collection and reconstruction of the TPC, which has been shown in the ProtoDUNE-SP detector as discussed in section 2.5. This chapter

will discuss the impacts of the inclusion of the light signals and xenon doping on this proton decay sensitivity.

## 5.1 Event Generation

All proton decay events in this analysis are generated using the GENIE Neutrino Monte-Carlo generator. For this analysis, the protons are simulated as bound nucleons. The decaying nucleon has an assigned Fermi momentum and escape energy, where the entire process is modeled using a relativistic Fermi gas model with an incorporated Bodek-Richie tail. This Bodek-Richie models the short range nucleon interactions that would occur in a bound nucleus. The propagation of the decay products through the nucleus are also handled by the GENIE generator, using an intranuclear cascade generator.

Within this model, the kaon is allowed to scatter within the detector, affecting the expected momentum and energy of the kaon after escaping the nucleus. Directly after the proton decay, the kaon moves freely through the nucleus. After some time, it is possible for the kaon to interact with another nucleon with a probability that depends on the mean-free-path ( $\lambda$ ) and the nuclear density ( $\rho$ )

$$\sigma = \frac{1}{\lambda(E, r)\rho(r)} \quad (5.1)$$

where the interaction probability is based on the cross sections of reactions for the free nucleons. The model chosen for this analysis is the **hA** model[66], which is an empirical data-driven model of interactions which employs the total cross sections for each nuclear process in the decision making (as opposed to calculating all reactions). Subsequent passage through the detector medium and the detector response and reconstruction is done using GEANT4 and the standard DUNE reconstruction software suite.



## 5.2 Addition of a PDS-based $t_0$

The DUNE PDK analysis was done using a machine learning package built into ROOT called TMVA. TMVA integrates into ROOT and allows the analyzer to easily import a TTree and perform a machine learning (ML) based analysis and output another ROOT file for further analysis or ingestion. This scheme integrates well with the rest of the High Energy Physics analysis ecosystem, and this TMVA is typically considered the standard package for ML-based physics analyses. To perform the PDK sensitivity study described in [65], a series of TPC track based variables were fed into a boosted decision tree (BDT) and the output model's accuracy was used to determine the detector's sensitivities. In addition to these track based quantities, the event displays of these events were also characterized using a convolutional neural network (CNN), which using the event display instead of the track variables to distinguish and score these PDK events. The combination of the event-display based CNN score and the reconstructed track characteristics produces a well trained, accurate model for PDK identification, distinguishing true PDK events from the background signals from atmospheric neutrinos and radiological activity.

The BDT for this analysis was trained in monte-carlo PDK and background atmospheric neutrino events. The standard reconstruction package can use a variety of techniques and algorithms to reconstruct events. The standard in LArTPC has quickly become the Pandora pattern recognition software[67], but other algorithms also exist and have been successful. To date, Pandora has not been optimized or proven for these very low energy events, as it has largely been developed for accelerator based neutrino experiments. This led to the use of a different algorithm in the sensitivity studies done previously. However, all of these reconstruction algorithms assume a perfect  $t_0$  measurement.

When a PDK event is simulated, the monte-carlo event starts at a time of 0, beginning all activity at the time of the event occurrence. This leads to the reconstruction software to use that time of event initiation as the true time of event for the reconstruction, meaning that all time-based mea-

measurements use  $t_0 = 0$ . However, these event generators are typically designed such that the true event time is distributed around 0, giving some distribution of decay times to better simulate a real world situation. This leads to a slight inaccuracy in most event reconstruction, though this feature has not been well studied to this point. The design of the DUNE detector makes use of the PDS for event timing, as well as a well known beam trigger. The use of the PDS as a trigger is often assumed to be a simple addition, because the timing resolution of the PDS is on the order of nano-seconds and the light signal is shown to be efficiently collected, but the correction to this perfect  $t_0$  has not been studied in these PDK sensitivities.

After studying the optical flash reconstruction in the DUNE software suite<sup>??</sup>, the timing of these flashes was then implemented into the Pandora reconstruction process. After the creation of the wire based hits, during the step where Pandora uses the raw wire hit information to create a three-dimensional space-point, a flash-based offset was introduced, simulating the effects of a real-world PDS-based  $t_0$  measurement. The use of the Pandora suite for this analysis was based on the push for Pandora to be the baseline reconstruction suite for the DUNE physics program. To examine how flash-based  $t_0$  measurement effects the PDK sensitivities, the ML based analysis was recreated and these newly timed events were fed into the model and the identification accuracy was analyzed.

In this new iteration of the study, some variables were omitted due to changes in the software or ease of computation. First, the CNN score was omitted. During the time since the original study was performed, many changes have been implemented in the reconstruction software and the use of the old CNN would be inaccurate. The computational time to simulate enough samples and properly train a new CNN was decided to not be beneficial to the study, as the gains from the CNN were deemed not be significant to test this feature. In addition, the energy measurement quantities used in the initial study have been removed from the reconstruction chain in lieu of improved features, and so these are not used. This leaves fewer variables to study and leads to less accurate models being trained from these events, but this study is only intended to test the relative accuracy of the model between features, so the total accuracy of the model is less important. A list of the input

variables and their descriptions is listed below.

- Number of tracks: The total number of tracks in the detector during the event.
- Number of showers: The total number of particle showers in the detector during the event.
- Number of vertices: The total number of independent vertices, or track or shower start/interaction points, in the detector during the event.
- Particle Identification (PIDA) of the longest track: The PIDA of the longest track in the event, where PIDA is calculated as the mean over the last thirty centimeters of the track of the function  $PIDA = (dE/dX)_i R_i^{42}$ .
- PIDA of the shortest track: The PIDA of the shortest track in the event.
- Length of the longest track.
- Length of the shortest track.
- Momentum of the longest track.
- Fraction of energy in the track that is EM-like: The tracking algorithm examines the energy deposited in the track and characterizes it as EM or track-like (i.e. EM or hadronic).
- Number of optical flashes in the event: This is the total number of flashes that occur throughout the entire readout time period.
- PE in largest flash: The sum of photons collected during the largest optical flash in the event.

PDK events were simulated and reconstructed using the production Pandora reconstruction and the flash-matched reconstruction. Events that occurred outside of the interior section of the detector or that had components that were not contained were cut from the analysis, leading to a sample of PDK and atmospheric neutrinos events occurring near the center of the DUNE detector. Events where the longest or shortest track was longer than 100cm in length were also omitted, removing

events that produced a muon of too high of energy. The variables listed above were collected and fed into a series of ML algorithms and the accuracy was recored and compared. Also analyzed were the feature importances, a measure of how important the individual variables was in the model's decisions, which give insight into which particular variables were impacting the model. Using these metrics allows one to observe how the changing features affect the sensitivity of the DUNE detector.

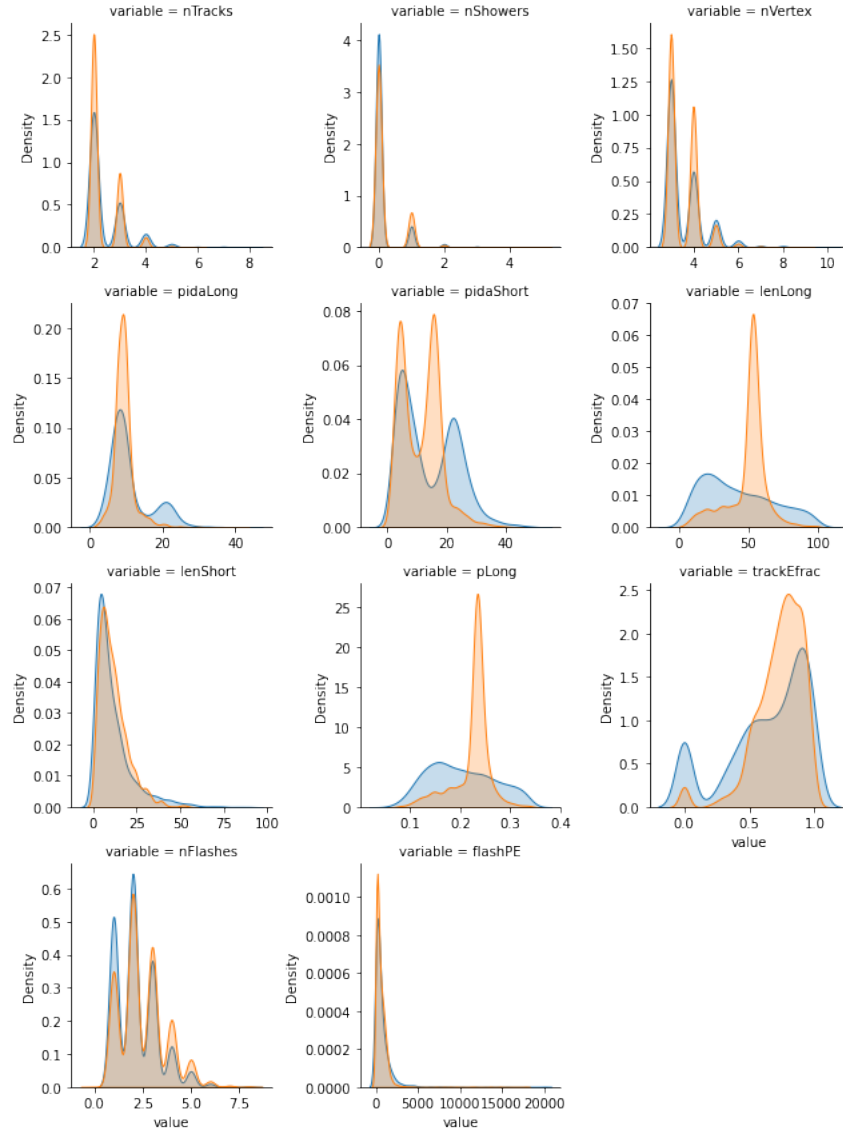


Figure 5.1: Input variables for the signal and background for production timed pure LAr events.

Though TMVA was used previously, the limited array of ML models integrated with this software make the differentiation of the impacts from these new features difficult. To alleviate this and to

gain more insight, this analysis was performed using the Python based package SciKit-Learn. This addition to the python coding language makes ML analyses intuitive, allowing for the data to be input from a labelled comma separate file and giving the user access to a variety of ML models. In this analysis, the performance of 7 different models were compared, in an attempt to gain maximum insight from the fairly small sample of events. The models used for this analysis are listed and described here:

- **Decision Tree:** A decision tree is a a method of supervised learning. The tree is trained by making a decision, in this case a cut on a variable, and then checking to see how well the model scores after this decision is made. After this, the classifier makes a second decision, and then a third, etc... until a flow chart-like tree of decisions has been made that optimizes the models accuracy.
- **Boosted Decision Tree:** An extension on the decision tree, a boosted decision tree combines the power of multiple, weaker decision trees to create a stronger classifier. Once a decision is made and a tree has been created, the accuracy is tested and assigned a weight, which is relative to the tree's accuracy. The final model then uses a weighted sum of the trees to make decisions, focusing on mis-classified data more heavily in the next iteration.
- **Random Forest:** The random forest is yet another extension of the basic decision tree. In this model, a decision tree is trained using a random ensemble of the training data that is sampled with replacement. This allows for a more random training sample to be used at this particular point. Further, when a node (decision) is being created for the tree, the cut is optimized either by the input features of the training ensemble, or a completely random sample. These two sources of random behavior decrease the variance in the estimator, providing a more robust classifier.
- **Support Vector Machine:** This classifier learns by creating a hyperplane in the multidimensional parameter space that the variables live in, and calculates the distance from this plane

to the nearest point of any classification. This plane placement is then shifted to allow for maximal distance of the plane from all points in the parameter space. In highly complex parameter spaces, where the points are not linearly separable, the machine maps the points onto a higher dimensional space using a kernel function, and optimizes the hyperplanes in this larger dimensional space. This classifier is largely not suited for this application, but was implemented for comparison.

- **Neural Network:** A neural network is modeled after the human brain, as the name implies. This model analyzes the input features and maps these features to a layer of neurons, which weights the input variables together to form an output function from this node. These outputs are then fed into another layer of neurons and the process repeats for a designated number of layers. These layers and their weights are optimized as training data is viewed, creating a network of feature - output relations that define the classifier model. This classifier could be quite excellent in this application, but this analysis did no tuning to maximize performance, as simply a comparison between samples after chagnes were made was the final goal.
- **Gaussian Naive Bayes:** This model uses Bayes's theorem to make decisions, looking at all input features as independent of one another when making a decision. For all of the possible outcomes given the input features, the Bayes model creates a probability density function defining the likely hood of classification given the inputs. The classifier makes decisions similar to a decision tree, but instead of continuing this ad nauseam, the classier constructs a decision based in the weighted probability densities that arise from the model.

The models were trained on events that were reconstructed using the standard and flash-matched reconstructed algorithms. The accuracies, the number of correct classifications, of the various models for the two samples is given in figure 5.3. Here, it can be seen that a more accurate flash-based  $t_0$  measurement has minimal effect on the accuracy of the model. This shows that the quoted sensitivity is not expected to change in the DUNE detector that will use the PDS to trigger these candidate events. The input samples for the production timing are shown in figure 5.1, while all other collec-

tions of input variables are included at the end of the document, for brevity. Figure ?? shows the score distribution from the Boosted Tree classifier on signal and background samples for both the training and testing datasets.

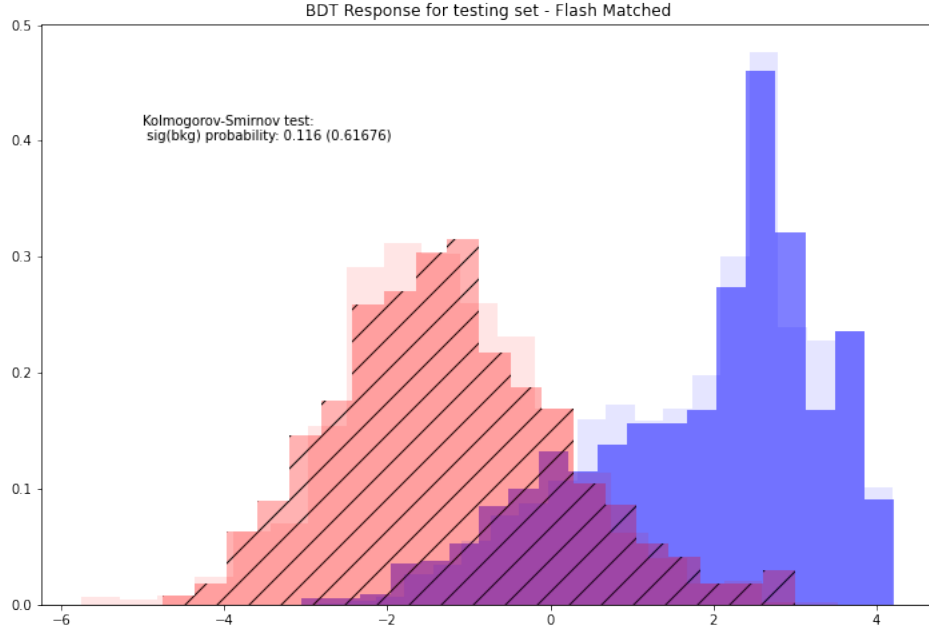


Figure 5.2: Distribution of the classifier score for the signal (blue) and background (red) sample for the training (light) and testing (dark) datasets.

### 5.3 Effects of Xenon Doping

The injection of Xenon into the detector medium has been shown to increase the light yield, in chapter 4, particularly at long distances from the PDS, and not have any clear effect on the charge yield in the TPC. This points to the cost being the only downside of xenon injection, but no work has been done to study the effects injection on some non-accelerator based studies, such as the PDK sensitivity. Here, the effects on the PDK sensitivity in the presence of Xenon are studied. 12,000 ( 4,200 after cuts) proton decay events and 22,000 ( 1,600 after cuts) atmospheric neutrino events were simulated using the same GENIE models as before, where a light-library that included xenon

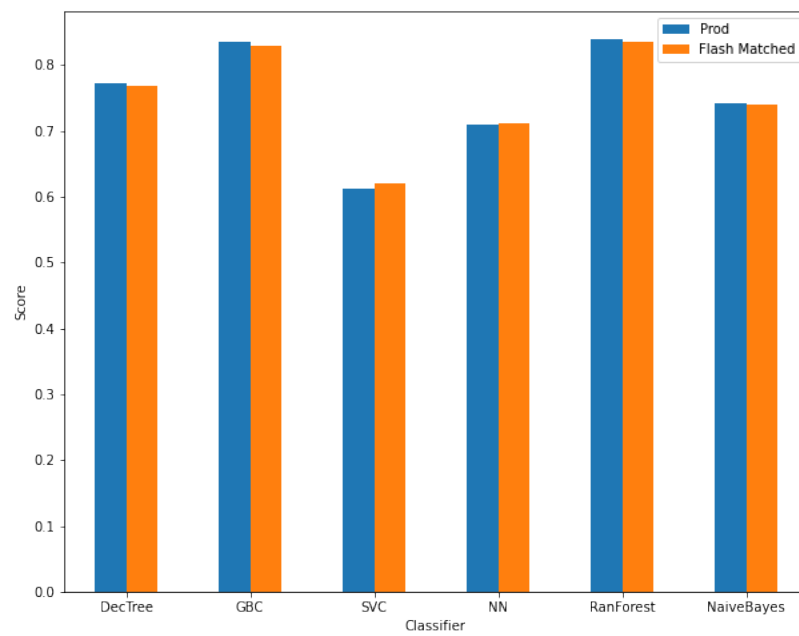


Figure 5.3: A comparison of how the accuracy of the classifiers changes when a flash matched  $t_0$  is introduced.



was introduced at the GEANT4 stage and propagated throughout the reconstruction process as described above. No other changes were made to the software, allowing the effects of the xenon injection on the measurement to be directly measured. The same ML models described above were trained on these 32,000 (5,800) with both the standard  $t_0 = 0$  and flash-matched  $t_0$  methods and the accuracies are compared to the pure LAr samples. This comparison can be seen in figure 5.4. The difference in the feature importances between the flash matched samples in the xenon for the decision tree-based classifiers given in figure 5.5.

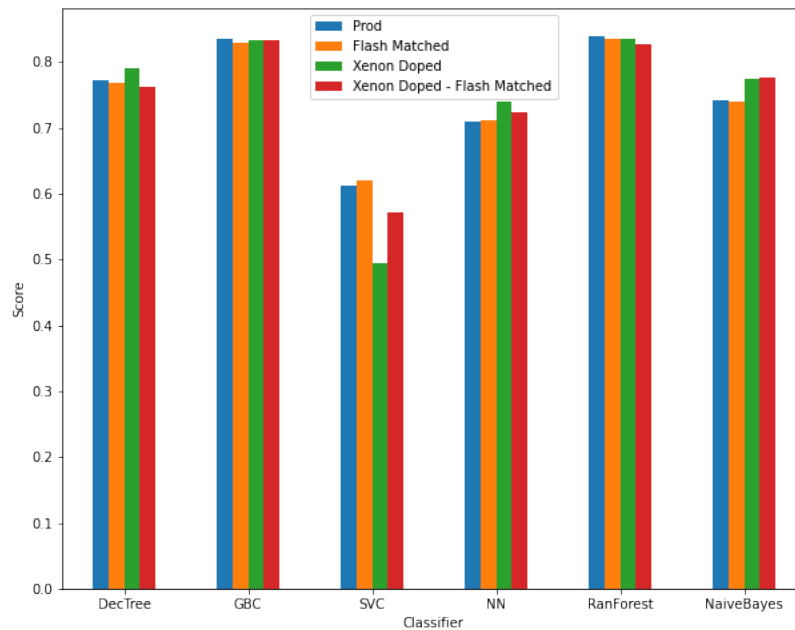


Figure 5.4: The accuracy of the four separate samples for the 6 classifiers profiled in this work.

From figure 5.4, it seems that the addition of xenon has a minimal effect on the performance of the majority of classifiers over the nominal LAr mixture. In the case of flash matched  $t_0$ , the pure LAr sample greatly outperforms all others for the decision tree and random forest classifiers, while the flash-matched xenon sample appears to perform relatively consistently over all of the classifiers. As anticipated, the SVC and neural networks underperform in this application. The neural network could be optimized via hyper-parameter tuning to improve overall performance, but the trend of

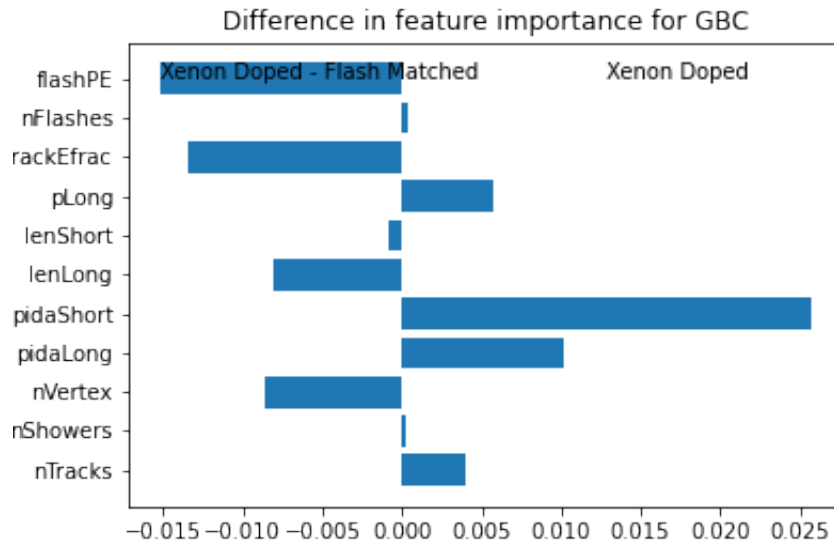


Figure 5.5: Difference in the feature importances between the xenon doped nominal matching and the xenon-doped flash matched samples.

the results presents stability in sensitivity with xenon injections. The SVC is largely just not a useful classifier for this use case, as the very large dimensionality of the parameter space makes the algorithm challenging to optimize. As anticipated, the "simpler" algorithms perform rather well, having the ability to slice in the parameter space in a slightly more arbitrary way.

Figure 5.6 gives the distributions of the classifier score for the boosted tree for the training and testing datasets in the case of xenon doping. The distribution shows more spread in the score of the background in the case of xenon. There are more samples that are better classified as background, while also including samples which are slightly more mis-identified as signal events. As the total accuracy does not change this does not seem to have a large effect on the analysis, but does indicate a difference with the injection of xenon.

Important to note at this point is that the LAr based study was completed with production monte-carlo samples. These events were generated and reconstructed in August of 2020 using the most up-to-date version of the reconstruction software at that time. The xenon-doped samples were created in May of 2022 using a more current version of the software. This was largely due to the lack of

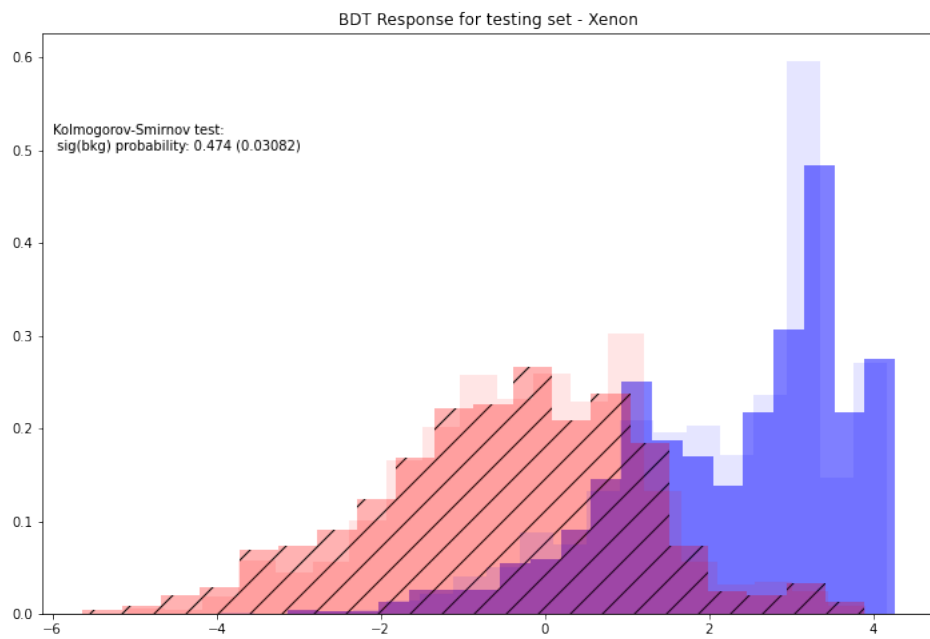


Figure 5.6: Distribution of the classifier score for the signal (blue) and background (red) sample for the training (light) and testing (dark) datasets for the xenon doped dataset.

backwards compatibility of the software and the analysis at the time. This shift to a newer version of the reconstruction could be the root cause of these non-xenon related shifts. As seen in figure 5.7, the PIDA of the longest track in the signal sample seems to have a systematic shift between the old and new samples. Also present is a small sample of pure LAr events generated in the same environment as the Xenon events. It can be seen that the older version calculation of this variable seems to deviate from the newer version, which agrees regardless of doping status.

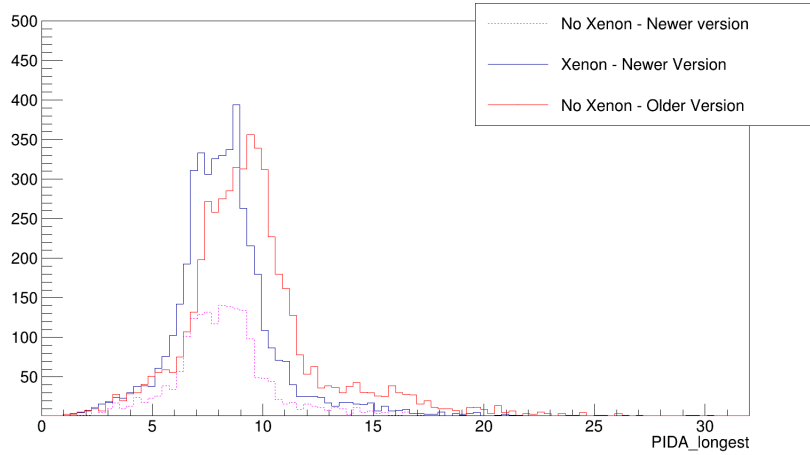


Figure 5.7: The PIDA of the longest track for three samples: The xenon-doped PDK samples used in this analysis (blue), the nominal PDK events used in this analysis (red), and a small sample generated in the environment of (blue), but with no xenon (magenta-dashed).

There is some shift in the relative importance of the PIDA feature in the classification, as seen in figure 5.5, so there is some chance this versioning issue is propagating through the classification. However, if one examines the input variable by eye, this shift in PIDA is not distinguishable, especially when comparing the signal and background events. With this, the results are presented here with confidence despite this abnormality. Ideally, a new sample of background and signal events in pure LAr would be generated and compared to the xenon samples in an attempt to alleviate this issue and better test the compatibility of xenon doping with the PDK search. This was not performed for this task due to time constraints, and the conclusions presented here are that improved flash matching does not affect our sensitivity, and that the addition of xenon seems to not affect said sensitivity.

The addition of xenon also has the possibility to increase the size of the fiducial volume selected for this analysis. The increased uniformity of the light yield can aid in energy and particle reconstruction closer to the edges of the detector, where backgrounds are more likely to penetrate. This increased uniformity would allow the light and timing signals of events farther out to be taken into consideration for the classifier, as they are here, and would possibly allow for increased sensitivity in the detector. This analysis was not included for this work, but is a logical continuation that the author recommends as an exercise to the reader.

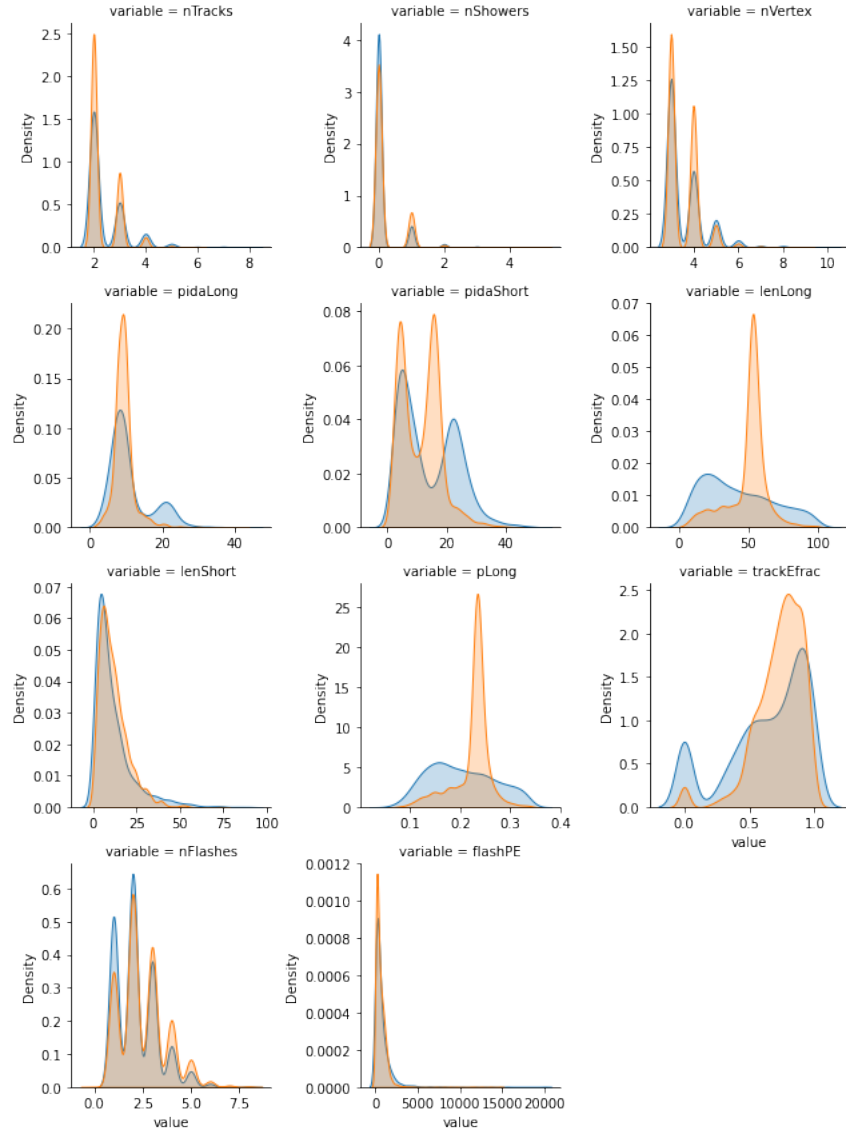


Figure 5.8: Input variables for the signal and background for flash matched pure LAr events.

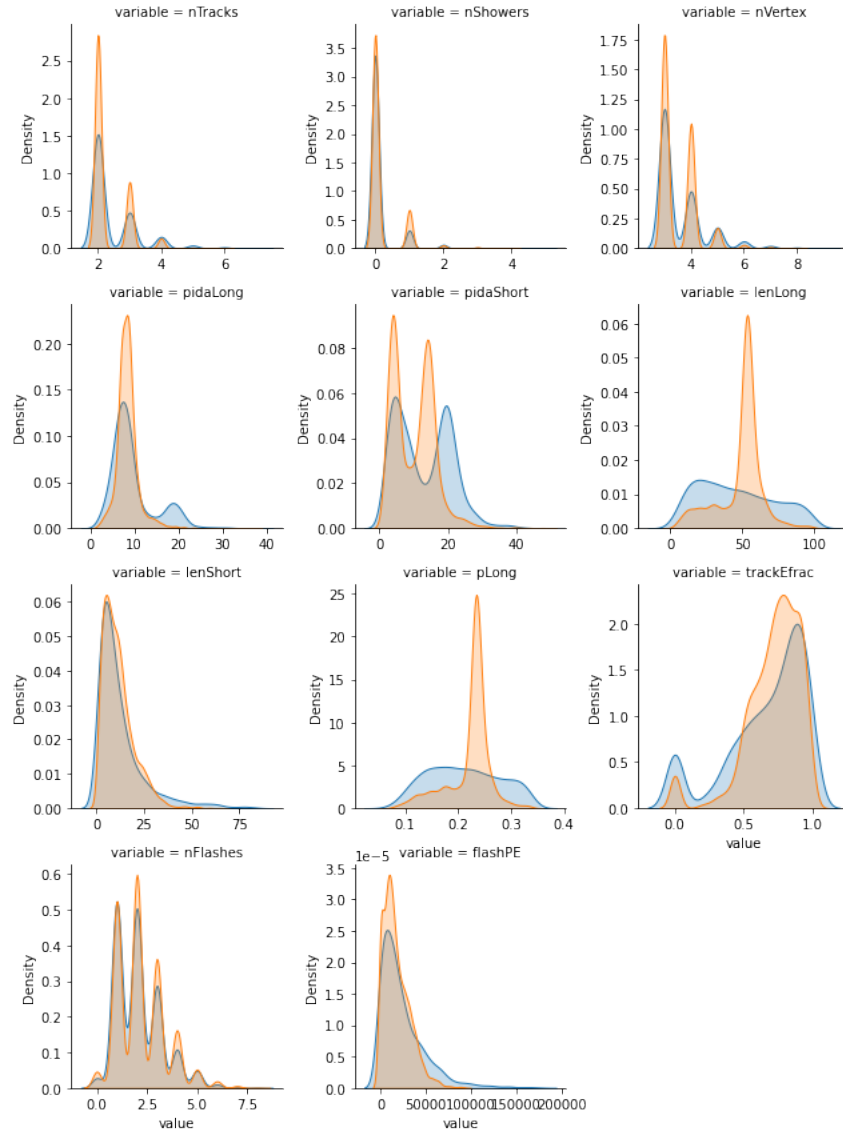


Figure 5.9: Input variables for the signal and background for production timed xenon-doped events.

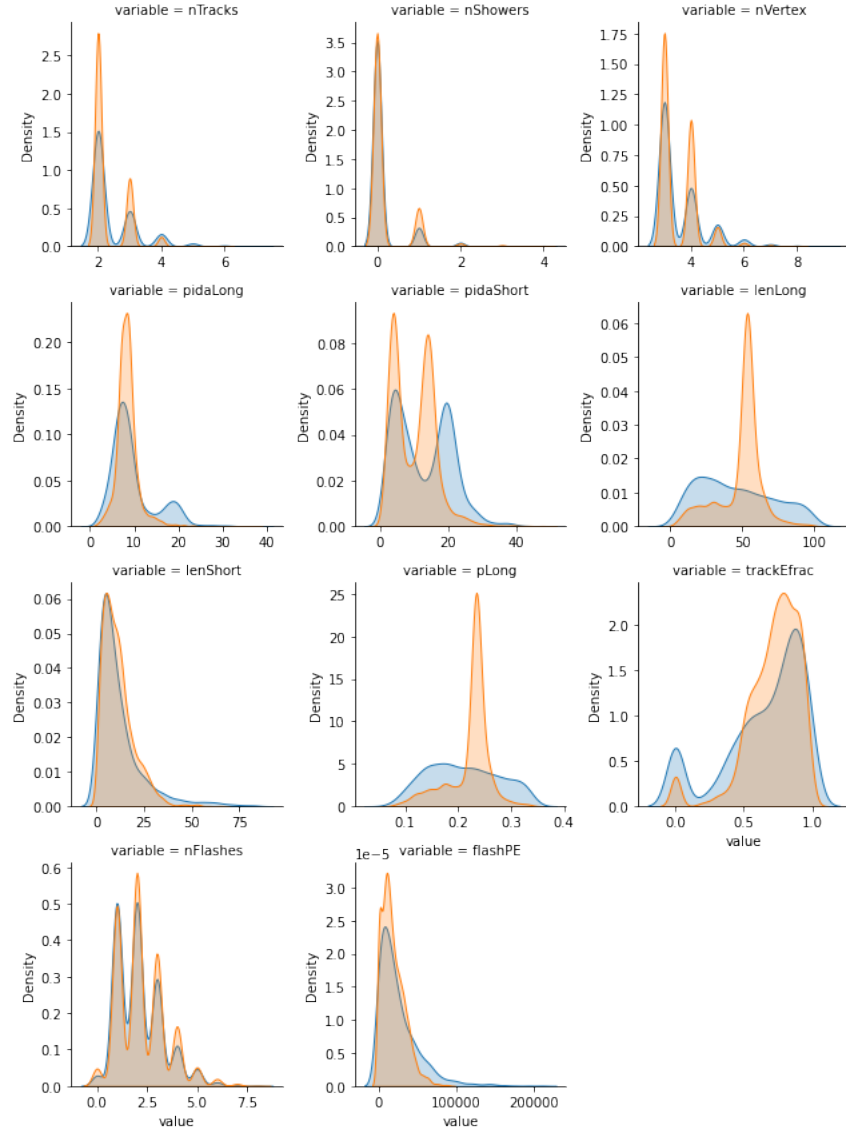


Figure 5.10: Input variables for the signal and background for flash matched xenon-doped events.



## Chapter 6

# Conclusion

The operation of the ProtoDUNE-SP detector was quite the successful campaign. The detector successfully operated for multiple years, characterizing the technologies intended for the DUNE far detector, as well as studying various particle cross sections and scintillation light in liquid argon. This work discussed the attenuation and Rayleigh Scattering length of the 127nm scintillation light in a LAr environment. This was measured to be  $93 \pm 5\text{cm}$ , agreeing with the most recent results[61][62][46].

The effect of nitrogen quenching were also studied. This specific contaminant has been fairly well studied in the past, as most recirculation and filtration systems in use in modern TPCs cannot filter out nitrogen effectively. In ProtoDUNE-SP, 5.7 ppm of nitrogen was introduced to the system and was seen to quench the LAr scintillation light by nearly 50% without introducing further absorption effects. The ratio of scintillation light with and without the presence of a 500 V cm electric field was also seen to behave as expected from literature, showing approximately a 35% decrease in light with the field on. There is some evidence of a discrepancy in the distribution of the light collected over a distance in cases where the field is and is not applied, but nothing was confirmed in this work.

The addition of xenon has been shown to alleviate the quenching due to the nitrogen contamination. 18.8ppm of xenon was injected into ProtoDUNE-SP, which successfully returned the light yield to that of pure liquid argon in the presence of nitrogen. This same xenon injection was also shown

to increase the uniformity of light over the 3.6m drift distance in ProtoDUNE-SP. This increase in uniformity, and increased performance at long distances with respect to pure argon, is largely an effect of the increased rayleigh scattering length of xenon. This work favors a value of  $867 \pm 12.5\text{cm}$  for the Rayleigh scattering length of the 175nm xenon scintillation light in an argon medium. This is over nine times that of the argon scintillation light, and agrees very well with the expected values. This makes xenon an attractive dopant option to increase the photon detection abilities in DUNE.

The addition of xenon in a liquid argon TPC was shown to have many positive qualities from a scintillation light perspective. The study at ProtoDUNE-SP also showed that the injection had little effect on the drift charge in the TPC. The influence of the doping on the expected proton decay identification capabilities was studied, since there was no clear evidence of loss of charge reconstructed and the increased light yield and uniformity has the potential to positively impact the study. A series of machine-learning classifiers were trained on monte-carlo samples using a standard and improved flash-matching timing scheme in a pure argon and xenon doped argon sample. The performance of these classifiers did not significantly change with the introduction of xenon, showing that the sensitivity to detect proton decay, which is a major physics charge for DUNE, is not influenced by the addition of xenon. This lack of impact further supports the addition of xenon as a dopant in LArTPCs.

## Appendices

## Appendix A

# Supplemental Information

### A.1 Photon Detection System Calibration

As with all detectors in the prototyping and initial data-taking periods, all detector components need to be calibrated so that all future data is well understood and the proper conclusions can be reached. The PDSP PDS, the construction of which is described in 2.4.2, is no exception to this. Each individual PDS module is readout by a series of ganged SiPMs, whose readout ADC per photon is slightly different from one another. These SiPM readouts need to be calibrated so that the integrated charge on the chip can be converted to the number of detected photons from the detector. The readout from the SSP is a time dependent waveform, representing ADC vs time, as seen in figure ??.

One can see the offset described in the same section, with the waveform beginning at  $t = 250ns$ , and running for  $13.3\mu s$ . The integrated charge on this readout channel represents the number of photon collected by this readout channel during this event. To calibrated this value, a large sample size that contains events with 1, 2, 3, ... photons needs to be collected for all PDS readout channels.

During the initial data taking period of PDSP, a series of calibration runs were taken, where a series of LEDs were illuminated periodically and triggered the data readout.. These LEDs are distributed throughout the cryostat, and illuminate the entire drift volume. The positioning of the LEDs allow them to illuminate the PDS modules with a varying number of photons each. Modules far from the

LED(s) may see zero or one photon, while closer modules have the possibility of seeing many more. The readout waveforms for many of these events can then be plotted together on one plot, as done in figure ?? . The waveforms in this figure come from a DSLG with a SensL C-series SiPM. By eye, one can clearly see the distribution of multi-photon events. The integral of these peaks can then be histogrammed, and the peaks fit to find the total integrated ADC for each peak. When fit with a line, the slope of this value returns the  $\text{ADC}/\gamma$  value. To allow for noise reduction and consistent

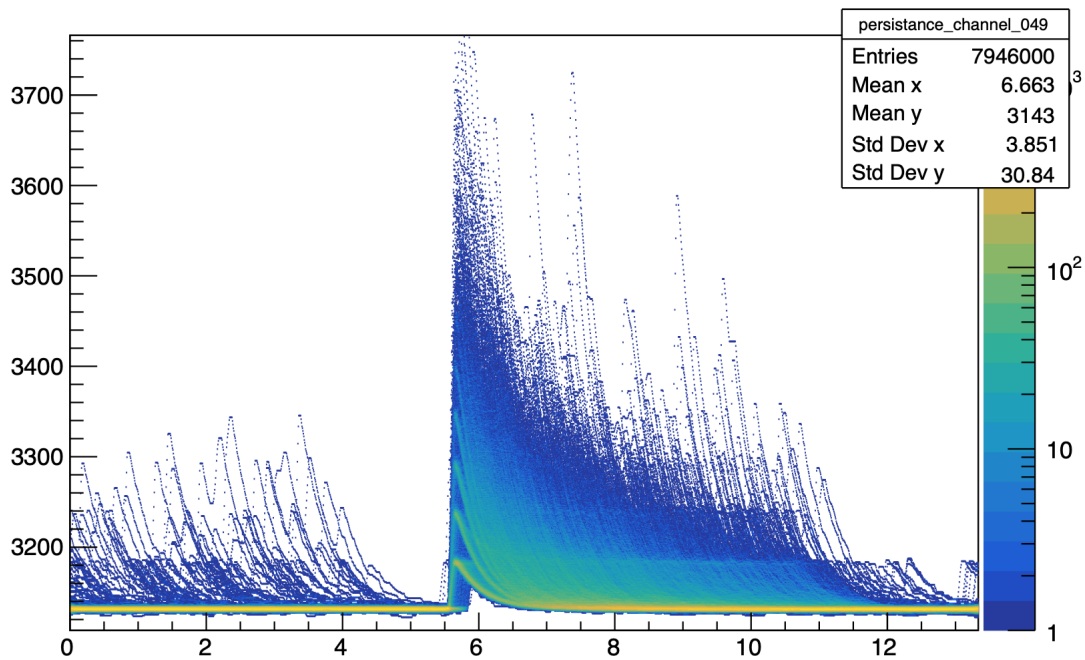


Figure A.1: The readout of a single SensL C-Series PDS module from many events. The persistence traces of an integer number of photons incident on the SiPM can clearly be seen.

calculations, a system was implemented to calculate this integrated charge.

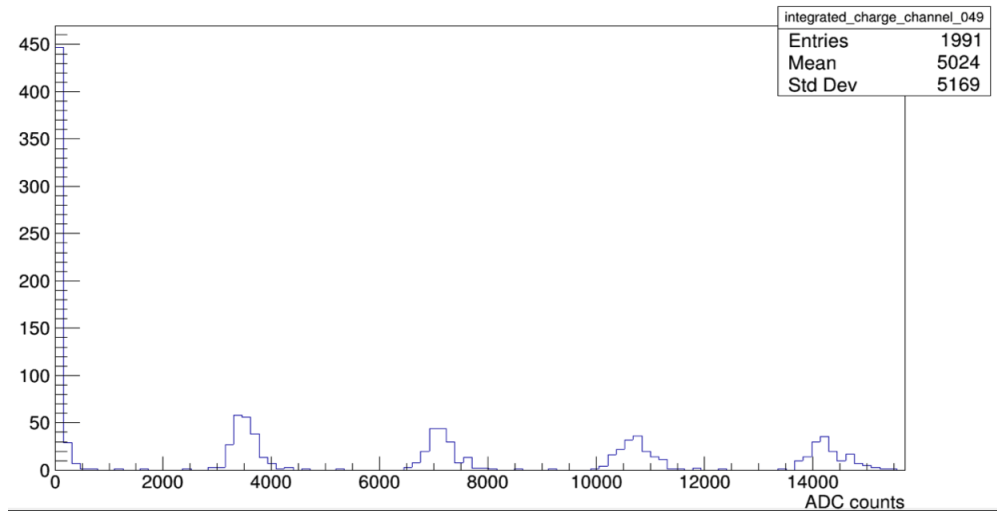
First, the baseline for the individual readout was calculated using the first 40 samples of the readout. This allows for each sample used in the integration to be w.r.t zero, and not offset by some slightly varying baseline value. This also allows one to calculate the variance from the baseline, allowing one to cut on only large, non-noise peaks. The built in ROOT<sup>1</sup> peakfinding algorithm was then used to locate peaks in the waveform readout that had values greater than  $5\sigma$  above the baseline. From

<sup>1</sup><https://root.cern>

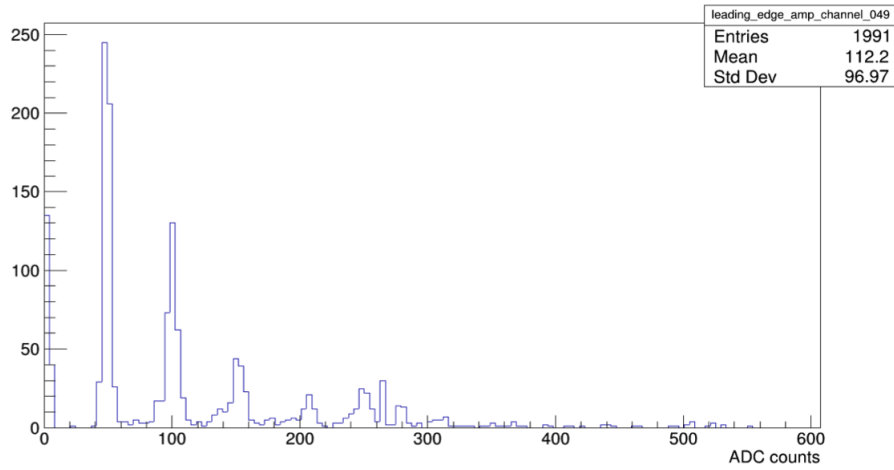
this peak point, 5 samples behind and 245 samples forward were integrated. This gives us a histogram full of integrated ADC charges which can be analyzed using the procedure above. Also illuminating, is a similar plot of the leading edge amplitude. This plot alone gives a similar relationship to the integrated charge, though with no calibration uses. When plotted together, the leading edge amplitude versus integrated charge plot gives a better picture of the relationship between the two, and also the modal nature of photon collection. All three of these plots for the above persistence trace can be seen in figure ?? Here, the increasing integer number of photons can be clearly seen, allowing very precise differentiation.

As has been discussed in detail, ProtoDUNE-SP is a testbed for a variety of technology candidates for the DUNE far detector. Due to this, the PDS is composed of 3 bar technologies with 5 different SiPM chips installed throughout. This means that there is a lot of variability in the readout chips, or the bar responses. In spite of this large variability, all of these individual readout channels must be calibrated. Some technologies used in PDSP do not read out as cleanly as others, or the example above. Figure ?? shows these combinations here, and Fermilab constructed bars with the Hamamatsu SiPMs perform significantly less consistently in this waveform space than the SensL example above. Shown in figure ??, the waveform persistence traces does not have a clear modal behavior. This creates a challenge for calibration. As discussed above, switching to the amplitude versus integral phase space helps to resolve some of these behaviors, but the performance of this plot also follows the performance of the trace plots. Though there is more discerning power, there is still no clear behavior in these plots. There are something like two discern-able peaks, which trend into the two-dimensional plot where two distinct trend lines exist, allowing calibration to proceed. Similar results for the ARAPUCA are shown in ?. Here, calibration appears slightly easier.

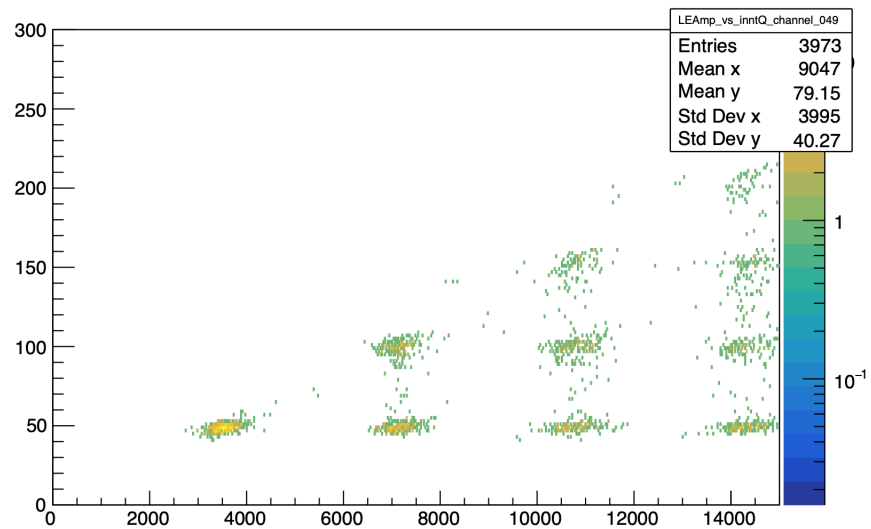
The above plots are relatively statistically lacking. As more data was processed, a more complete dataset and better analysis methods led to final calibrations by other members of the calibration.



(a)

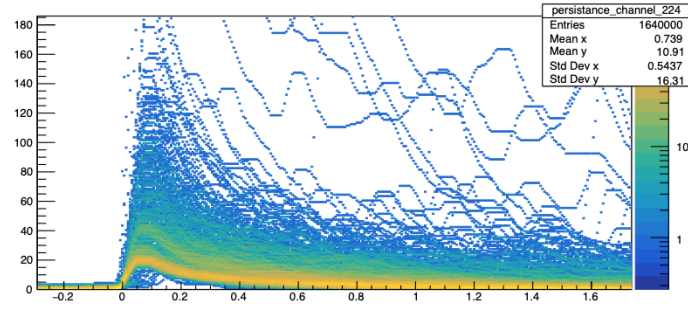


(b)



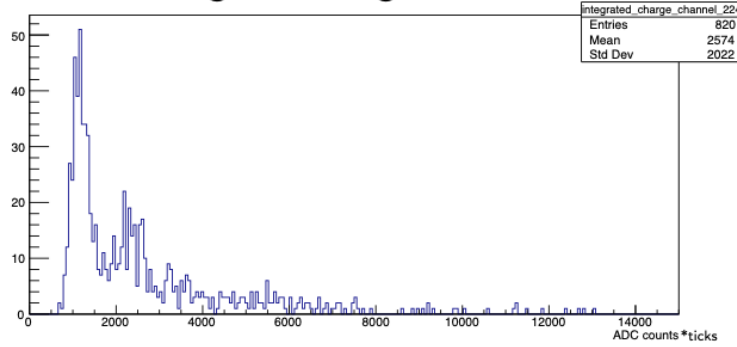
(c)

Figure A.2: A single DSLG with a SensL C-series SiPM that displayed strong response and an easy to calibrate behavior in ProtoDUNE-SP.



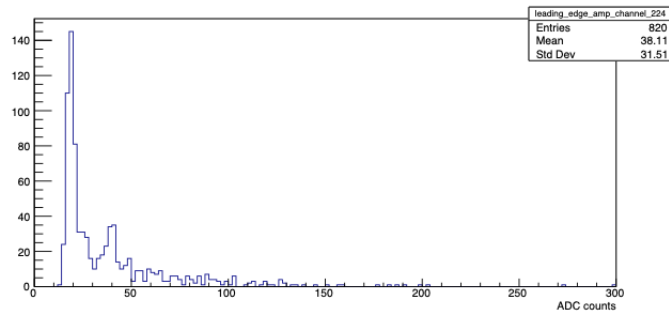
(a)

### Integrated charge distribution

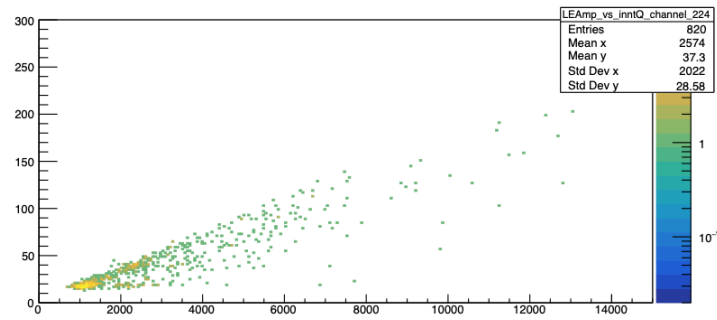


(b)

### Leading edge amplitude distribution



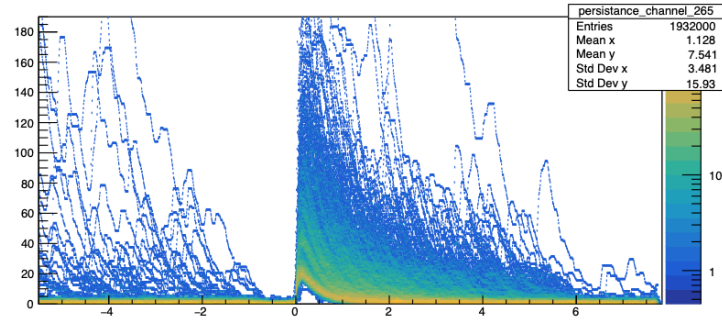
(c)



(d)

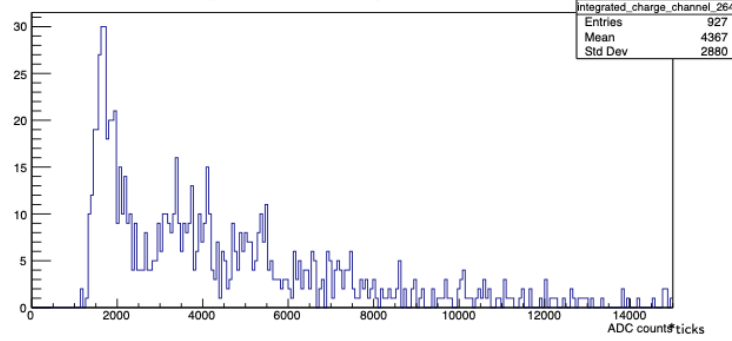
Figure A.3: A layout of the steps taken to calibrate a single DSLG with a Hamamatsu SiPM in the ProtoDUNE-SP photon detection system. (a) The collection of multiple readout waveforms. (b) A histogram of the integral of all of the waveforms collected. (c) The amplitude of the leading edge of these waveforms. (d) a plot of (c) versus (b), searching for a nodes in the multi-dimensional space.





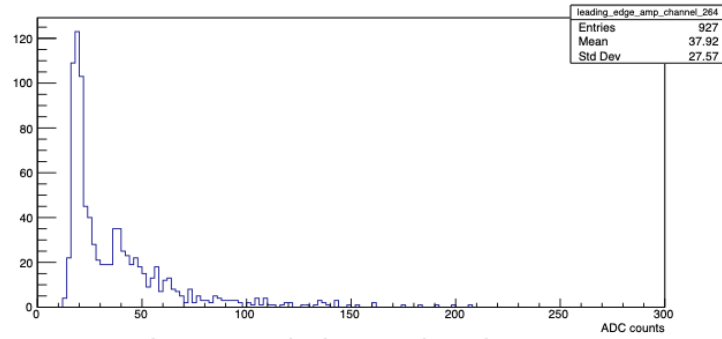
(a)

### Integrated charge distribution

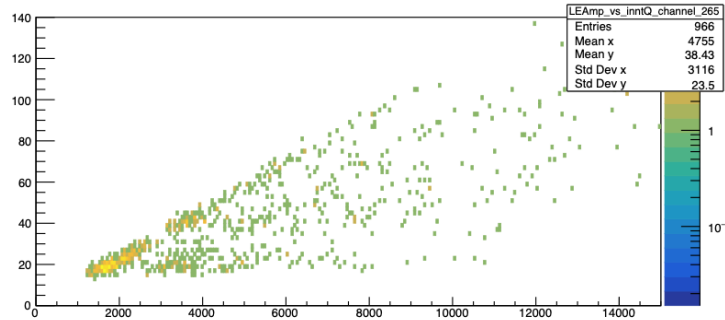


(b)

### Leading edge amplitude distribution



(c)



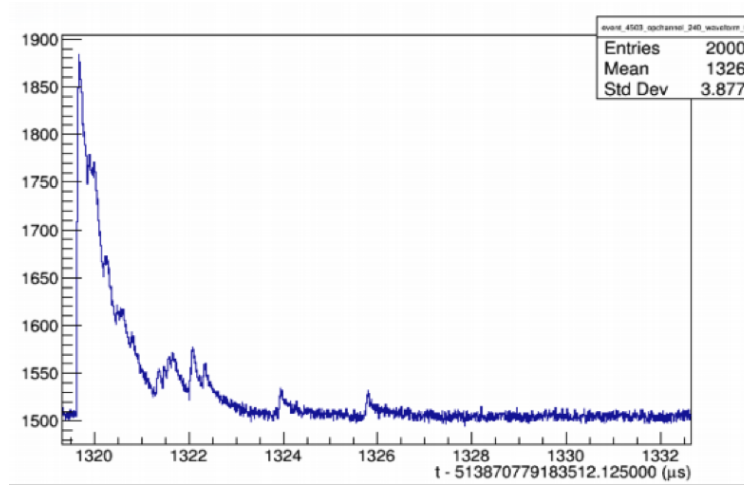
(d)

Figure A.4: A layout of the steps taken to calibrate the ARAPUCA in the ProtoDUNE-SP photon detection system. (a) The collection of multiple readout waveforms. (b) A histogram of the integral of all of the waveforms collected. (c) The amplitude of the leading edge of these waveforms. (d) a plot of (c) versus (b), searching for a nodes in the multi-dimensional space.

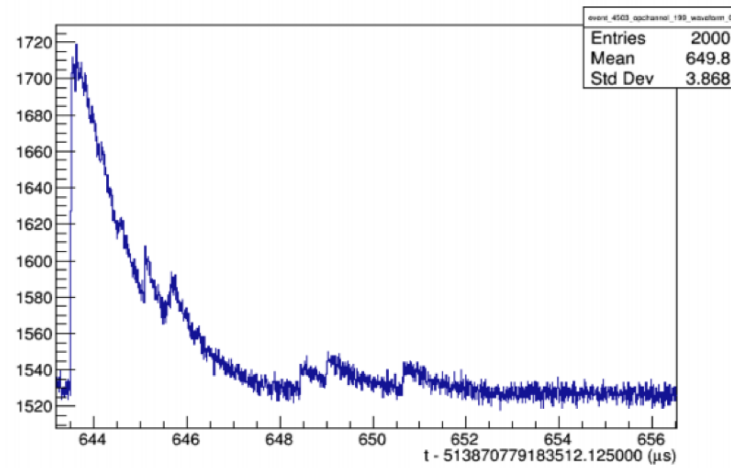
## A.2 Flash Calibration

After calibrations of the photon detection system itself, the software needs to be calibrated. Most of the PDS analysis and structure is carried over from other neutrino experiments. This ports relatively well, but does necessitate finalizing the behavior once specific technologies are installed or behaviors are identified. In the ProtoDUNE software, the optical hit and flash (a collation of optical hits) are calculated and formed directly from the SSP readout waveforms, and used later in the reconstruction and analysis chains. The optical hit is a single spike in the waveform on a single channel, that represents a number of photons incident on that optical channel at a specific time with a specific width. There are other characteristics in the optical hit, but they are not relevant to this document. After the calibration of the PDS, the software was producing a wide range of optical hits, some missing obvious candidates and some including noise as hits. In figure ??, we see two readout waveforms from PDSP. For example, in ?? we see something like expected behavior, with one large flash  $4\mu s$  wide and two smaller hits. However, we also see 22 other hits in this waveform. In ?? we see nearly completely opposite the behavior, where we have 1 flash of width  $13\mu s$ . Clearly, both of these are extreme cases, but need to be characterized and sorted for proper operation and use.

Calculation of the optical hit amplitude and integral, and therefore the number of photons as described above, is dependent on accurate calculation of the baseline of the waveform. Within the PDSP reconstruction software, the baseline of these waveforms was initially set as a constant, with a value of  $1500ADC$ . The specific value is roughly what one expects from a SensL C-series SiPM, in general, but as stated above there is some expected deviation in this number. In figure ?? we can see that this preset baseline is clearly a cause to one of these issues, with ?? clearly having a baseline of  $1520$ , which resulted in a singular long hit instead of the expected behavior. This calculation was changed to intelligently look at the front and back of the waveform and calculate a baseline in both. It then compares the two calculations and looks for activity in either, and if so it discards that section of the waveform. It then calculates the baseline from the remaining sections. This resulted



(a)



(b)

Figure A.5: Two similar waveforms which were characterized quite differently in the optical-hit finding. (a) was characterized as having 25 optical hits while (b) registered just a single hit. Neither behavior is expected.

in removal of the exceptionally long hits.

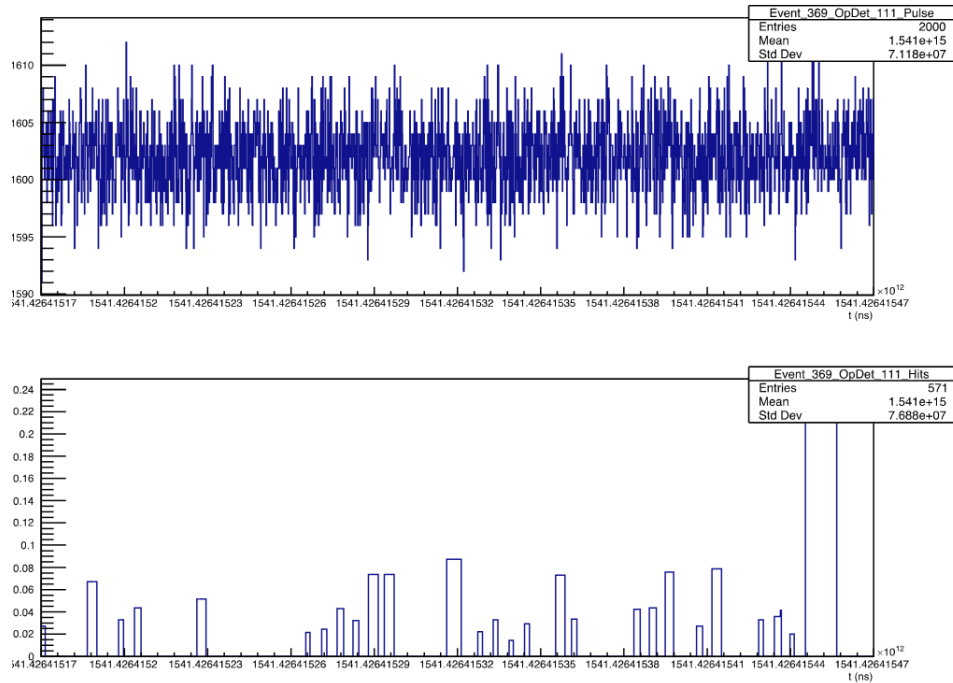
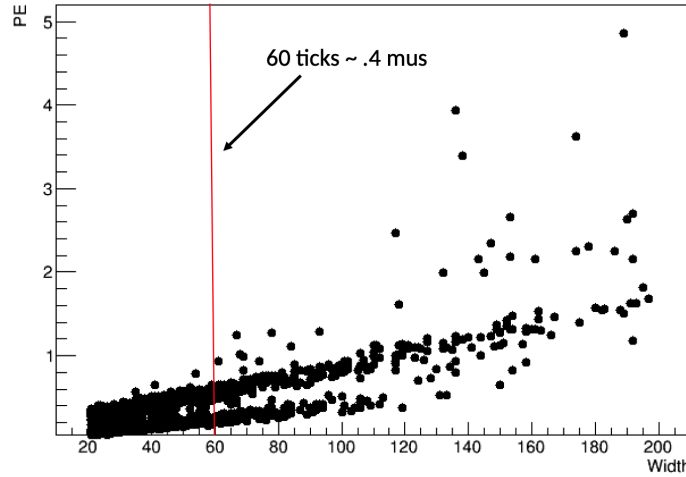


Figure A.6: (top) A waveform with no activity on it. (bottom) The locations and widths of the optical hits detected in the waveform in (top)

The second errant behavior is the presence of many small hits, dispersed throughout the waveform. This behavior could be seen exceptionally well if one looks at a waveform with no activity in it. The example in figure ?? reported nearly 30 hits. There are many options in the hit finding algorithm that could cause this sort of behavior. To find hits, the algorithm loops over the samples in the waveform and looks for a peak some number of  $\sigma$  above the baseline with a width greater than or equal to some preset value. If the peak value is set too low, the baseline deviation is being miscalculated, or the width cutoff for a peak is set too low these low sporadic hits can occur. Amplitude setting and variance calculations are both carry-overs from another physics experiment, so the expectation of correctness is present. In this case, this idea holds true and the variance calculation is standard and the amplitude is set as a configurable. The distribution of number of detected photons vs hit width between 20 and 200 for a sample of optical hits is shown in figure ?. One can see that there is a large number of low (sub-integer) photon hits with widths less than 100 SSP ticks. A somewhat arbitrary

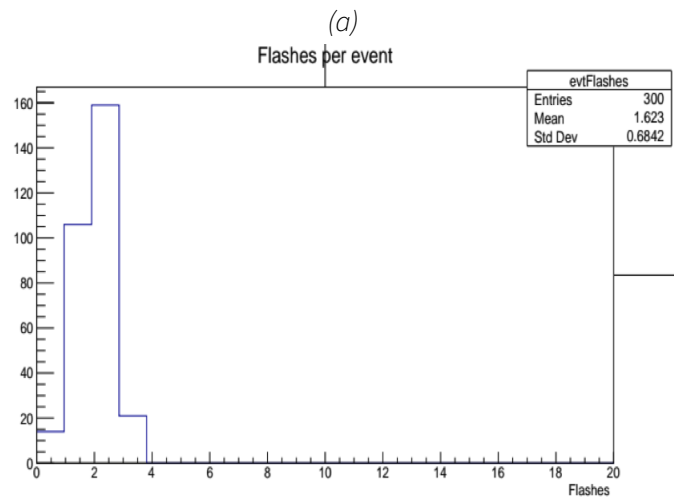
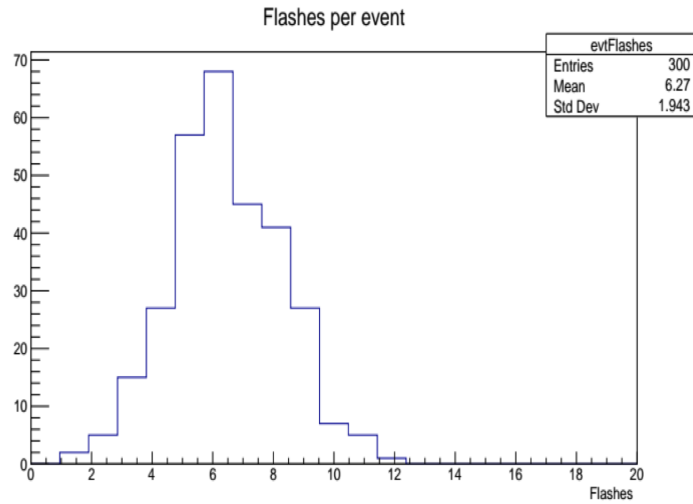
cut on 60 ticks was chosen, resulting in large removal of very small optical hits while leaving room for short integer sized hits to pass this cut. Once this cut was approved and pushed to software, the behavior of the optical hit detection exhibited the expected behavior.



*Figure A.7: The number of photons collected in an optical hit versus the selected time width of the hit. A cut was implemented, as shown in red, setting the minimum tick width to 60.*

Once optical hit finding has been modified and finalized, a look at how the software grouped these hits into optical flashes was necessary, to make sure no major (negative) changes were committed to shared reconstruction software. Flashes in PDSP were not well characterized or classified prior to this work. The knowledge of optical flashes in these detectors was carried over from the operational experience of MiniBoone, and much of this was still applicable to ProtoDUNE-SP. That being said, there are goals of DUNE that are not aligned with those of the MiniBoone experiment. The flash finding algorithm, OpFlashAlg, that was ported from that experiment works well for cosmic rays and beam particles, but is designed to look for simultaneous optical hits in relatively small windows, meaning that a single PDS readout could have more than two flashes included, if other PDS modules have similar activity. This is fine behavior for many cases, but does mean that late light from an event could be misplaced into another reconstructed flash.

In a standard cosmic event in PDSP, one might expect to have one flash coincident with the CRT trigger, and a very small number of additional flashes in the externally triggered flash set. To note



(b)

Figure A.8: The total number of optical flashes reconstructed for (a) the standard flash finding algorithm and (b) the OpSlicer algorithm. The design of the OpSlicer algorithm is clearly seen, with it reconstructing significantly fewer flashes than the standard algorithm.

here, PDSP separates flashes into externally triggered, where the PDS waveforms are readout from a CRT or software triggered event and reconstructed, and internal flashes, where the waveforms are readout when activity of a certain size is detected in the PDS module. When events are triggered by a cosmic ray track, the  $13\mu s$  readout is expected to see a small number of muons active in the detector, the one that triggered the CRT and a small number of coincident spurious events in the detector. When the number of flashes per externally triggered event is plotted, as in figure ??, it is clear that there are more flashes than one might expect in such an event using the reasoning just described. Characterization of these flashes is necessary to confirm this is the right logic. To serve as a comparison, a second flash matching algorithm was analyzed for comparison and simultaneous characterization. This second algorithm is called "OpSlicer", and was designed specifically for experiments which use SiPMs, as opposed to PMTs, which have a different readout structure. This second algorithm is also designed with an emphasis on collecting late light from the event.

Figure ?? shows the number of flashes per event for the OpSlicer algorithm. It is clear that this algorithm and OpFlashAlg have very different behavior. This is expected because OpSlicer is designed to collect optical hits over a longer time period, collecting as much light as possible to be used for low energy events. Figure ?? shows the characteristics of the flashes for both algorithms, with ?? shows it  $\log(\gamma)$  for the largest flash, ?? shows it  $\log(\gamma)$  for the second largest flash, and ?? shows the time difference between the largest flash and other flashes in the event, separated into large ( $O[largestflash]$ ) and small flashes ( $O[.3 * largest]$ ). The behavior of the two algorithms is clear here, with OpSlicer finding fewer large flashes, per its design, and OpFlashAlg finding many flashes of differing sizes dispersed throughout the event. This behavior is fine, as long as the analyzer knows of the behavior and can act accordingly. Once these plots are analyzed, one can characterize the flashes into four categories. There is the largest flash, or the triggering cosmic ray. Other very large flashes in the event are certainly (other) cosmic ray activity, given PDSP's location on the surface. Small flashes after the largest flash is attributed to late light, or photons originating from the cosmic ray that takes more time to travel to the PDS. Small flashes that occur before the large flash can be attributed to noise, reflections, or small cosmic ray event that may not traverse much of the

detector. These flashes can largely be ignored or disregarded in analysis. The number of each of these types of flashes can be seen figure ?? and in table ?. The number of late light flashes is calculated as the number of small flashes after the large flash minus the number of small flashes before in the same event. The number of noise flashes is twice the sum of the small flashes before the largest flash, to account for only summing a part of the time space.

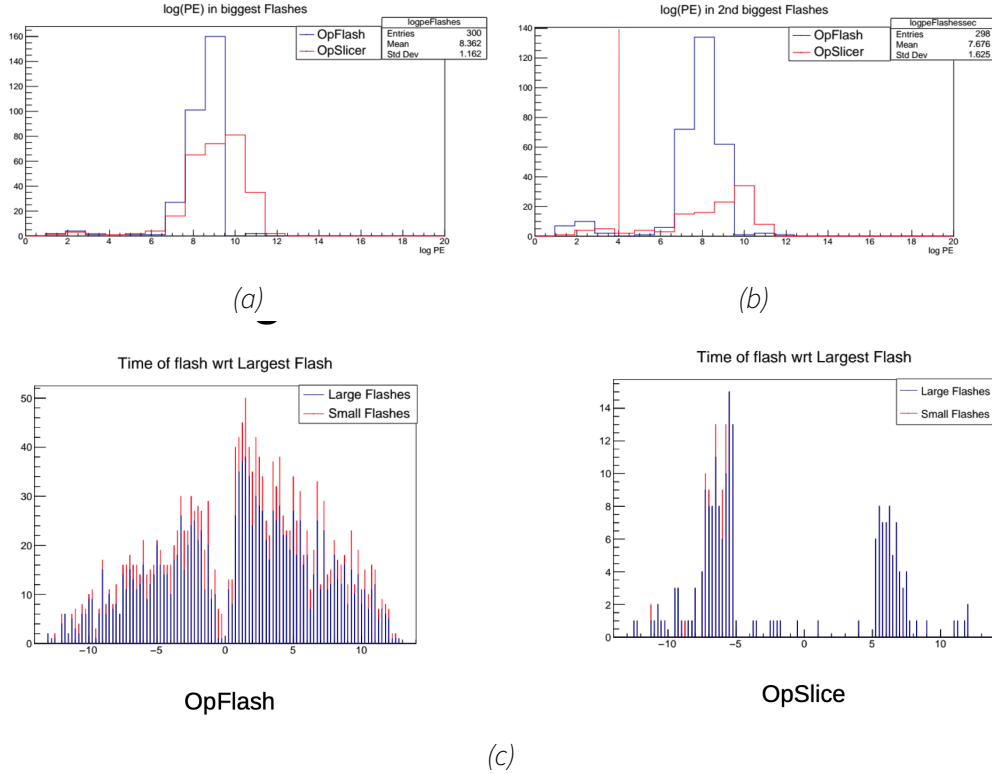
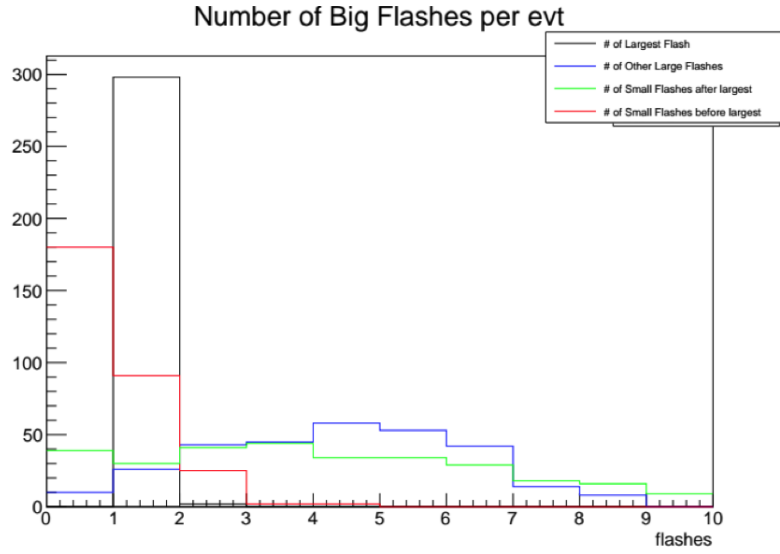


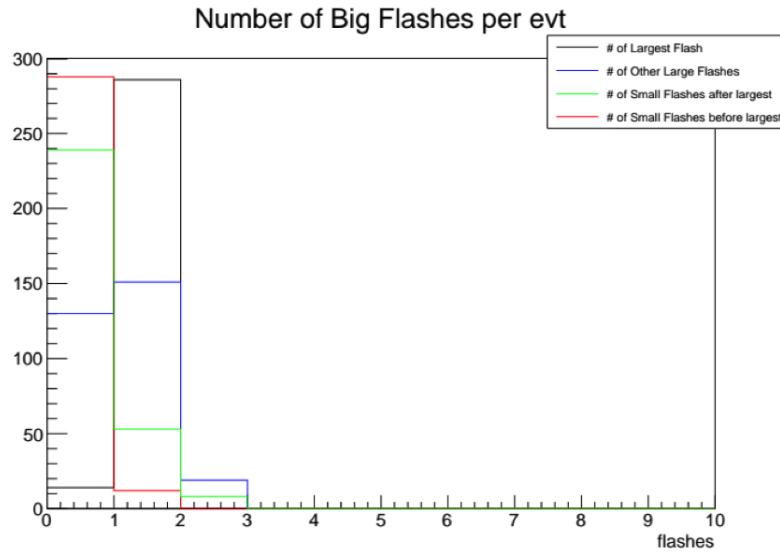
Figure A.9: Three metrics used to characterize the flash finding algorithms. The size of the (a) largest and (b) second largest flashes in the events, as well as (c) the offset of these flashes from the event time for both algorithms.

Overall, with the change made to the optical hits, the flash matching algorithm worked as intended. Once all parts of the reconstruction were operational, work was done to analyze and characterize the flashes in PDSP. Here, we can see that OpFlashAlg characterizes one flash per trigger, plus late light. Often, there is other activity in the event that is also collated into flashes. The OpSlicer algorithm takes the majority of these same events and groups them into one or two flashes, due to the main design feature of the algorithm being to collect early and late light from SiPM readouts in





(a)



(b)

Figure A.10: Characterization of optical flash events for the (a) standard flash finding algorithm and the (b) algorithm designed to collect late light for small energy events.

Category	OpFlashAlg	OpSlicer
BiggestFlash	1	.95
Other Cosmics	3.9	.63
Late Light	3.09	.17
Noise	1	.08

Table A.1: In this table, the number of flashes in each category is presented for each flash finding algorithm discussed in this section.

LArTPCs. All changes to the reconstruction software were pushed to shared resources and used in production.

## References

- [1] Y. Fukuda et al. “Evidence for Oscillation of Atmospheric Neutrinos”. In: *Physical Review Letters* 81.8 (Aug. 1998), pp. 1562–1567. DOI: 10.1103/physrevlett.81.1562. URL: <https://doi.org/10.1103/physrevlett.81.1562> (cit. on p. 1).
- [2] Peter W. Higgs. “Broken Symmetries and the Masses of Gauge Bosons”. In: 13.16 (Oct. 1964), pp. 508–509. DOI: 10.1103/PhysRevLett.13.508 (cit. on p. 2).
- [3] University of Zurich. *The Standard Model*. 2018. URL: <https://www.physik.uzh.ch/en/researcharea/lhcb/outreach/StandardModel.html> (visited on 06/30/2022) (cit. on p. 3).
- [4] M Baggett, N Baggett, and F Eisele. “MEASUREMENT OF THE RATIO AXIAL VECTOR TO VECTOR COUPLING CONSTANT  $g_{sub1}/f_{sub1}$  absolute value IN  $\lambda$  Yields  $\nu_{sup}$ — anti  $\nu$  DECAY.” In: *Z. Phys.* 249: No. 4, 279-85(1972). (Jan. 1972). DOI: 10.1007/BF01379721. URL: <https://www.osti.gov/biblio/4710203> (cit. on p. 5).
- [5] Nicola Cabibbo. “Unitary Symmetry and Leptonic Decays”. In: 10.12 (June 1963), pp. 531–533. DOI: 10.1103/PhysRevLett.10.531 (cit. on p. 5).
- [6] M. Kobayashi and T. Maskawa. “CP-Violation in the Renormalizable Theory of Weak Interaction”. In: *Progress of Theoretical Physics* 49.2 (Feb. 1973), pp. 652–657. DOI: 10.1143/PTP.49.652 (cit. on p. 5).
- [7] Susanne Mertens. “Direct Neutrino Mass Experiments”. In: *Journal of Physics Conference Series*. Vol. 718. Journal of Physics Conference Series. May 2016, p. 022013. DOI: 10.1088/1742-6596/718/2/022013. arXiv: 1605.01579 [nucl-ex] (cit. on p. 6).

- [8] P. Hernandez. “Neutrino physics”. In: (Aug. 2017). 58 pages, contribution to the CERN in the Proceedings of the 2015 CERN-Latin-American School of High-Energy Physics, Ibarra, Ecuador, 4 - 17 March 2015. arXiv admin note: text overlap with arXiv:1010.4131, 85–142. 58 p. DOI: **10.5170/CERN-2016-005.85**. arXiv: **1708.01046**. URL: **<https://cds.cern.ch/record/2243592>** (cit. on p. 6).
- [9] J Chadwick. “Intensitätsverteilung im magnetischen Spectrum der  $\beta$ -Strahlen von radium B + C”. In: *Verhandl. Dtsc. Phys. Ges.* 16 (1914), p. 383. URL: **<https://cds.cern.ch/record/262756>** (cit. on p. 6).
- [10] N. Bohr, H. A. Kramers, and J. C. Slater. “Über die Quantentheorie der Strahlung”. In: *Zeitschrift für Physik* 24.1 (Dec. 1924), pp. 69–87. DOI: **10.1007/BF01327235** (cit. on p. 7).
- [11] C. S. Wu, E. Ambler, R. W. Hayward, D. D. Hoppes, and R. P. Hudson. “Experimental Test of Parity Conservation in Beta Decay”. In: *Physical Review* 105.4 (Feb. 1957), pp. 1413–1415. DOI: **10.1103/PhysRev.105.1413** (cit. on pp. 7, 12).
- [12] Jr. Cowan C. L., F. Reines, F. B. Harrison, H. W. Kruse, and A. D. McGuire. “Detection of the Free Neutrino: A Confirmation”. In: *Science* 124.3212 (July 1956), pp. 103–104. DOI: **10.1126/science.124.3212.103** (cit. on p. 7).
- [13] Raymond Davis Jr., Don S. Harmer, and Kenneth C. Hoffman. “Search for neutrinos from the sun”. In: *Physical Review Letters* 20.21 (1968). Cited by: 784, pp. 1205–1209. DOI: **10.1103/PhysRevLett.20.1205**. URL: **<https://www.scopus.com/inward/record.uri?eid=2-s2.0-12744261626&doi=10.1103%2fPhysRevLett.20.1205&partnerID=40&md5=dcc5a01f397e8eeb80>** (cit. on p. 8).
- [14] B. Pontecorvo. “Mesonium and Antimesonium”. In: *Soviet Journal of Experimental and Theoretical Physics* 6 (Jan. 1958), p. 429 (cit. on p. 8).
- [15] Z. Maki, M. Nakagawa, and S. Sakata. “Remarks on the Unified Model of Elementary Particles”. In: *Progress of Theoretical Physics* 28.5 (Nov. 1962), pp. 870–880. DOI: **10.1143/PTP.28.870** (cit. on p. 8).
- [16] M. H. Ahn et al. “Measurement of neutrino oscillation by the K2K experiment”. In: *Phys. Rev.*

- D* 74 (7 Oct. 2006), p. 072003. DOI: 10.1103/PhysRevD.74.072003. URL: <https://link.aps.org/doi/10.1103/PhysRevD.74.072003> (cit. on p. 11).
- [17] J. H. Christenson, J. W. Cronin, V. L. Fitch, and R. Turlay. “Evidence for the  $2\pi$  Decay of the  $K_2^0$  Meson”. In: *Phys. Rev. Lett.* 13 (4 July 1964), pp. 138–140. DOI: 10.1103/PhysRevLett.13.138. URL: <https://link.aps.org/doi/10.1103/PhysRevLett.13.138> (cit. on p. 12).
- [18] Ettore Majorana. “Teoria simmetrica dell’elettrone e del positrone”. In: *Il Nuovo Cimento (1924-1942)* 14.4 (1937), p. 171 (cit. on p. 12).
- [19] E. Akhmedov, P. Lipari, and M. Lusignoli. “Matter effects in atmospheric neutrino oscillations”. In: *Physics Letters B* 300.1-2 (Feb. 1993), pp. 128–136. DOI: 10.1016/0370-2693(93)90759-b (cit. on p. 13).
- [20] C. Athanassopoulos, L. B. Auerbach, D. Bauer, R. D. Bolton, R. L. Burman, I. Cohen, D. O. Caldwell, B. D. Dieterle, J. B. Donahue, A. M. Eisner, A. Fazely, F. J. Federspiel, G. T. Garvey, M. Gray, R. M. Gunasingha, V. Highland, R. Imlay, K. Johnston, H. J. Kim, W. C. Louis, A. Lu, J. Margulies, G. B. Mills, K. McIlhany, W. Metcalf, R. A. Reeder, V. Sandberg, M. Schillaci, D. Smith, I. Stancu, W. Strossman, R. Tayloe, G. J. VanDalen, W. Vernon, Y. -X. Wang, D. H. White, D. Whitehouse, D. Works, Y. Xiao, and S. Yellin. “The liquid scintillator neutrino detector and LAMPF neutrino source”. In: *Nuclear Instruments and Methods in Physics Research A* 388.1-2 (Feb. 1997), pp. 149–172. DOI: 10.1016/S0168-9002(96)01155-2. arXiv: [nuc1-ex/9605002](https://arxiv.org/abs/nuc1-ex/9605002) [nuc1-ex] (cit. on p. 13).
- [21] Andrei D. Sakharov. “SPECIAL ISSUE: Violation of CP in variance, C asymmetry, and baryon asymmetry of the universe”. In: *Soviet Physics Uspekhi* 34.5 (May 1991), pp. 392–393. DOI: 10.1070/PU1991v034n05ABEH002497 (cit. on p. 13).
- [22] RICARDO GONZÁ LEZ FELIPE. “NEUTRINOS AND THE MATTER-ANTIMATTER ASYMMETRY IN THE UNIVERSE”. In: *International Journal of Modern Physics E* 20.sup01 (Dec. 2011), pp. 56–64. DOI: 10.1142/s0218301311040074. URL: <https://doi.org/10.1142%2Fs0218301311040074> (cit. on p. 13).
- [23] A. Serebrov, V. Varlamov, A. Kharitonov, A. Fomin, Yu. Pokotilovski, P. Geltenbort, J. Butter-

- worth, I. Krasnoschekova, M. Lasakov, R. Tal'daev, A. Vassiljev, and O. Zhrebtsov. "Measurement of the neutron lifetime using a gravitational trap and a low-temperature Fomblin coating". In: *Physics Letters B* 605.1 (2005), pp. 72–78. DOI: <https://doi.org/10.1016/j.physletb.2004.11.013>. URL: <https://www.sciencedirect.com/science/article/pii/S0370269304015552> (cit. on p. 13).
- [24] Borut Bajc, Junji Hisano, Takumi Kuwahara, and Yuji Omura. "Threshold corrections to dimension-six proton decay operators in non-minimal SUSY SU(5) GUTs". In: *Nuclear Physics B* 910 (Sept. 2016), pp. 1–22. DOI: [10.1016/j.nuclphysb.2016.06.017](https://doi.org/10.1016/j.nuclphysb.2016.06.017). arXiv: 1603.03568 [hep-ph] (cit. on p. 14).
- [25] N. Sakai and Tsutomu Yanagida. "Proton decay in a class of supersymmetric grand unified models". In: *Nuclear Physics B* 197.3 (1982), pp. 533–542. DOI: [https://doi.org/10.1016/0550-3213\(82\)90457-6](https://doi.org/10.1016/0550-3213(82)90457-6). URL: <https://www.sciencedirect.com/science/article/pii/0550321382904576> (cit. on pp. 15, 16, 21).
- [26] Luca Di Luzio. *Aspects of symmetry breaking in Grand Unified Theories*. 2011. DOI: [10.48550/ARXIV.1110.3210](https://arxiv.org/abs/1110.3210). URL: <https://arxiv.org/abs/1110.3210> (cit. on p. 15).
- [27] Yunfei Wu and Da-Xin Zhang. "Study of non-minimal SUSY SU(5) model with realistic fermion sectors". In: *Journal of High Energy Physics* 2011.1 (Jan. 2011). DOI: [10.1007/jhep01\(2011\)074](https://doi.org/10.1007/jhep01(2011)074). URL: <https://doi.org/10.1007%2Fjhep01%282011%29074> (cit. on p. 16).
- [28] Steven Abel, Keith R. Dienes, and Eirini Mavroudi. "Towards a nonsupersymmetric string phenomenology". In: 91.12, 126014 (June 2015), p. 126014. DOI: [10.1103/PhysRevD.91.126014](https://doi.org/10.1103/PhysRevD.91.126014). arXiv: 1502.03087 [hep-th] (cit. on p. 16).
- [29] Zurab Berezhiani. *Solving SUSY GUT Problems: Gauge Hierarchy and Fermion Masses*. 1994. DOI: [10.48550/ARXIV.HEP-PH/9412372](https://arxiv.org/abs/hep-ph/9412372). URL: <https://arxiv.org/abs/hep-ph/9412372> (cit. on p. 16).
- [30] Helge Egil Seime Pettersen. "The Higgs Boson in Less Constrained Supersymmetric Models". PhD thesis. June 2012 (cit. on p. 17).
- [31] Howard Georgi and S. L. Glashow. "Unity of All Elementary-Particle Forces". In: *Phys. Rev. Lett.*

- 32 (8 Feb. 1974), pp. 438–441. DOI: [10.1103/PhysRevLett.32.438](https://doi.org/10.1103/PhysRevLett.32.438). URL: <https://link.aps.org/doi/10.1103/PhysRevLett.32.438> (cit. on pp. 16, 21).
- [32] DUNE Collaboration et al. *Long-Baseline Neutrino Facility (LBNF) and Deep Underground Neutrino Experiment (DUNE) Conceptual Design Report Volume 2: The Physics Program for DUNE at LBNF*. 2015. DOI: [10.48550/ARXIV.1512.06148](https://doi.org/10.48550/ARXIV.1512.06148). URL: <https://arxiv.org/abs/1512.06148> (cit. on p. 20).
- [33] B. et al. Abi. “Deep Underground Neutrino Experiment (DUNE), Far Detector Technical Design Report, Volume IV: Far Detector Single-phase Technology”. In: (2020). DOI: [10.48550/ARXIV.2002.03010](https://doi.org/10.48550/ARXIV.2002.03010). URL: <https://arxiv.org/abs/2002.03010> (cit. on pp. 20, 26).
- [34] K. Abe et al. “Search for proton decay via  $pe^+\pi^0$  and  $p \rightarrow \mu^+\pi^0$  in 0.31 megaton  $\cdot$  years exposure of the Super-Kamiokande water Cherenkov detector”. In: *Phys. Rev. D* 95 (1 Jan. 2017), p. 012004. DOI: [10.1103/PhysRevD.95.012004](https://doi.org/10.1103/PhysRevD.95.012004). URL: <https://link.aps.org/doi/10.1103/PhysRevD.95.012004> (cit. on p. 21).
- [35] David R. Nygren. “Proposal to investigate the feasibility of a novel concept in particle detection”. In: (1974) (cit. on p. 21).
- [36] Carlo Rubbia. *The liquid-argon time projection chamber: a new concept for neutrino detectors*. Tech. rep. Geneva: CERN, 1977. URL: <https://cds.cern.ch/record/117852> (cit. on p. 21).
- [37] S. Kubota, A. Nakamoto, T. Takahashi, T. Hamada, E. Shibamura, M. Miyajima, K. Masuda, and T. Doke. “Recombination luminescence in liquid argon and in liquid xenon”. In: *Phys. Rev. B* 17 (6 Mar. 1978), pp. 2762–2765. DOI: [10.1103/PhysRevB.17.2762](https://doi.org/10.1103/PhysRevB.17.2762). URL: <https://link.aps.org/doi/10.1103/PhysRevB.17.2762> (cit. on pp. 23, 24, 100).
- [38] Ettore Segreto. “Properties of liquid argon scintillation light emission”. In: *Physical Review D* 103.4 (Feb. 2021). DOI: [10.1103/PhysRevD.103.043001](https://doi.org/10.1103/PhysRevD.103.043001). URL: <https://doi.org/10.1103/PhysRevD.103.043001> (cit. on p. 23).
- [39] Tadayoshi Doke, Kimiaki Masuda, and Eido Shibamura. “Estimation of absolute photon yields in liquid argon and xenon for relativistic (1 MeV) electrons”. In: *Nuclear Instruments and Methods in Physics Research Section A: Accelerators, Spectrometers, Detectors and Associated Equip-*

- ment 291.3 (1990), pp. 617–620. DOI: [https://doi.org/10.1016/0168-9002\(90\)90011-T](https://doi.org/10.1016/0168-9002(90)90011-T). URL: <https://www.sciencedirect.com/science/article/pii/016890029090011T> (cit. on p. 24).
- [40] T. Heindl, T. Dandl, M. Hofmann, R. Krücken, L. Oberauer, W. Potzel, J. Wieser, and A. Ulrich. “The scintillation of liquid argon”. In: *EPL (Europhysics Letters)* 91.6 (Sept. 2010), p. 62002. DOI: [10.1209/0295-5075/91/62002](https://doi.org/10.1209/0295-5075/91/62002). URL: <https://doi.org/10.1209%2F0295-5075%2F91%2F62002> (cit. on pp. 24, 25).
- [41] “Calculations of the Excimer State Energies of Xenon, as a Function of Nuclear Separation”. In: *J. Chem Physics* 52 (1970) (cit. on p. 24).
- [42] T. Doke. “FUNDAMENTAL PROPERTIES OF LIQUID ARGON, KRYPTON AND XENON AS RADIATION DETECTOR MEDIA”. In: *Experimental Techniques in High-Energy Nuclear and Particle Physics*, pp. 537–577. DOI: [10.1142/9789814355988\\_0010](https://doi.org/10.1142/9789814355988_0010). eprint: [https://www.worldscientific.com/doi/pdf/10.1142/9789814355988\\_0010](https://www.worldscientific.com/doi/pdf/10.1142/9789814355988_0010). URL: [https://www.worldscientific.com/doi/abs/10.1142/9789814355988\\_0010](https://www.worldscientific.com/doi/abs/10.1142/9789814355988_0010) (cit. on p. 24).
- [43] A.A. Machado, E. Segreto, D. Warner, A. Fauth, B. Gelli, R. Máximo, A. Pissolatti, L. Paulucci, and F. Marinho. “The X-ARAPUCA: an improvement of the ARAPUCA device”. In: *Journal of Instrumentation* 13.04 (Apr. 2018), pp. C04026–C04026. DOI: [10.1088/1748-0221/13/04/c04026](https://doi.org/10.1088/1748-0221/13/04/c04026). URL: <https://doi.org/10.1088%2F1748-0221%2F13%2F04%2Fc04026> (cit. on p. 27).
- [44] H. V. Souza. *ARAPUCA, light trapping device for the DUNE experiment*. 2021. DOI: [10.48550/ARXIV.2112.02967](https://arxiv.org/abs/2112.02967). URL: <https://arxiv.org/abs/2112.02967> (cit. on p. 30).
- [45] B. Abi et al. *The Single-Phase ProtoDUNE Technical Design Report*. 2017. DOI: [10.48550/ARXIV.1706.07081](https://arxiv.org/abs/1706.07081). URL: <https://arxiv.org/abs/1706.07081> (cit. on pp. 31, 49).
- [46] B. Abi et al. “First results on ProtoDUNE-SP liquid argon time projection chamber performance from a beam test at the CERN Neutrino Platform”. In: *Journal of Instrumentation* 15.12 (Dec. 2020), P12004–P12004. DOI: [10.1088/1748-0221/15/12/p12004](https://doi.org/10.1088/1748-0221/15/12/p12004). URL: <https://doi.org/10.1088%2F1748-0221%2F15%2F12%2Fp12004> (cit. on p. 34).



- [47] D. Whittington, S. Mufson, and B. Howard. “Scintillation light from cosmic-ray muons in liquid argon”. In: *Journal of Instrumentation* 11.05 (May 2016), P05016–P05016. DOI: [10.1088/1748-0221/11/05/p05016](https://doi.org/10.1088/1748-0221/11/05/p05016). URL: <https://doi.org/10.1088/1748-0221/11/05/p05016> (cit. on p. 35).
- [48] E. M. Conover. “Muon-induced backgrounds in the Double Chooz neutrino oscillation experiment”. In: (2014). URL: <http://pi.lib.uchicago.edu/1001/cat/bib/10168750> (cit. on p. 38).
- [49] R. Herbst, R. Claus, M. Freytag, G. Haller, M. Huffer, S. Maldonado, K. Nishimura, C. O’Grady, J. Panetta, A. Perazzo, B. Reese, L. Ruckman, J. G. Thayer, and M. Weaver. “Design of the SLAC RCE Platform: A general purpose ATCA based data acquisition system”. In: *2014 IEEE Nuclear Science Symposium and Medical Imaging Conference (NSS/MIC)*. 2014, pp. 1–4. DOI: [10.1109/NSSMIC.2014.7431254](https://doi.org/10.1109/NSSMIC.2014.7431254) (cit. on p. 39).
- [50] J. Anderson, K. Bauer, A. Borga, H. Boterenbrood, H. Chen, K. Chen, G. Drake, M. Dönszelmann, D. Francis, D. Guest, B. Gorini, M. Joos, F. Lanni, G. Lehmann Miotto, L. Levinson, J. Narevicius, W. Panduro Vazquez, A. Roich, S. Ryu, F. Schreuder, J. Schumacher, W. Vandelli, J. Vermeulen, D. Whiteson, W. Wu, and J. Zhang. “FELIX: a PCIe based high-throughput approach for interfacing front-end and trigger electronics in the ATLAS Upgrade framework”. In: *Journal of Instrumentation* 11.12 (Dec. 2016), pp. C12023–C12023. DOI: [10.1088/1748-0221/11/12/c12023](https://doi.org/10.1088/1748-0221/11/12/c12023). URL: <https://doi.org/10.1088/1748-0221/11/12/c12023> (cit. on p. 39).
- [51] E. Aprile et al. “The XENON1T dark matter experiment”. In: *The European Physical Journal C* 77.12 (Dec. 2017), p. 881. DOI: [10.1140/epjc/s10052-017-5326-3](https://doi.org/10.1140/epjc/s10052-017-5326-3). URL: <https://doi.org/10.1140/epjc/s10052-017-5326-3> (cit. on p. 40).
- [52] M. Auger, D. J. Auty, P. S. Barbeau, E. Beauchamp, V. Belov, C. Benitez-Medina, M. Breidenbach, T. Brunner, A. Burenkov, B. Cleveland, S. Cook, T. Daniels, M. Danilov, C. G. Davis, S. Delaquis, R. deVoe, A. Dobi, M. J. Dolinski, A. Dolgolenko, M. Dunford, W. Fairbank, J. Farine, W. Feldmeier, P. Fierlinger, D. Franco, G. Giroux, R. Gornea, K. Graham, G. Gratta, C. Hall, K. Hall, C. Hargrove, S. Herrin, M. Hughes, A. Johnson, T. N. Johnson, A. Karelin, L. J. Kaufman, A. Kuchenkov, K. S. Ku-

- mar, D. S. Leonard, F. Leonard, D. Mackay, R. MacLellan, M. Marino, B. Mong, M. Montero Díez, A. R. Müller, R. Neilson, R. Nelson, A. Odian, I. Ostrovskiy, K. O’Sullivan, C. Ouellet, A. Piepke, A. Pocar, C. Y. Prescott, K. Pushkin, P. C. Rowson, J. J. Russell, A. Sabourov, D. Sinclair, S. Slutsky, V. Stekhanov, T. Tolba, D. Tosi, K. Twelker, P. Vogel, J.-L. Vuilleumier, A. Waite, T. Walton, M. Weber, U. Wichoski, J. Wodin, J. D. Wright, L. Yang, Y.-R. Yen, and O. Ya. Zeldovich and. “Search for Neutrinoless Double-Beta Decay in  $^{136}\text{Xe}$ ”. In: *Physical Review Letters* 109.3 (July 2012). DOI: [10.1103/physrevlett.109.032505](https://doi.org/10.1103/physrevlett.109.032505). URL: <https://doi.org/10.1103/physrevlett.109.032505> (cit. on p. 40).
- [53] K. Abe, K. Hiraide, K. Ichimura, Y. Kishimoto, K. Kobayashi, M. Kobayashi, S. Moriyama, M. Nakahata, H. Ogawa, K. Sato, H. Sekiya, T. Suzuki, O. Takachio, A. Takeda, S. Tasaka, M. Yamashita, B.S. Yang, N.Y. Kim, Y.D. Kim, Y. Itow, K. Kanzawa, K. Masuda, K. Martens, Y. Suzuki, B. D. Xu, K. Miuchi, N. Oka, Y. Takeuchi, Y.H. Kim, K.B. Lee, M.K. Lee, Y. Fukuda, M. Miyasaka, K. Nishijima, K. Fushimi, G. Kanzaki, and S. Nakamura. “A measurement of the scintillation decay time constant of nuclear recoils in liquid xenon with the XMASS-I detector”. In: *Journal of Instrumentation* 13.12 (Dec. 2018), P12032–P12032. DOI: [10.1088/1748-0221/13/12/p12032](https://doi.org/10.1088/1748-0221/13/12/p12032). URL: <https://doi.org/10.1088/1748-0221/13/12/p12032> (cit. on p. 41).
- [54] D.L. Adams, M.C.Q. Bazetto, L. Bomben, S. Bordon, F. Boran, C. Brizzolari, G. Brunetti, C. Cattadori, F. Cavanna, G. De Souza, F. Dolek, Z. Djurcic, A. Falcone, N. Gallice, A. Himmel, U. Kose, E. Lutsenko, A.A. Machado, F. Pietropaolo, M. Prest, A. Rafique, B. Ramson, F. Resnati, P. Sala, E. Segreto, K. Spurgeon, H. Vieira de Souza, D. Totani, S. Tufanli, E. Vallazza, D. Warner, D. Whittington, R.J. Wilson, and A. Zani. “Doping liquid argon with xenon in ProtoDUNE Single-Phase”. In: () (cit. on pp. 41, 87).
- [55] R Acciarri, M Antonello, B Baibussinov, M Baldo-Ceolin, P Benetti, F Calaprice, E Calligarich, M Cambiaghi, N Canci, F Carbonara, F Cavanna, S Centro, A G Cocco, F Di Pompeo, G Fiorillo, C Galbiati, V Gallo, L Grandi, G Meng, I Modena, C Montanari, O Palamara, L Pandola, G B Pivano Mortari, F Pietropaolo, G L Raselli, M Roncadelli, M Rossella, C Rubbia, E Segreto, A M

- Szelc, S Ventura, and C Vignoli. “Effects of Nitrogen contamination in liquid Argon”. In: *Journal of Instrumentation* 5.06 (June 2010), P06003–P06003. DOI: 10.1088/1748-0221/5/06/p06003. URL: <https://doi.org/10.1088/1748-0221/5/06/p06003> (cit. on p. 41).
- [56] H. V. Souza. *ARAPUCA, light trapping device for the DUNE experiment*. 2021. DOI: 10.48550/ARXIV.2112.02967. URL: <https://arxiv.org/abs/2112.02967> (cit. on p. 48).
- [57] B. Howard, S. Mufson, D. Whittington, B. Adams, B. Baugh, J.R. Jordan, J. Karty, C.T. Macias, and A. Pla-Dalmau. “A Novel Use of Light Guides and Wavelength Shifting Plates for the Detection of Scintillation Photons in Large Liquid Argon Detectors”. In: *Nucl. Instrum. Meth.* 907 (2018), pp. 9–21. DOI: 10.1016/j.nima.2018.06.050. arXiv: 1710.11233 [physics.ins-det] (cit. on pp. 49, 82, 86).
- [58] Christopher Benson, Gabriel D. Orebi Gann, and Victor Gehman. “Measurements of the intrinsic quantum efficiency and absorption length of tetraphenyl butadiene thin films in the vacuum ultraviolet regime”. In: *The European Physical Journal C* 78.4 (Apr. 2018), p. 329. DOI: 10.1140/epjc/s10052-018-5807-z. URL: <https://doi.org/10.1140/epjc/s10052-018-5807-z> (cit. on pp. 50, 51, 57).
- [59] D. Totani, G. Canelo, F. Cavanna, C.O. Escobar, E. Kemp, F. Marinho, L. Paulucci, D.D. Phan, S. Mufson, C. Macias, and D. Warner. “A measurement of absolute efficiency of the ARAPUCA photon detector in liquid argon”. In: *Journal of Instrumentation* 15.06 (June 2020), T06003–T06003. DOI: 10.1088/1748-0221/15/06/t06003. URL: <https://doi.org/10.1088/1748-0221/15/06/t06003> (cit. on p. 57).
- [60] G Michna, S Gent, and A Propst. *CFD Analysis of Fluid, Heat, and Impurity Flows in DUNE FAR Detector to Address Additional Design Considerations*. Oct. 2017 (cit. on p. 61).
- [61] M. Babicz, S. Bordoni, A. Fava, U. Kose, M. Nessi, F. Pietropaolo, G.L. Raselli, F. Resnati, M. Rossella, P. Sala, F. Stocker, and A. Zani. “Light Propagation in Liquid Argon”. In: *JINST* 15 (Mar. 2020). 20 pages, 10 figures, P09009. 21 p. DOI: 10.1088/1748-0221/15/09/P09009. arXiv: 2002.09346. URL: <https://cds.cern.ch/record/2713386> (cit. on p. 82).

- [62] M. Babicz, S. Bordoni, T. Cervi, Z. Collins, A. Fava, U. Kose, M. Meli, A. Menegolli, M. Nessi, F. Pietropaolo, G.L. Raselli, F. Resnati, M. Rossella, P. Sala, and A. Zani. “Experimental study of the propagation of scintillation light in Liquid Argon”. In: *Nuclear Instruments and Methods in Physics Research Section A: Accelerators, Spectrometers, Detectors and Associated Equipment* 936 (2019). Frontier Detectors for Frontier Physics: 14th Pisa Meeting on Advanced Detectors, pp. 178–179. DOI: <https://doi.org/10.1016/j.nima.2018.10.082>. URL: <https://www.sciencedirect.com/science/article/pii/S0168900218313962> (cit. on p. 82).
- [63] G.M. Seidel, R.E. Lanou, and W. Yao. “Rayleigh scattering in rare-gas liquids”. In: *Nuclear Instruments and Methods in Physics Research Section A: Accelerators, Spectrometers, Detectors and Associated Equipment* 489.1 (2002), pp. 189–194. DOI: [https://doi.org/10.1016/S0168-9002\(02\)00890-2](https://doi.org/10.1016/S0168-9002(02)00890-2). URL: <https://www.sciencedirect.com/science/article/pii/S0168900202008902> (cit. on p. 82).
- [64] O. Schnepf and K. Dressler. “Absorption Spectra of Solid Xenon, Krypton, and Argon in the Vacuum Ultraviolet”. In: *The Journal of Chemical Physics* 33.1 (1960), pp. 49–55. DOI: [10.1063/1.1731133](https://doi.org/10.1063/1.1731133). eprint: <https://doi.org/10.1063/1.1731133>. URL: <https://doi.org/10.1063/1.1731133> (cit. on p. 95).
- [65] A Higuera, Y. Jwa, and G. Karagiorgi. *Proton Decay  $p \rightarrow \pi^0 K^+$* . 2019 (cit. on pp. 104, 106).
- [66] Costas Andreopoulos, Christopher Barry, Steve Dytman, Hugh Gallagher, Tomasz Golan, Robert Hatcher, Gabriel Perdue, and Julia Yarba. *The GENIE Neutrino Monte Carlo Generator: Physics and User Manual*. 2015. DOI: [10.48550/ARXIV.1510.05494](https://arxiv.org/abs/1510.05494). URL: <https://arxiv.org/abs/1510.05494> (cit. on p. 105).
- [67] MicroBooNE Collaboration et al. *The Pandora multi-algorithm approach to automated pattern recognition of cosmic-ray muon and neutrino events in the MicroBooNE detector*. 2017. DOI: [10.48550/ARXIV.1708.03135](https://arxiv.org/abs/1708.03135). URL: <https://arxiv.org/abs/1708.03135> (cit. on p. 106).

## Vita

Author's Name: Kyle Spurgeon

Place of Birth: Kansas City, Kansas, USA

Date of Birth: December, 24 1993

Degrees Awarded:

Bachelor of Science, University of Northern Iowa, 2016

Professional Experience:

Research Assistant, Syracuse University Department of Physics, 2018-2022